UNIVERSITÀ
DEGLI STUDI
DI PADOVA


Università degli Studi di Padova

Dipartimento di Fisica e Astronomia "Galileo Galilei"

Corso di Laurea Magistrale in Astronomia


TESI DI LAUREA MAGISTRALE IN ASTRONOMIA

# SAMPLE SELECTION OF TYPE-II AGNs IN THE SOUTHERN SKY


Relatore
Prof. Stefano Ciroi

Laureando
Mattia Gioele Prendin
Matricola n°
1147582


ANNO ACCADEMICO 2018-2019

Universitá degli Studi di Padova

Tesi di laurea Magistrale

in Astronomia

# Sample selection of type-II AGNs in the southern sky


Student:

**Mattia Gioele Prendin**

Supervisor: **S. Ciroi**

26 September 2019

# Abstract

According to the Unified Model of Active Galactic Nuclei (AGNs), the Extended Narrow line Region (ENLR) also called "ionization cones", is expected to be diffusely present. On the contrary, only a few tens of AGNs are known to show this structure of ionized gas. The small number of observed ionization cones may be related to the difficulty of finding them. Indeed their discovery is quite often a result of serendipitous detections. In the past, some authors attemped to image nearby Seyfert galaxies through interferential filters and their researches had success but they were limited to small samples of AGNs. Nowadays, huge spectroscopic archives of galaxies are available and this offers the unique opportunity to identify hundreds of new AGNs potentially hosting ionization cones. The aim of this work is the selection of a new sample of type-II AGNs visible at southern latitudes to obtain a catalogue of targets for an already planned observational campaign with [O III] filters at Las Campanas Observatory (Chile). The AGNs were selected from the 6dFGS and partly from the SDSS spectroscopic surveys starting from 12737 and 36315 emission line galaxies, respectively. After having found a way to calibrate 6dFGS in flux, the underlying stellar component was subtracted from all the data, and the main emission lines were fitted with a multi-Gaussian approach. Then, through diagnostic diagrams as [O III] $\lambda$5007/H$\beta$ vs [N II] $\lambda$6584/H$\alpha$ and [O I] $\lambda$6300/[O III] $\lambda$5007 vs [O II] $\lambda$3727/[O III] $\lambda$5007, a sample of 761 sources was obtained.

The characterization of the AGN types was carried out by means of the comparison of the FWHMs of H$\alpha$ and H$\beta$. A sub-sample of 80 possible type-1.9 Seyfert was detected.

Finally, the size-luminosity relation for the ENLR was applied and the plot was used to select 200 candidates showing [O III] luminosity $L_{[O\,III]} \geq 10^{42}\,erg\,s^{-1}$. The main idea behind this limit is the following: since the [O III] luminosity is proportional to the power of the AGN, the highest values of $L_{[O\,III]}$ could indicate an AGN potentially able to ionize gas up to several kpc from the nucleus.

# Abstract

Secondo il modello unificato dei Nuclei Galattici Attivi (AGNs), si ritiene che la Extended Narrow line Region (ENLR) anche nota come "coni di ionizzazione", sia largamente diffusa in questi oggetti. In realtà, ad oggi sono conosciute solo una decina di AGNs che presentano questa struttura di gas ionizzato. Il numero esiguo di coni di ionizzazione osservati potrebbe essere legato alla difficoltà di individuarli, infatti la loro scoperta è spesso inaspettata.

In passato, alcuni autori hanno tentato di osservare le galassie di Seyfert più vicine attraverso l'utilizzo di filtri interferenziali per individuare queste strutture. Le loro ricerche hanno avuto successo, ma il numero esiguo di sorgenti non ha permesso di individuarne molte. Negli ultimi anni, la quantità di dati spettroscopici disponibili è enorme e questo permette l'opportunità unica di identificare centinaia di nuovi AGNs che potenzialmente possono ospitare coni di ionizzazione. Lo scopo di questo lavoro è la selezione di un nuovo campione di AGNs type-II visibile a latitudini australi per ottenere un catalogo di oggetti per una campagna osservativa già pianificata utilizzando filtri [O III] all'Osservatorio Las Campanas (Cile).

Gli AGNs sono stati selezionati dalle survey spettroscopiche 6dFGS e parte della SDSS partendo rispettivamente da un campione iniziale di galassie caratterizzate da righe di emissione di 12737 e 36315 oggetti. Dopo aver trovato un metodo per calibrare in flusso gli spettri della 6dFGS, la componente stellare è stata sottratta da tutti i dati e le principali righe di emissione sono state fittate con un approccio multi-Gaussiano. Successivamente, per mezzo dei diagrammi diagnostici come [O III] $\lambda$5007/H$\beta$ vs [N II] $\lambda$6584/H$\alpha$

and [O I] $\lambda$6300/[O III] $\lambda$5007 vs [O II] $\lambda$3727/[O III] $\lambda$5007, si è ottenuto un campione di 761 galassie. La caratterizzazione dei tipi di AGNs è stata eseguita confrontando le FWHMs di H$\alpha$ e H$\beta$. In questo modo è stato selezionato un sottocampione di 80 possibili AGNs tipo-1.9. Infine è stata applicata la relazione dimensione-luminosità per le ENLRs e dal grafico si è ottenuto un campione di 200 candidati caratterizzati dalla luminosità di [O III] $L_{[O\,III]} \geq 10^{42}\,erg\,s^{-1}$. La principale idea alla base della scelta di questo limite è la seguente: poichè la luminosità di [O III] è proporzionale alla potenza dell'AGNs, i valori più alti di $L_{[O\,III]}$ potrebbero indicare un AGN che potenzialmente può ionizzare il gas a vari kpc dal nucleo.

# Acknowledgment

This thesis is based on of the NASA/IPAC Extragalactic Database (NED) provided by the Jet Propulsion Laboratory, California Institute of Technology, under contract with the National Aeronautics and Space Administration. Funding for the Sloan Digital Sky Survey IV has been provided by the Alfred P. Sloan Foundation, the U.S. Department of Energy Office of Science, and the Participating Institutions. SDSS acknowledges support and resources from the Center for High-Performance Computing at the University of Utah. The SDSS web site is www.sdss.org. We acknowledge the efforts of the staff of the Australian Astronomical Observatory (AAO), who have undertaken the survey observations and developed the 6dF instrument. The STARLIGHT project is supported by the Brazilian agencies CNPq, CAPES and FAPESP and by the France-Brazil CAPES/Cofecub program.

"The Universe is full of magical things patiently

waiting for our wits to grow sharper"

Eden Philpotts

# Contents

# Introduction

Active Galactic Nuclei (AGN) are very powerful sources of radiation that extends from radio wavelengths to gamma rays through different energy processes. Decades of observations of the AGN family led to the identification and definition of distinct groups: Seyfert galaxies, quasars, radio galaxies, blazars, etc. All of them are believed to be the result of the accretion of matter onto a supermassive black hole surrounded by highly ionized gaseous region, the Broad Line Region (BLR), an obscuring torus of dust and gas, and a less ionized gaseous region, the Narrow Line Region (NLR). One of the most used methods to identify an AGN is based on the analysis of the optical lines (Padovani et al. 2017).

The measure of the Full Width at Half Maximum (FWHM) of the Balmer lines is an indicator of the orientation of the source and permits to divide the AGNs in two main classes, type-I and type-II. The latter group is sometimes characterized by extended narrow line regions (ENLR) with a size from few up to $15 - 20\,\mathrm{kpc}$ supposed to be produced by the anysotropic radiation coming from the center of the AGN. These structures are present in both AGN classes, but the orientation of the dusty torus of the type-II sources allows a better observation of them. According to the Unified Model (Antonucci 1993), that explains most of the observed properties of AGNs as an inclination of our line of sight with respect to the torus axis, the detection of the ENLR should be very frequent. In fact, until now, only a few tens of them are known ($\approx$ 50 at $z < 0.05$, Netzer 2015). The aim of this thesis is the preparation of a well selected sample of type-II AGNs using the largest spectroscopic database of the

southern hemisphere, the 6dFGS and part of the SDSS spectroscopic survey in order to carry out new observations and hopefully discover new ENLRs by means of the instrumentation available in the southern observatories. This thesis is organized in four chapters: the first is an overview on the AGN's characteristic features through the whole electromagnetic spectrum and the description of the unification model. The second chapter describes the properties of the NLR and the importance of the analysis of this region. The third chapter is dedicated to the methods used to select the sample and the description of the surveys used in this work. The last chapter show the result obtained and the comparison with others works.

# Chapter 1

# Active Galactic Nuclei

Active Galactic Nuclei (AGNs) are stronger emitters compared to the nuclei of "normal" galaxies. These sources are characterized by the presence of a super massive accreting black hole (SMBH) with Eddington ratio[1] exceeding the limit of $L_{AGN}/L_{Edd} = 10^{-5}$ where $L_{AGN}$ is the bolometric luminosity and $L_{Edd} = 1.5 \times 10^{38}\, M_{BH}/M_{\odot}\, \mathrm{erg\,s^{-1}}$ is the Eddington luminosity for a compact object with the same composition of the Sun. Moreover AGNs show observational signatures that cover the full electromagnetic spectrum. The amount of energy is produced by gas falling onto the SMBH. To explain the observed spectral properties of AGNs the presence of several elements has been supposed:

- a rotational dominated accretion flow that refers to the accretion disk of the SMBH
- a broad line region (BLR), characterized by high density and dust-free gas clouds moving rapidly at a luminosity dependent distance of $0.01 - 1\,\mathrm{pc}$ from the SMBH
- a dusty axisymmetric structure, the torus, with a luminosity dependent dimension of $1 - 10\,\mathrm{pc}$

[1]The Eddington luminosity is the maximum luminosity a body can achieve in hydrostatic equilibrium, when there is balance between the force of radiation acting outward and the gravitational force acting inward. The Eddington limit is used to explain the observed luminosity of accreting black holes such as quasars.

- a narrow line region (NLR) extending from just outside the torus to hundreds or thousands of parsecs along the direction perpendicular to the torus plane. This region is characterized by lower density and lower velocity ionized gas

- a radio jet oriented in perpendicular direction with respect to the accretion disk

These different elements contribute to different energy range and, thanks to that, the emission cover the whole electromagnetic spectrum in (fig. 1.1).

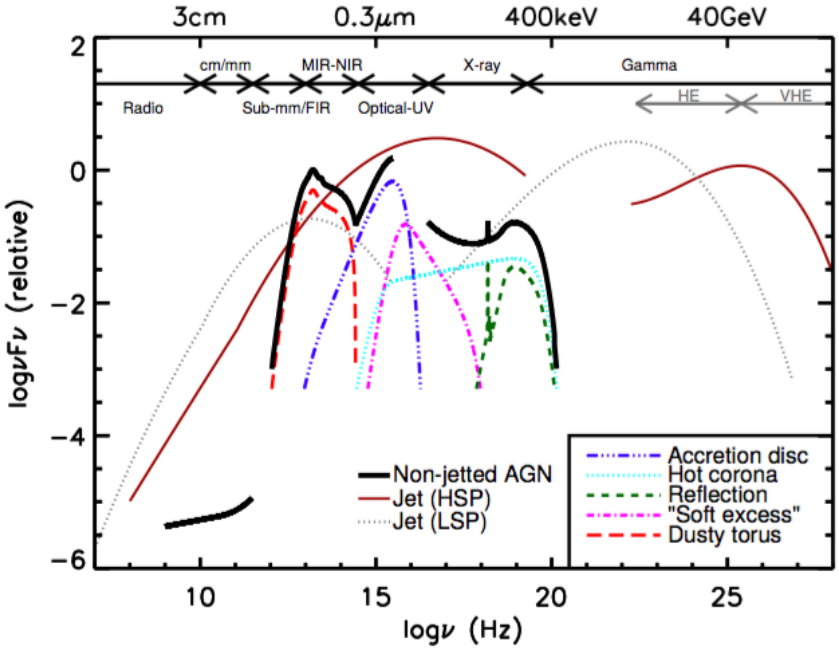


**Figure 1.1:** Schematic representation of an AGN spectral energy distribution (Padovani et al. 2017). The black solid line represents the total emission and the various colored curves represent the individual ones.

The various wavelength ranges provide different windows on AGN physics. The obscuring material and dust that compose the torus emit mainly in the infrared band, the ultraviolet/optical bands are characterized by emissions from BLR, NLR and from the accretion disk. The emission from $\gamma$-ray, X-ray and radio bands are product by non-thermal processes while the lower energetic X-ray emission can also be produced by the hotter part of the accretion disk (Padovani et al. 2017). Detailed studies of large samples of AGNs and the understanding of their connection with inactive galaxies

started in the late 1970s, long after the discovery of the first quasar in the early 1960s and the first observation of this kind of galaxies made by Seyfert in the late of 1940s. The AGNs classification is based on high-quality observations of a huge number of objects and the main subgroups are:

- type-I radio quiet (type-I Seyfert and radio quiet quasar)
- type-I radio loud (BLRGs and radio loud quasar)
- type-II radio quiet (type-II Seyfert)
- type-II radio loud (NLRGs)
- LINERs
- Blazar

## 1.1 Seyfert galaxies

In the local universe, the Seyfert galaxies are the most common class of AGNs that can be observed. The images of them typically show a bright central point-like core and their spectra show highly ionized emission lines, indeed the identification of these objects is based on their spectral features. In the early of 1970s, analyzing the spectra of Seyfert galaxies it was found two distinct types of optical spectra, indeed all the spectra showed narrow emission lines but only some of them showed broad emission lines, therefore they were separated into classes according to their relative widths of the forbidden and Balmer lines (Khachikian and Weedman 1974). The strongest lines that characterize the spectra of these galaxies are [O III] $\lambda\lambda$4959,5007, [N II] $\lambda\lambda$6548,6584, [O II] $\lambda$3727 and the hydrogen and helium lines (Netzer 2015). In the spectra of type-I Seyfert the permitted lines and some of the semi-forbidden lines appear broader with respect to the forbidden lines while the spectra of type-II Seyfert show permitted and forbidden lines with the same narrow width. The narrow emission lines show a typical

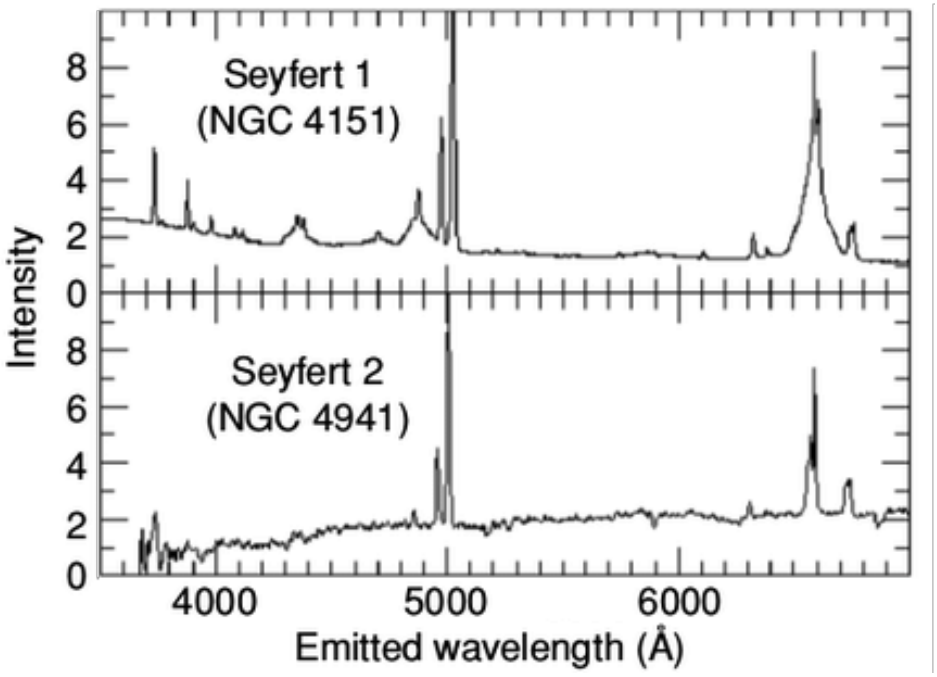


**Figure 1.2:** Comparison between the optical spectrum of the type-I Seyfert NGC 4151 and the type-II Seyfert NGC 4941. The intensity unit is $10^{-14}\,\mathrm{erg\,cm^{-2}\,s^{-1}}$ (Netzer 2013).

full with at half maximum (FWHM) of 300-1000 $\mathrm{km\,s^{-1}}$ and they are supposed to be emitted by low-density gas characterized by an electron density $n_e \approx 10^3 - 10^6\,\mathrm{cm^{-3}}$. The broad emission lines show a larger FWHM up to 20000 $\mathrm{km\,s^{-1}}$ indicating a higher velocity of the gas. This emission is supposed to come from a region close to the accretion disk and called broad line region (BLR) characterized by $n_e \geq 10^9\,\mathrm{cm^{-3}}$ (Beckmann 2012).

In fig. 1.2 it is possible to compare the spectra of the two types of sources. The continuum shows a superposition of the emission from the host galaxy and the AGN core. In the type-I Seyfert the AGN core appears more luminous with respect to the emission of the surrounding galaxy, while the type-II Seyfert shows a stronger host galaxy emission characterized by the presence of stellar absorption lines.
The continuum of type-I Seyfert appears featureless and often exhibits a non-thermal emission well different from the stellar one. It is supposed that the continuum emission of the AGNs core is a signature of the presence of an accretion disk around the SMBH

and it can be described as a superposition of many black-body spectra of a continuous range of temperature. According to the Balmer lines characteristic the Seyfert galaxies are divided in several sub-groups like type 1.2, 1.5, 1.8 and 1.9. The Seyfert 1.2 show the typical broad Balmer line of the type-I but H$\beta$ is slightly less broad with respect to the others. The Seyfert 1.5 are characterized by an H$\beta$ line in which the broad component is strong as the narrow one and in the Seyfert 1.8 and 1.9 the Balmer lines appear with weaker broad component, moreover the Seyfert 1.9 present a broad component only in the H$\alpha$ emission line (D. E. Osterbrock 1977).

## 1.2 LINERs

The low-ionization nuclear emission-line regions (LINERs) are AGNs characterize by faint core luminosity. The typical strong emission lines that characterize this group of sources are [O II] $\lambda$3727, [O I] $\lambda$6300, [N II] $\lambda\lambda$6548, 6584, [S, II] $\lambda\lambda$6717, 6731 and the Balmer lines. It is supposed that LINERs may be AGNs accreting at lower radiative efficiency or at lower rate with respect to Seyfert galaxies and therefore are considerate low-luminosity AGNs. Indeed a recent study suggested that AGNs could be divided in two different groups, the radiative-mode and the jet-mode (Heckman and Best 2014). The first group is refereed to the Seyfert galaxies and to the quasar in which most of their energy output is in the form of thermal radiation as result of the emitted photons from accretion disk. These objects are the most luminous with $L_{AGN}/L_{Edd} > 0.01$. They are defined as high ionization AGNs due to the level of ionization of the ions present in the NLR. The latter group is composed by the low luminosity radio galaxies and by LINERs in which the prime energy output of these objects is supposed to be the bulk of kinetic energy transported by the two-side jets and others non-thermal processes.

## 1.3 Diagnostic diagrams

The mainly used method to distinguish the different emission line galaxies is based on the diagnostic diagrams (fig. 1.3). Characteristic emission lines can be produced by different sources of ionizing photons: some galaxies show the presence of AGN core, others appear excited by star-forming regions and others show a combination of both. The diagnostic diagrams were introduced by Baldwin, Phillips, and Terlevich 1981 and successively revised by Veilleux and Donald E. Osterbrock 1987, they are based on the comparison of various emission-line intensity ratios. The observed emission lines contain a lot of information about the gas condition as the ionization level, temperature, density and composition and the analysis of their ratios, permit to discern the different type of photoionization source. The [O III] $\lambda$5007/H$\beta$ line ratio give a lot of information about the ionization level of the gas. A strong [O III] line indicates a high level of ionization, and large amount of energy from the source while the flux of H$\beta$ is proportional to the recombination of the Hydrogen ions so it gives a measure of the number of the photons absorbed by the gas. Galaxies dominated by AGNs core are characterized by a high [O III] $\lambda$5007/H$\beta$ ratio, while lower values indicate the presence of different photoionization source as early-type stars as in the star-forming galaxies. The intensity lines ratio [O I] $\lambda$6300/H$\alpha$ permit to analyze the properties of low ionized sources. In particular [O I] is a strong line in partly ionized gas in case of ionization from AGN core, indeed only the X-ray photons emitted by the AGNs can ionized the gas beyond the $H^+$ ionization front and penetrate into the regions where the oxygen is neutral. In the case of photoionization from star-forming regions, the photons emitted by massive early-type stars cannot penetrate the ionization front thus the [O I] emission line is weak (Netzer 2013). Often the [O I] is too weak to be measured so it is used the line ratio [N II] $\lambda$6584/H$\alpha$ that provides similar information.

In fig. 1.3 are plotted the various diagnostic diagrams that are used to classify the emission line galaxies. In order to separate the different sources it was developed a

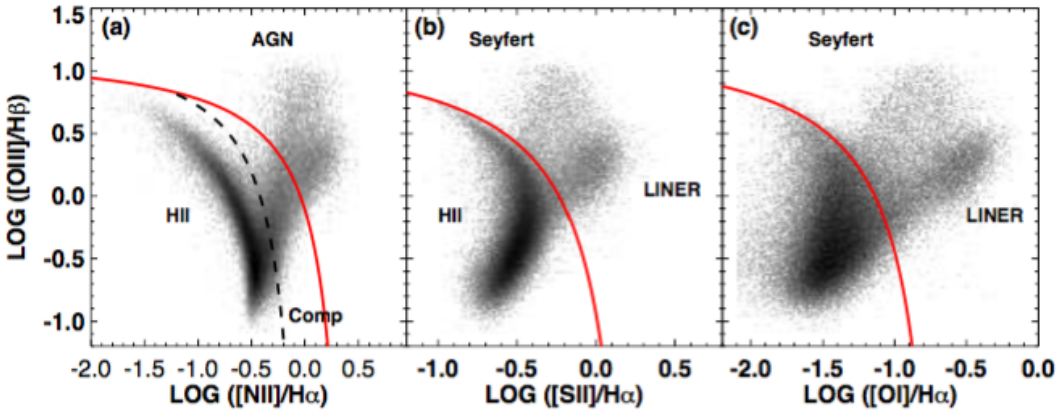


**Figure 1.3:** a) The [N II]/H$\alpha$ vs [O III]/H$\beta$ diagnostic diagram for SDSS galaxies with $S/N > 3$ b) The [SII]/H$\alpha$ vs [O III]/H$\beta$ diagnostic diagram, c) The [O I]/H$\alpha$ vs [O III]/H$\beta$ diagnostic diagram. The solid line represents the extreme star-forming line (Kewley et al. 2001) and the dashed line the classification proposed by Kauffmann et al. 2003.

"maximum starburst line" (Ke01, the red line in the plots) that represents the theoretical limit for a pure stellar photoionization model, sources lying above this line are dominated by AGN (Kewley et al. 2001). In order to obtain this limit a combination of stellar population synthesis and photoionization models were used. The second line plotted (Ka03, the black dashed line in the plot) on the diagnostic diagrams was modeled by Kauffmann et al. 2003, it represents the empirical division between star-forming and the composite galaxies that show photoionization from both star forming regions and AGN. Following the diagnostic diagram of [O III]/H$\beta$ vs [N II]/H$\alpha$, the star-forming galaxies occupy the region below the Ka03 line, while the composite galaxies lying between the two separation lines and the pure-AGN sources lie above the Ke01 line (L. J. Kewley et al. 2006).

## 1.4 Radio galaxies

On the basis of their radio emission, AGNs are divided in to Radio Quiet (RQ) and Radio Loud (RL). This division is based on the *radio loud-ness* parameter $R$ that is a

measure of the ratio between radio and optical B-band luminosity.

$$R = \frac{L_\nu(5\,\mathrm{GHz})}{L_\nu(4400\mathrm{A})} \tag{1.1}$$

Usually it is chosen R = 10 as value limit between RQ and RL. Moreover, local universe observations show that most of the radio emitters are RQ while only 10% of the galaxies shows RL proprieties. The dominant emission process is the synchrotron radiation and the radio spectrum is represented by a single power law $F_\nu \propto \nu^{-\alpha_r}$. The AGNs showing $\alpha_r < 0.5$ are named *flat-spectrum radio sources*, while those with $\alpha_r > 0.5$ are refereed to *steep-spectrum radio sources*. The first ones have higher luminous cores and weak or undetectable lobes and following the classification proposed by Fanaroff and Riley 1974 are low-luminosity Fanaroff-Riley class-I galaxies (FR-I) while the other ones that show a lobe-dominated radio morphology are classified also as high-luminosity Fanaroff-Riley class-II galaxies (FR-II). This dichotomy is interpreted as the result of our viewing angle with respect to the radio emission. In particular, in flat-spectrum sources the line of sight (LoS) is oriented at a small angle with respect to the direction of the jet, while in steep-spectrum sources the LoS is far from the direction of the jet (Netzer 2013). In fig. 1.4 are plotted some examples of the two different objects.

In the last years it was introduced the FR-0 class by Baldi, Capetti, and Giovannini 2015, it corresponds to radio galaxies that appears as FR-I but showing a more concentrated emission, they are $\approx 30$ times more core-dominated. In order to explain that two different scenarios were supposed. The first proposed that the FR-0 sources correspond to young intermittent radio sources that can evolve into extended radio galaxies, but it is in contrast with the low-luminosity radio galaxies model that supposed a continuous accretion of hot gas from the corona. The second scenario suggests that FR-0 are characterized by a lower Lorentz factors $\Gamma$[2], so their jets are less stable

[2]It is refereed to the emitted matter and it is defined as $\Gamma = \frac{1}{\sqrt{1-\frac{v^2}{c^2}}}$

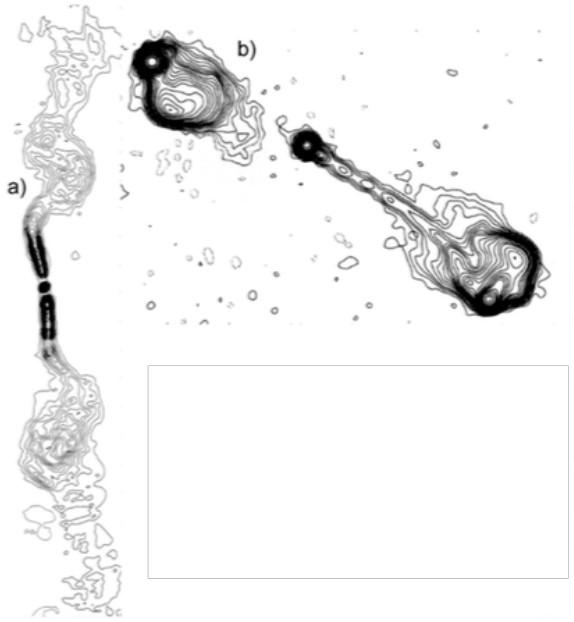


**Figure 1.4:** Example of Fanaroff-Riley sources: a) 3C 499 classified as FR-I, b) 3C 175 classified as FR-II. The concentration of the black solid line correspond to the amount of emission (Padovani et al. 2017).

against the passage through the interstellar material of the circumnuclear region of the host galaxies and it can cause their destruction. Another way to classifie the AGNs in radio band is through their optical spectrum (Hine and Longair 1979). Objects that show high ionization level emissions lines as Seyfert galaxies and quasars are classified as High Emission Galaxies (HEG) while sources that show low ionization level lines as LINERs correspond to Low Emission Galaxies (LEG) (Padovani et al. 2017).

## 1.5 Quasar

Quasar is the acronym of *quasi-stellar radio sources*, these objects correspond to the optical counterpart of some radio sources discovered between the late of 1950s and early 1960s using radio telescopes. They appeared in optical images as blues stars, and their spectra showed various strong emission lines. Observing the optical spectra of 3C 273, Maarten Schmidt in 1963 realized that the lines corresponded to Balmer lines redshifted by 16% (Beckmann 2012). It was necessary other twenty years and the

advent of the space telescopes to confirm that quasars underline the same phenomenon of Seyfert galaxies but at higher distance. In optical and UV observations these sources appear bluer with respect to other galaxies. This feature permits their identification and it is known as the *big blue bump*. It is supposed that the bump is due to the presence of the accretion disk. Moreover in 2011, thanks to infrared observations that permit the identification of the earliest quasar showing the Ly$\alpha$ emission line in this band due to the high redshift of the source, a quasar with $z = 7.1$ was observed and this corresponds to 0.77 billion years after the Big Bang (Mortlock 2011).

## 1.6 Blazar

It is supposed that Blazars are sources in which the relativistic jet is pointing toward the observer. Their energy output is dominated by non-thermal radiation that arises in a relativistic jet and the spectral energy distribution (SED), covering the whole electromagnetic spectrum, shows a typical "double humped" shape (fig. 1.5). The component at lower energy peaks between IR and X-ray band and is produced by relativistic electrons moving in a magnetic field. The nature of the higher energy component has two different plausible interpretations. In the first, described by the leptonic models (Maraschi, Ghisellini, and Celotti 1992), the emission it is supposed to be produced by inverse Compton scattering between the electrons in the jet and their own synchrotron emission, this process is known as synchrotron self-Compton. In the latter, described by the hadronic scenario (Böttcher et al. 2013), it is supposed that the $\gamma$-ray emission originate from photons loosing energy either through synchrotron emission or through photo-meson interactions.

The Blazars can be divided in two classes as showed in fig. 1.6, the BL Lacertae (BL-Lac) and the flat spectrum radio quasar (FSRQ). The two sources differ in the emission from the optical to soft X-ray bands, the first does not present any particular feature because the non-thermal emission is dominant in the whole spectrum while

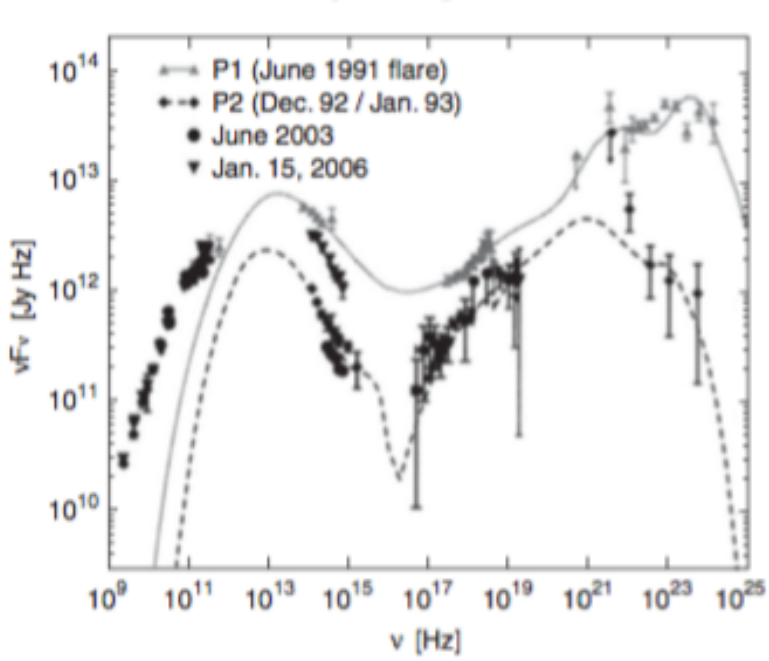


**Figure 1.5:** The multiepoch, multiwavelength spectrum of the blazar 3C 279. It shows the characteristic two peaks at low and high energies and the long-term variation of the source (Beckmann 2012).

the latter shows optical and UV emission lines from the BLR overlapping the thermal continuum from the accretion disk. In order to classify it is used the equivalent width (EW) of the emission lines, sources that show EW $>$ 5 Å are classified as FSRQ. Another property that shows these objects is the variability of the emissions in the whole electromagnetic spectrum, the variations can have time scale from years to some days (Beckmann 2012).

## 1.7 AGNs Unification Scheme

The unification scheme tried to give a unique theoretical model of the AGNs to explain the observation in different wavelengths bands. Fig. 1.7 shows the elements that are supposed to be present in AGNs and the classification.

The old unification scheme (Antonucci 1993) was developed to combine the huge number of different class of AGNs into a pictures based on two parameters: the torus

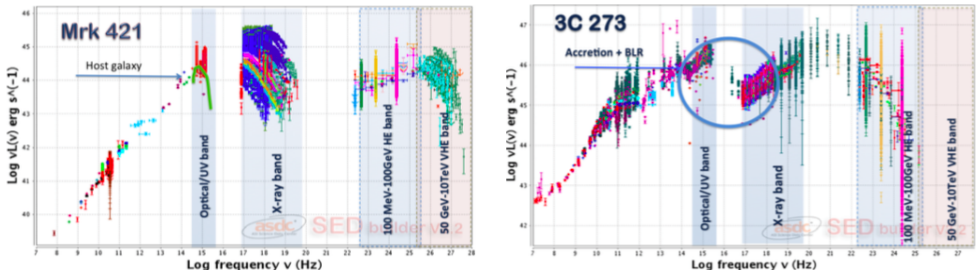


**Figure 1.6:** On the left the SED of the BL Lac Mrk 421, the green line represents the typical spectrum of a blazar host galaxy, it is also possible to see the variability of the source that dominates in the X-ray and $\gamma$-ray where it is present the peak of the emission. On the right, the SED of the FSRQ 3C 273 that shows the strong non-thermal emission coming from the jet in the entire spectrum, but from optical to soft x-ray the spectrum is dominated by emissions from the accretion disk and the BLR (Padovani et al. 2017).

inclination with respect to the line of sight (LoS) and the luminosity of the central source. The original idea of torus was a central axisymmetric dusty structure placed around the accretion disk of the central SMBH characterized by a column density[3] large enough to obscure the central source in some directions. Following studies proposed a more complex structure characterized by dense clouds of dust immersed in diffuse atomic and ionized gas (Netzer 2015). The first observation of the thermal emission from the torus of Cygnus A appeared to be consistent with the multi-phase torus model (Carilli et al. 2019). The observational consequence of the presence of the torus, is the inclination dependence of the obscuring column and the polarization of the radiation reflected from dust and free electrons. In type-I AGNs our LoS has small inclination with respect to the direction of the torus axis providing an un-obscured view of the accretion disk and BLR. On the contrary type-II AGNs are characterized by higher inclinations of the LoS and the regions cited above are obscured in the UV and soft X-rays bands by the dusty torus. If the anisotropy of the AGN population would be caused by the different amount of absorption, the intrinsic properties of the AGNs would be expected to be similar for all these sources. In order to test this idea, polarized light observations were employed, that permitted to analyze the photons coming from the inner part of

[3]Column density is a measure of the amount of matter between an observer and the observed object

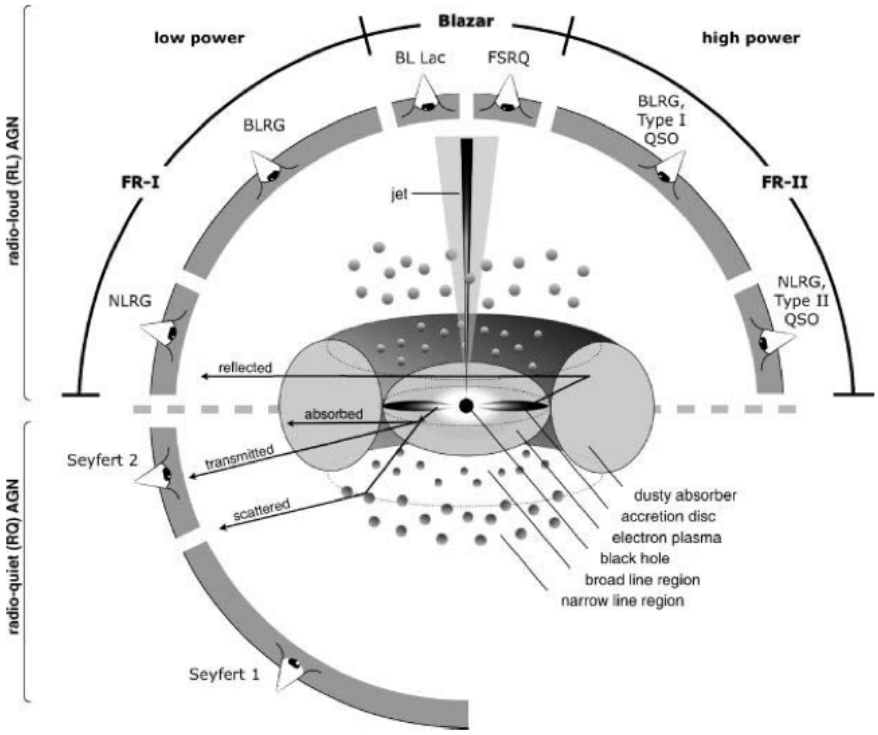


**Figure 1.7:** Unification scheme for AGNs. On the top of the image the radio-loud class, on the bottom the radio quiet (Beckmann 2012).

the active nucleus that are not absorbed by the dust. These photons are scattered by the free electrons present in the inter-clumpy medium. The scattering material acts like a mirror which permits to look behind the absorbing matter (Beckmann 2012). Observations of type-II Seyfert galaxies confirmed the hypothesis, broad Balmer lines photons and the continuum coming from the accretion disk, presented the same polarization. From the other side the narrow forbidden lines from the narrow line region do not show any polarization degree confirming its direct observations. (Tran, Miller, and Kay 1992). Following observations showed that only 40% of the type-II Seyfert seem to harbor a hidden broad line region (HBLR) (Wu et al. 2011). It was observed that only the more luminous AGNs with $L_{AGN}/L_{Edd} > 0.01$ showed the presence of the BLR. Sources characterized by $L_{AGN}/L_{Edd} < 0.01$ do not show strong absorption and neither in normal nor in polarized light one showed the presence of a broad line region (Trump et al. 2011). The type-II AGNs class was divided in further two sub-class the

"hidden" type-II and the "real" type-II. The first presents a HBLR while the latter do not show it in spectropolarimetric observations. These observations permitted to add a new parameter to the unification scheme and underlines on one side the difficulty to create a unique model to explain all the observed features of these objects, but from the other side the strength of this approach.

# Chapter 2

# Extended Narrow Line Region

The Unified Model postulates the presence of an anisotropic photoionization field confined by the torus. The extended narrow-line region (ENLR), that it is observable in some AGNs, is one evidence of it. This region is composed by highly ionized gas and the spectrum is similar to the one emitted from the narrow-line region, characterized by strong optical emission lines. The properties of forbidden and semi-forbidden lines suggest that NLR is characterized by high density clouds ($n_H \approx 10^2 - 10^6\,\mathrm{cm}^{-3}$), electronic temperature ($T_e \approx 10^4\,K$) and FWHM of the emission lines within the range $300 - 1000\,\mathrm{km\,s}^{-1}$ (Beckmann 2012) surrounded by low-density but high ionized gas. The central source provides the ionization field composed by a non-thermal power law spectrum plus possible others contributions from shocks or photoionization by circumnuclear star-forming regions. Moreover, in some clouds the column density is small enough to permit the presence of dust in the environment and this can influence the spectrum. Compared to the NLR which is traced up to few kiloparsec from the nucleus, strongest emission lines were observed up to $\approx 20\,\mathrm{kpc}$ from it. The shape of ENLRs is often conical or bi-conical with the two apexes pointing towards the active nucleus, and in these cases it is called *ionization cones*. In fig. 2.1 it is possible to see the shape of the ENLR of the galaxy Mrk 573.

According to the unification model, these structures should be observed in both

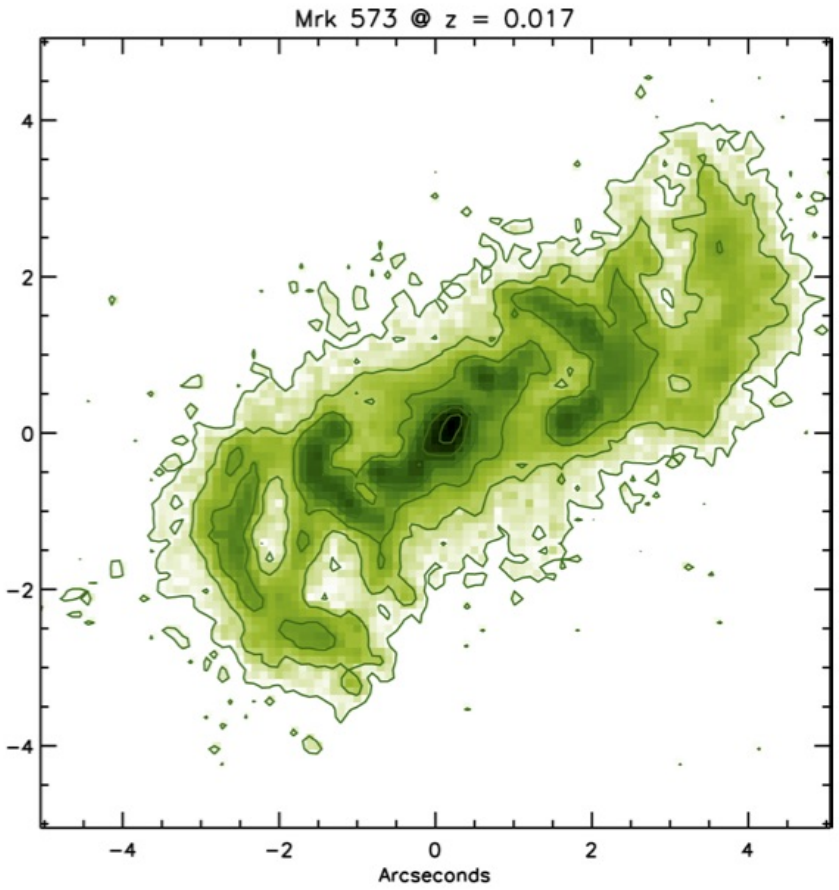


**Figure 2.1:** Image of the [O III] emission of Mrk 573 from the Archival HST/WFPC2.

type-II and type-I AGNs but the characteristics of the ENLRs in the latter class are supposed to be partially different. Due to the different inclination of the structures with respect to the LoS, a smaller and halo-like ENLR is expected in type-I AGNs. Observations partially confirmed the hypothesis but some exceptions of conical ENLR observed in type-I sources are present (Schmitt et al. 2003).

Another example is two objects observed with HST, they show a halo-like E-NLRs and for one of them it was confirmed the presence of a broad H$\alpha$ component from its spectrum confirming the observation of a type-I Seyfert nucleus. In this case the shape of the ENLR was consistent with a more inclined visualization of the AGN (Storchi-Bergmann et al. 2018). The small number of ionization cones observed until now (around 50), and their particular shape detected in some AGNs could be related to

the origin of the ionized gas present in these structures. Indeed, it could be part of the interstellar medium of the host galaxy, or material ejected by the nucleus in strong interaction with the radio-jet. Moreover, considering a dense environment, the gas could be acquired from the intergalactic medium or provided by gravitational interaction as in case of minor merging events (Cracco et al. 2011).

## 2.1 Physical description

The ionization parameter $U$ (eqn. 2.1) is an important parameter to understand the physics of the ENLRs

$$U = \frac{\Phi}{4\pi r^2 n_H c} \tag{2.1}$$

where $\Phi$ is the number of ionizing photons emitted by the central source and $n_H$ is the electron density. It is usually used to estimate the ionization degree of the gas. High values of $U$ could be due to high values of ionizing photons flux or to low density of the gas. The ionization parameter allows to understand the degree of coupling between the AGN radiation field and the E-NLRs gas. It is observed that radiation becomes the dominant source contributing to the gas pressure when $\log U \geq -2$, above this critical value the ENLR spectrum becomes almost independent of the initial ionization parameter and the gas density in the low ionization zone scales as the radiation flux and it produces a constant local ionization parameter. On the other way $\log U \leq -2$ characterized the gas pressure dominated regime in which the ionization parameter is decreases with galactocentric distance within individual ENLR (Davies et al. 2016). The analysis carried out by Thomas et al. 2018 showed ENLRs characterized by an almost constant ionization parameter. The measured values present a little variation of $U$ within $-3.2 \leq \log U \leq -2.6$. Moreover to describe the physical condition in the NLR, it is important to understand the role of dust, indeed the presence of dust grains in the gas clouds can affect their internal structure. In high ionized gas characterized by

$\log U \geq -1.5$, the dust absorption dominates, therefore a large fraction of the ionizing radiation is absorbed by the dust and remitted in IR wavelength band. On the other side, at lower values of $U$, most of the ionizing photons are absorbed by the gas. It is supposed that dust would be on the basis of the regulation mechanism under the high ionizing emissions. Considering a gas cloud in which the value of $U$ on the illuminated face is above the critical value[1], the dust opacity dominates the attenuation of the radiation field, therefore the radiation pressure on the dust grains is larger than the internal pressure of the cloud and this corresponds to a compression of the gas close to the illuminated side and a reduction in $U$. In the inner part of the cloud the value of $U$ decreases further due to the increased amount of dust as long as radiation and gas pressure will balance at specific depth that corresponds to a peculiar value of $U$. This process controls the condition in the part of the cloud where the high ionized gas is present and permits to explain the similar line ratios of the various emission lines regardless of the location of it. Moreover it can explain the uniform value of $U$ inferred from spectroscopy of many type-II AGNs (Netzer 2013).

Another characteristic feature of NLR spectrum is the coronal lines that are observable in infrared wavelength band. They correspond to high ionization lines produced by fine-structure transitions as [N V] $\lambda 14.3\,\mu$m, [Ne VI] $\lambda 7.6\,\mu$m or [Si VI] $\lambda 1.9\,\mu$m. It is supposed that most of the coronal lines are emitted by gas located between the BLR and NLR (fig. 2.2) and the region is characterized by a very high value of $U$.
Recent observations show that ENLRs present different degree of excitation in their structures that can be inferred from emission line ratios. In fig. 2.3 are plotted the spatial profiles of [O III]/H$\beta$ analyzed by Storchi-Bergmann et al. 2018, the value are measured along the ionization axis and in direction perpendicular to it. The plots show that higher ionization values, in the range $0.9 \leq \log [\mathrm{O\,III}]/\mathrm{H}\beta \leq 1.2$, are observed closer to the central axis while lower values of ionization, in the range $0.5 \leq \log [\mathrm{O\,III}]/\mathrm{H}\beta \leq 0.8$,

[1]It correspond to the value of ionization parameter at which the dust dominates the radiation field absorption, it correspond to $\log U \geq -1.5$

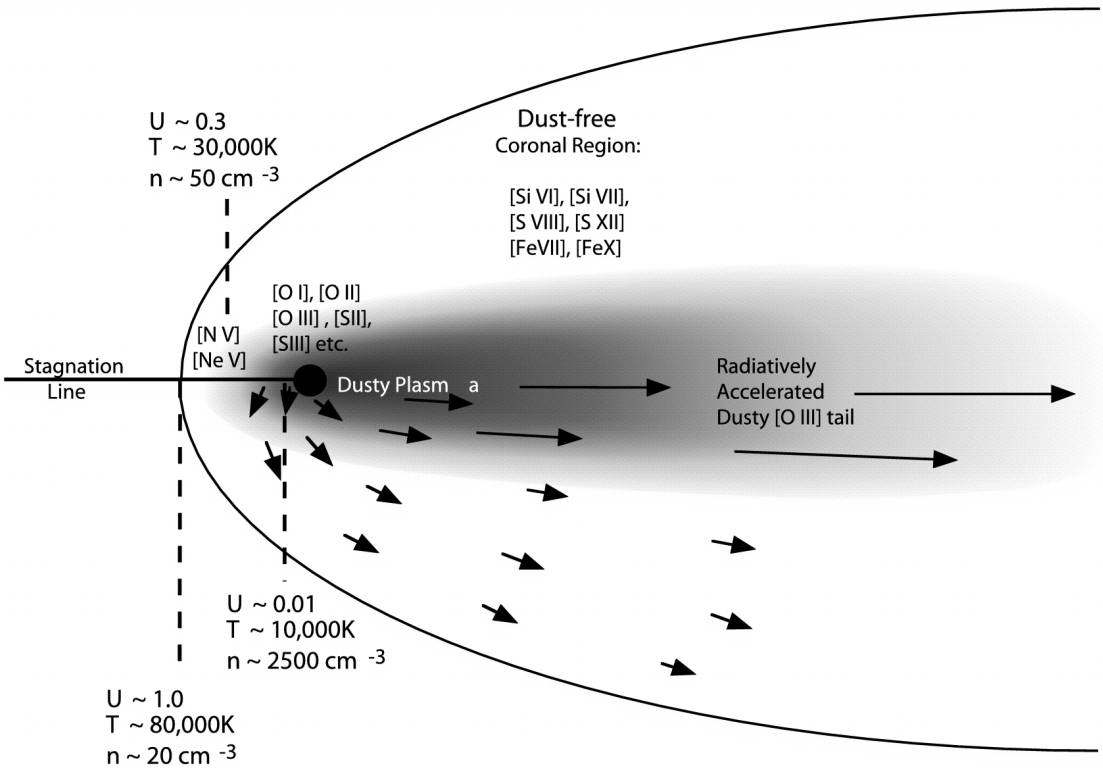


**Figure 2.2:** Theoretical picture showing the dusty model proposed by Dopita et al. 2002 with the parameters marked by dashed lines that indicate the typical values for the object NGC 1068.

are measured in the perpendicular direction confirming the presence of the obscuring dusty torus proposed by the Unification Model.

The ionization parameter associated to the direction of the torus was $\log U \approx -3$ while in the direction of the ionization cones axis was $\log U \approx -2$. This imply that the rate of escaping photons from the ionization cones are 10 times higher with respect to the perpendicular direction, and is a further observation supporting the presence of the torus. Moreover it is observed that the [O III]/H$\beta$ decreases rapidly beyond the limit of the ENLR showing that the region is matter bounded due to the lack of gas at larger distance from center of the galaxy. As evidence of it, in some of the objects observed by Storchi-Bergmann et al. 2018, the radiation field emitted by the AGN reaches gas clouds beyond the limit of the host galaxy disk or in other situations the dimension of the two opposite ionizing cones are not the same. This can be understood as the result

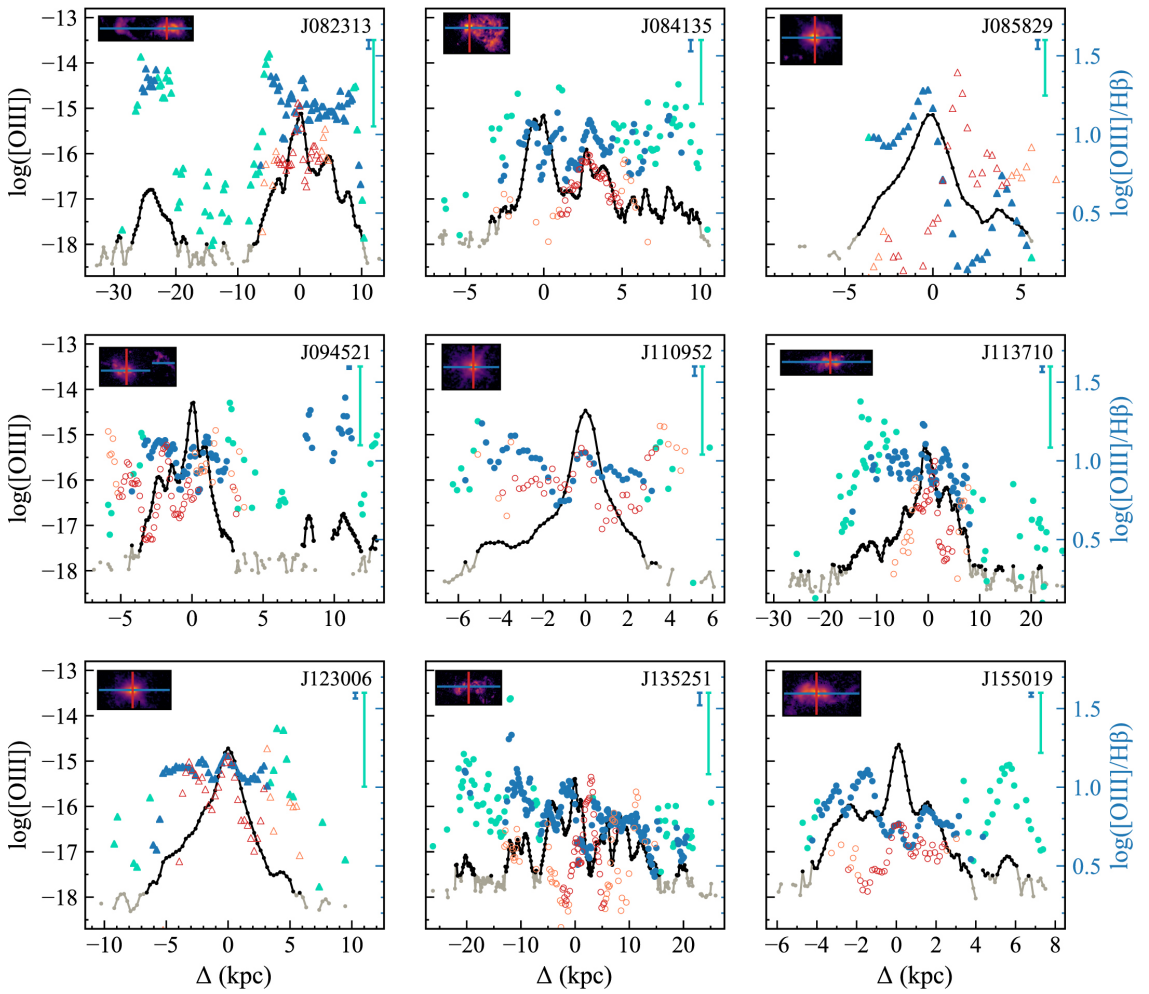


**Figure 2.3:** The images are from Storchi-Bergmann et al. 2018 and plot the [O III] flux (black and grey lines), [O III]/H$\beta$ along the ionization axis (blue and turquoise symbols) and [O III]/H$\beta$ (red and orange symbols) along the direction perpendicular to the ionization axis. The frame on the upper left corner shows the narrow-band images taken with HST, the blue line represents the ionization axis, the red line the direction perpendicular to it.

of merger or interaction processes that product a non-homogeneous distribution of the gas across the galaxy so one of the cones has a limited size due to the lack of gas.

### 2.1.1 Photoionization Models

The number of processes involved in the ionized gas is very huge and to understand ionization and thermal structures of clouds are used photoionization codes throughout numerically solutions. The models have to consider the photoionization and recombi-

nation processes, the thermal balance, the ionizing spectrum, the chemical composition of the gas and the clouds or filaments distribution. Following Netzer 2013 two models are proposed to describe the condition in NLRs: the LOC model and the clouds model. In the first model it is assumed that the density of the gas and thereafter the ionization parameter could be vary within a wide range of values at every location and the entire volume is filled with gas characterized by different densities. The presence of dust, following the process described above, controls the high ionizing emission process and consecutively restricts the range of possible value of $U$. This model, if on one side can explain the spectrum of NLRs, do not permit to understand why the coronal line's emission region, characterized by low-density and high $U$, is dust free gas. The second model is characterized by stratification: the values of density and $U$ at each location are restricted into smaller range with respect to LOC model and it is assumed that the typical gas density distribution drops with distance follows $n_H \propto r^{-s}$ with $s \leq 2$. As a consequence of it, the ionization parameter $U$ decreases with the distance from the center. However this model, as the previous, cannot provide a good explication about the condition of the coronal line's emission region. In order to explain the high level of ionization in the inner part of the NLR others hypothesis are suggested regarded to the alteration of the ionizing SEDs of the radiation field. It is supposed that the presence of low-column density clouds in the inner part of the region could modify the ionizing SEDs and this can produce regions with lower $U$. In this model, the coronal lines are emitted by a region illuminated directly by photons from the central source while more distant regions receive a weaken ionizing radiation field.

### 2.1.2 Kinematics of the ENLR gas

Recent observations, obtained with IFU spectrographs, permitted to analyze the whole ENLRs obtaining a two-dimensional map of velocity and space of the major components of these regions.

The kinematic model of ENLRs is complex but it is possible to simplify it to an out-

flow driven by radiative pressure plus a rotating disk that coincides with the molecular gas disk of the host galaxy. Moreover it is observed that radiation pressure can drive outflow even if it is not dominant across the whole ENLR (Davies et al. 2016).
The analysis of kinematics usually uses two luminous emission lines of ENLRs [O III] and H$\alpha$. The velocity map is based on the total line profile and represents the combination of two different gas kinematics: the narrow component characterized by $\sigma \simeq 100 - 200\,\mathrm{km\,s^{-1}}$ represents the gas that undergoes gravitational potential of the host galaxy while the broad component, $\sigma \simeq 300 - 400\,\mathrm{km\,s^{-1}}$, manifests the AGN outflow. It is observed that the velocity dispersion of [O III] decreases radially outwards until it becomes comparable with the stellar velocity dispersion of the host galaxy. Moreover the size of influence of the outflow is smaller with respect to the photoionized region, not the whole ionized gas shows outflow features, and this can be attributed to the lower efficiency on kinetic energy transport mechanism with respect to photoionization processes (Kang and Woo 2018). Others observations carried out by Fischer et al. 2018 confirm the velocity map proposed above, but suggest the presence of a third component on gas kinematics. Some objects show the emission line [O III] characterized by $200 \leq \sigma \leq 300\,\mathrm{km\,s^{-1}}$ that probably corresponds to gas in rotation with the host galaxy but experiencing some influence from the AGN. These regions are known as *disturbed* kinematic regions.

## 2.2 Luminosity-scale relation

During the last years in order to improve the knowledge of the ENLRs a lot of observations were carried out using different methods and instruments to investigate these structures. One important relation that comes out from observations is the size-luminosity relation, that ties the luminosity of the AGN to the projected dimension of the NLR. The size-luminosity is fitted by the eqn. 2.2 and the parameters $a$ and $b$ for

the different authors are resumed in tab. 2.1.

$$\log R_{NLR} = a \log L_{[OIII]} + b \tag{2.2}$$

The NLR of seven quasar were observed with the Wide Field and Planetary Camera 2 (WFPC2) on board of the Hubble Space Telescope (HST). Images were taken using a linear-ramp filter to obtain the [O III] $\lambda$5007 and trace the NLR. The observations showed the structures were generally symmetric, in agreement with the prediction of Unified Model and it was observed that the size of NLR scales with the square root of the [O III] luminosity (Bennert et al. 2002). Following observations were done employing the same instrument with the aim of analysing the differences of the NLR shape between type-I and type-II Seyfert and again confirms the hypothesis of Unification Model. The sample was composed by 22 type-I Seyfert and 38 type-II Seyfert galaxies. The comparison between the size-luminosity relations of the two classes of Seyfert galaxies shows that the type-I has a steeper slope with a larger uncertainty. The scatter in the correction can be due to projection effects, in those galaxies the conical NLR is closer to the end-on respect to the type-II Seyfert that are closer to edge-on. Moreover it was shown that in type-I the emission is more concentrated towards the nucleus with respect to the more elongated emission of the type-II Seyfert (Schmitt et al. 2003). A different approach was used to study the distribution of the ionized emission around 14 quasar at $z \approx 0.5$. In this case to obtain this result it was employed the Gemini Integral Field Unit characterized by a $5 \times 7$ arcsec field of view, that at $z \approx 0.5$ corresponds to $30 \times 42\,\mathrm{kpc}^2$. This field of view permits a complete observation of the ENLRs and the definition of a better physically motivated boundary which corresponds to the isophotal radius at an intrinsic limiting surface brightness of $10^{-15}\,\mathrm{erg\,s^{-1}\,cm^{-2}\,arcsec^{-2}}$. In order to account for the cosmological surface brightness dimming effects, this value was corrected for the factor $(1+z)^{-4}$. The observations showed a difference of the NLR shape between the radio-quiet and radio-loud objects. The first presents a smoothed

morphology with respect to the more elongated shape of the latter class probably due to the interaction between the radio-jet and the host galaxy's ISM (Liu et al. 2013). In order to improve the understanding of the size-luminosity relation a sample of 8 quasar was observed using long-slit spectroscopy at the Southern African Large Telescope. The spatial extension of the ENLRs was compared to mid-IR luminosity that differently from the [O III] emission, it does not suffer of dust obscuration and depends on the NLR properties. Moreover the mid-IR luminosity is a directly probe of the AGNs luminosity tracing the dust around the central engine. It was shown that IR emission in luminous AGNs strongly correlates with soft X-rays emission (Matsuta et al. 2012). The size of the NLR was measured as in previous IFU observations employing the isophotal radius, and the results are in agreement with others work. As other studies suggested, it was observed that at high AGN luminosity the dimension of the NLR is limited by the finite extent of the gas clouds. The limit size agrees with the host galaxy dimension around $\approx 10 - 12\,\mathrm{kpc}$ (Hainline et al. 2013). Recently long-slit spectra were obtained with the HST/STIS instrument. On a sample of 12 type-II quasar at $z < 0.12$, with the aim to analyze the morphology and the kinematics of ionized gas in these the sources. The targets show different ENLRs morphology, from compact core-like to extended up several kiloparsec structures. It was observed that the inner part of the [O III] emission regions is radially driven, while the external part corresponding to the ENLRs often follows the disk rotation of the host galaxy (Fischer et al. 2018). Fig. 2.4 shows the comparison between the size-luminosity relation described in the various works analyzed above.

A recent work (Storchi-Bergmann et al. 2018), using narrow-band images from HST of 9 luminous type-II AGNs, obtained a different size-luminosity relation closer to the one obtained by Bennert et al. 2002 characterized by $R_{NLR} \approx L^{0.5}_{[OIII]}$. This implies that the sample is characterized by a $U$ almost constant on the ENLRs and a gas density $n_e$ that decreases radially from the center following the relation $n_e \propto R^{-2}$. Moreover, as observed in the analysis carried out by Schmitt et al. 2003, the size-

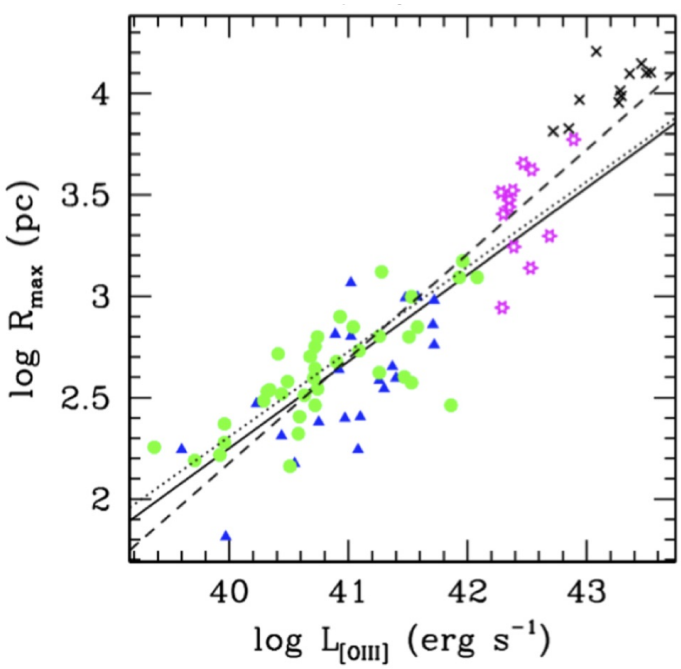


**Figure 2.4:** Image from Fischer et al. 2018. It shows the comparison between projected $\log R_{max}$ of the ENLR and the $\log L_{[OIII]}$ for type-I Seyfert (blue triangles) and type-II Seyfert (green circles) from Schmitt et al. 2003, type-II quasar (black x) from Liu et al. 2013 and type-II quasar (magenta star) from Fischer et al. 2018.

luminosity relation of the type-I AGNs results more steeper with respect to the type-II AGNs. The methods seen before employed spectroscopy and narrow-band filter images techniques, but in the last years it was developed a new strategy using broad-band images that permitted the analysis of a larger number of objects. It was observed that the strong emission lines of [O III] $\lambda\lambda$4959,5007 create flux excess in broadband images that allows to distinguish them from the normal galaxies. In order to reconstruct the [O III] distribution images from Subaru Hyper Suprime-Cam (HSC) and SDSS spectra were used. The SDSS spectra allowed to obtain a scaling factor in order to create a continuum subtraction model and also to quantify the contamination of other emission lines with respect to the [O III]. The estimate of [O III] emission region's size was possible through the isophotal radius, that permits more adaptive measurements to the irregular morphology of ENLRs region. Previous relations show that more luminous AGNs create larger emission line regions (Sun et al. 2018).

| Article | $a$ | $b$ |
|---|---|---|
| Bennert et al. 2002 | $(0.49 \pm 0.06)$ | $(-17.5 \pm 3.4)$ |
| Schmitt et al. 2003 | Syf-2 $(0.31 \pm 0.04)$ | $(-10.8 \pm 1.8)$ |
| | Syf-1 $(0.41 \pm 0.08)$ | $(-14.6 \pm 3.45)$ |
| Liu et al. 2013 | $(0.250 \pm 0.018)$ | $(+3.746 \pm 0.028)$ |
| Fischer et al. 2018 | $(0.42)$ | $(-14.45)$ |
| Storchi-Bergmann et al. 2018 | Syf-2 $(0.48 \pm 0.03)$ | $(-17.1 \pm 1.1)$ |
| | Syf-1 $(0.57 \pm 0.06)$ | $(-20.7 \pm 2.0)$ |
| Sun et al. 2018 | $L_{[OIII]}$ $(0.20 \pm 0.03)$ | $(-7.69 \pm 1.22)$ |
| | $L_{bol,15\mu\mathrm{m}}$ $(0.64 \pm 0.06)$ | $(-27.61 \pm 2.70)$ |

**Table 2.1:** The $a$ and $b$ parameters of the size-luminosity relations for the different observations. The second relation proposed by Sun et al. 2018 $L_{bol,15\mu}$ represents the bolometric luminosity calculated as $L_{bol,15\mu} = 9 \times L_{15\mu}$ on the basis of the area of the isophote expressed in $kpc^2$.

Following the unification scheme, the number of AGNs showing an ENLR would be large but notwithstanding recent observations with different instruments, it was possible to detect, map and study in detail only around 50 ENLRs at $z \approx 0.05$ (Netzer 2015). The small number of observed ENLRs could be related with the difficulty in finding them, first of all the presence of ionization cones is directly related to the presence of gas to be ionized, obviously if it is not present these regions cannot be observed, and second it is present an observational bias that is the reduction of the angular extension on the sky of the ENLRs due to the distance of the sources that does not permit their identification. With the aim to discover more ENLRs and improve their knowledge more detailed observations are necessary through narrow-band images or broad-band images surveys that until now are not present in literature. In order to carry out that surveys it is necessary a sample of AGNs candidate. Following Vaona et al. 2012 in which it was selected a sample of AGNs in the northern sky to study the spectroscopic properties of the nearby type-II Seyfert galaxies from a statistical point of view, in this work we have selected a completely new sample of type-II AGNs from the southern hemisphere, with the specific aim to look for new ENLRs.

# Chapter 3

# Sample selection and measurements

The emission line galaxies are generally classified in the optical range using the diagnostic diagrams (Veilleux and Donald E. Osterbrock 1987, Baldwin, Phillips, and Terlevich 1981). In this work we decided to use the [O III]/H$\beta$ vs [N II]/H$\alpha$ diagram, that permits to separate the AGNs from the others galaxies. This diagram is sensible to the measurements of the Balmer lines due to the presence of a stellar continuum underlying the emission spectrum. This stellar component leads to underestimate the flux of H$\beta$ and H$\alpha$ emission lines. The effect is an overestimation of the flux ratio, so it is necessary to correct the spectrum for the stellar absorptions in order to obtain a correct classification of the galaxies. Moreover, the H$\alpha$ emission line is less sensible to the stellar absorption respect to the H$\beta$ so, after the correction, the points on the diagram move down and slightly to the left. This means that, without an accurate correction, starburst galaxies could contaminate the section of the diagram that contains AGNs. The aim of this thesis is to select a sample of type-II AGNs in the southern sky and to analyse some of the characteristics of the ENLR testing the size-luminosity relation. Differently from northern sky, the number of all-sky spectroscopic surveys in the southern hemisphere is less. The spectra used in this work were carried out by Six Degree Field Galaxies Survey[1] (6dFGS) and by Sloan Digital Sky Survey[2] (SDSS).

[1] http://www.6dfgs.net
[2] http://skyserver.sdss.org/dr15/en/home.aspx

## 3.1 Sample selection

In following sections it is described the method used to obtain the samples from the two galaxies survey. The fig. 3.1 shows two plots that describe the samples of the sources selected from the surveys. The plot on the right give a direct image of the distribution of the galaxies ties to the redshift and is possible to observe that the SDSS sources show a more homogeneous distribution with respect to the 6dFGS while the left plot shows the distributions on the sky of the sources.

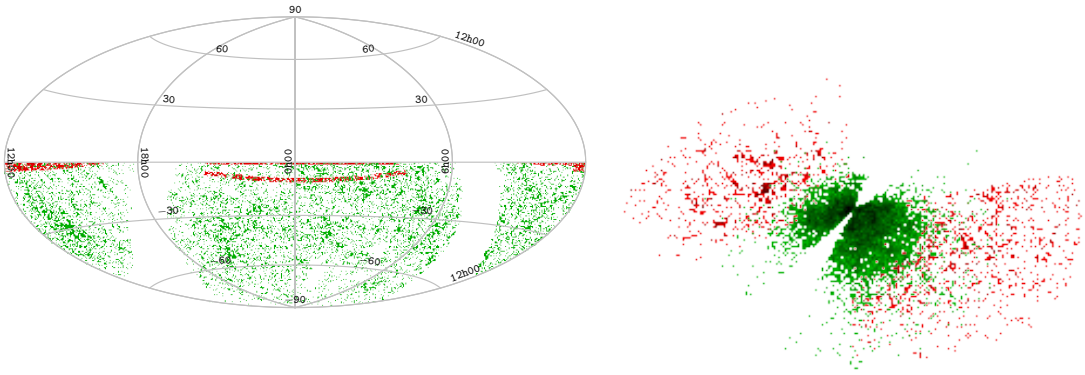


**Figure 3.1:** On the left, the distribution of the selected sources projected on the sky, on the right the distribution with respect to the redshift $z$. The SDSS sample is represented in red, while the 6dFGS is represented in green.

### 3.1.1 Six Degrees Field Galaxy Survey

The aim of this survey was to measure the redshift and the peculiar velocities of a sample of galaxies of the southern sky. The Final Redshift Release (DR3) contains the spectra of 136304 galaxies. The observations were carried out using the Six Degree Field fibre-fed multi-object spectrograph at the UK Schimidt Telescope (UKST) over 2001 May to 2006 January. The target field covered around $\sim 17000\,\mathrm{deg}^2$ of the southern sky, to mitigate the effect of high Galactic extinction correction all the observations were limited at $b > 10°$ from the Galactic plane (Jones, Read, et al. 2009).

The 6dFGS spectrograph could obtained 150 simultaneous spectra across the 5.7°

**Figure 3.2:** The UKST telescope of the Anglo-Australian Observatory.

of the UKST. Each field plate contained 154 fibers but four of them were used as guide fiber. Each science fiber had a dimension of 100 $\mu$m that corresponded to 6.7 arcsec and to a projected size on the sky of 4.8 $h^{-1}$ kpc at $z = 0.053$ that was the medium redshift yielded by observation. It is important to note that during the four years of observations the gratings of the two arms of the spectrograph were changed. All data taken before October 2002 used a 600V and 316R reflection gratings covering 4000-5600 Å and 5500-8400 Å respectively. For the data taken after, to improve the efficiency, focus and data uniformity, VPH transmissive gratings 580V and 425R were used covering a different wavelength range 3900-5600 Å and 5400-7500 Å respectively. In addition, it is important to underline that they were not flux calibrated (Jones, Saunders, et al. 2004). The preliminary selection of our sample was made using the parameters available on the survey query. The parameters used are summarized in tab. 3.1: *targetName* is an identification code of the spectra, *ra* and *dec* are the positions of the object in the sky expressed in degrees, $z$ is the redshift of the object, $A_V$ the Galactic extinction in V-band and *NGOOD* corresponds to the number of good emission lines in the spectrum. The preliminary sample selection was obtained assuming $dec \leq 0$, $NGOOD \geq 2$ and $0 \leq z \leq 0.14$.

The limit imposed to the maximum redshift is due to spectral range of the obser-

| targetname | ra | dec | $A_V$ | z | ngood |
|---|---|---|---|---|---|
| g0008227-295413, | 2.094 | -29.904 | 0.05 | 0.0053 | 5 |

**Table 3.1:** Example of output obtained by query searching of 6dFGS, the sky coordinate are expressed in degrees.

vations. Most of the 6dFGS spectra in R-band are limited to the wavelength range of 5400-7500 Å and to classify the galaxies through the diagnostic diagram at least 4 emission lines are needed, so $z = 0.14$ is the maximum redshift at which both H$\alpha$ and [N II] lines are visible in the spectrum. The selected objects from 6dFGS survey are 12737 and in fig. 3.3 it is possible to observe the distribution with respect to $z$ and $S/N$[3]. One is characterized by a mean value of $z = 0.03$ the other $S/N = 12$. Thanks to the cosmological calculator[4] created by Wright 2006 at a given redshift $z$ is possible to associate a linear dimension of the angular aperture of the fiber. The 6dFGS fibers have a projected aperture of 6.7 arcsec. It means that the observed light of nearer objects come from the inner part of the objects and only a small part of the ENLR can be observed that correspond to $2.8 - 19$ kpc in our redshift interval, and 4.2 kpc at the medium redshift $z = 0.03$.

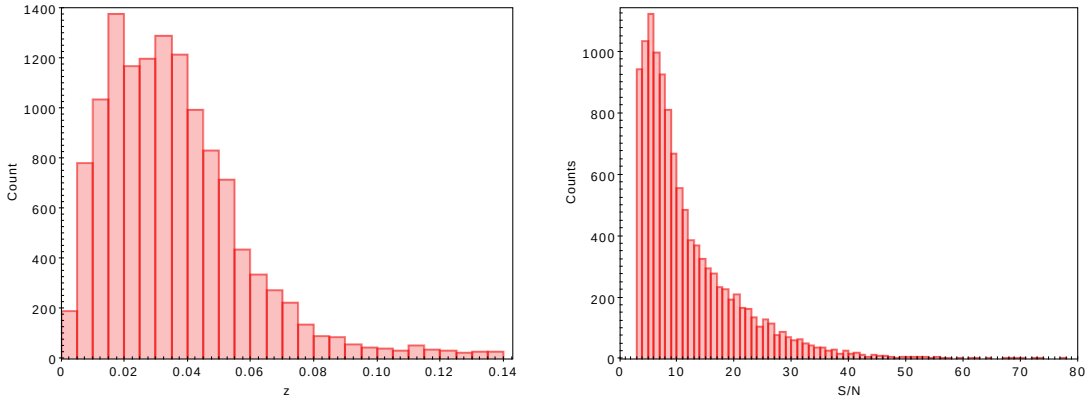


**Figure 3.3:** On the left, the redshift distribution of the preliminary 6dFGS sample, on the right the $S/N$ distribution.

[3]S/N of an observation correspond to the ratio between the *signal* of the source and the *noise* of the sky and instrumentation

[4]The cosmological constant used are $H_0 = 69.6$ , $\Omega_\Lambda = 0.714$ and $\Omega_M = 0.286$ (Bennett et al. 2014)

### 3.1.2 Sloan Digital Sky Survey

The Sloan Digital Sky Survey (SDSS) started regular survey operations in 2000, after a decade of design and construction. The program was composed by several phases, SDSS-I (2000-2005), SDSS-II (2005-2008), SDSS-III (2008-2014) and SDSS-IV (2014-). The data used in this thesis were obtained during the first phase of this program and are organized on the SDSS Legacy Survey[5]. The SDSS telescope, in fig. 3.4, has a diameter of 2.5 m and it is located at Apache Point Observatory, New Mexico.

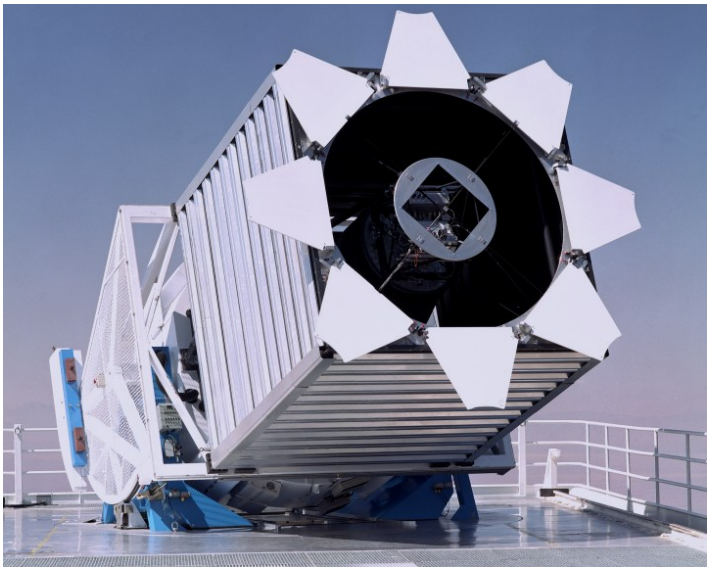

**Figure 3.4:** The telescope at Apache Point Observatory used by the SDSS survey programs.

It is equipped with two powerful instruments:

- the 120 megapixel camera with the possibility to capture 1.5 $\deg^2$ of sky for each observation, that correspond to about eight times the area of the full moon
- a pair of optical fibers spectrographs able to obtain the spectra of more than 600 sources in a single observation

The SDSS Legacy Survey provided a uniform, well calibrated map in *u-g-r-i-z* and associated spectra of more than 7.500 $\deg^2$ of the North Galactic Cap, and three stripes

[5]https://classic.sdss.org/legacy/index.html

in the South Galactic Cap totaling 740 $\deg^2$. The data used in this work, are carried out by the observation of the three stripes in the South Galactic Cap. The wavelength range of these spectra is larger that of 6dFGS, it extends from 3800-9200 Å. The preliminary selection of the objects from this survey was done using the parameters available on the survey query. The parameter used summarized in tab. 3.2: *specobjid* is an identification code of the spectra, *ra* and *dec* are the positions of the object in the sky expressed in degrees, $z$ is the redshift of the source, *class* is the classification of the object and *flux* of the most intense emission lines used in the selection process. The preliminary sample selection was obtained assuming $dec \leq 0$, $fluxes \geq 0$ and $0 \leq z \leq 0.2$. The limit on $z$ is fixed at that value in order to avoid that the H$\alpha$ and [N II] lines are out from the wavelength range. The number of objects selected in this way is 36315.

| specobjid | ra | dec | class | $z$ | flux [O III] |
|---|---|---|---|---|---|
| 341173262513891328 | 213.819 | -0.661 | Seyfert | 0.11 | 25.68313 |

**Table 3.2:** Example of output obtained by query searching of SDSS where only one emission lines is represented. The flux unit is $10^{-17}\,\mathrm{erg\,cm^{-2}\,s^{-1}}$ and the sky coordinate are expressed in deg.

In order to isolate the type-II Seyfert and the Intermediate-type Seyfert galaxies from we followed the work of Vaona et al. 2012 used the Oxygen diagram ($O_{123}$ diagram).

This diagram is based on [O II] $\lambda$3727/[O III] $\lambda$5007 ($O_{23}$) and [O I] $\lambda$6300/[O III] $\lambda$5007 ($O_{13}$) lines ratio and it is plotted in fig. 3.5.

The $O_{23}$ ratio represents a measure of the ionization level, and it was already used in the new diagnostic diagram proposed by L. J. Kewley et al. 2006. The $O_{13}$ instead is a tracer of the hardness of the photoionization field at large radii from the source. The advantages to use the $O_{123}$ diagram are the fact that the Oxygen lines are visible in all AGNs spectra and it is the only element for which it is possible to observe three different states of ionization in the optical range, moreover the emission lines are not

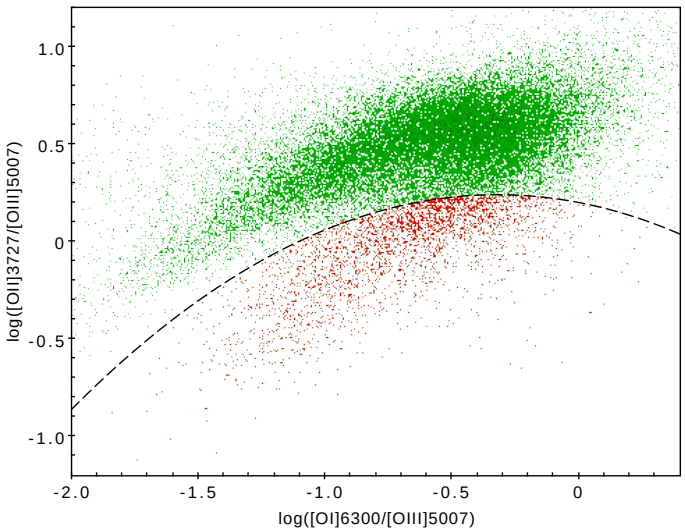


**Figure 3.5:** $O_{123}$ diagram of 36315 galaxies selected from the SDSS. The dashed line represents the separation (eqn. 3.1) between star-forming galaxies (above the line) and AGNs (below the line) as explained in the text.

contaminated by stellar spectral and this permits to use the $O_{123}$ diagram without the subtraction of any stellar template. The disadvantages of this diagram are the fact that [O I] is a weak line and the ratios are not correct for reddening. The preliminary SDSS sample selection was plotted on the $O_{123}$ diagram and using the polynomial function 3.1 it was possible to select the AGNs sample.

$$\log O_{23} = 0.20 - 0.25 \times \log O_{13} - 0.39 \times \log O_{13}^2 \tag{3.1}$$

In fact, this plot can distinguish AGNs from starburst galaxies (Vaona et al. 2012), the lower sequence therefore contains type-I and type-II AGNs and LINERs objects that have to be separated using another method. The sub-sample obtained is composed by 2755 sources, and is characterized by a lower limit in redshift because the [O II] line must be visible in the spectrum that corresponds to objects with $z \geq 0.02$.

In fig. 3.6 it is possible to observe the distribution of the sources with respect to $z$ and $S/N$ for both the preliminary and the $O_{123}$ diagram selection. The redshift distributions are quite similar and are characterized by a mean $z \approx 0.1$. The SDSS fiber aperture corresponds to a projected dimension in the sky of 3 arcsec. Following

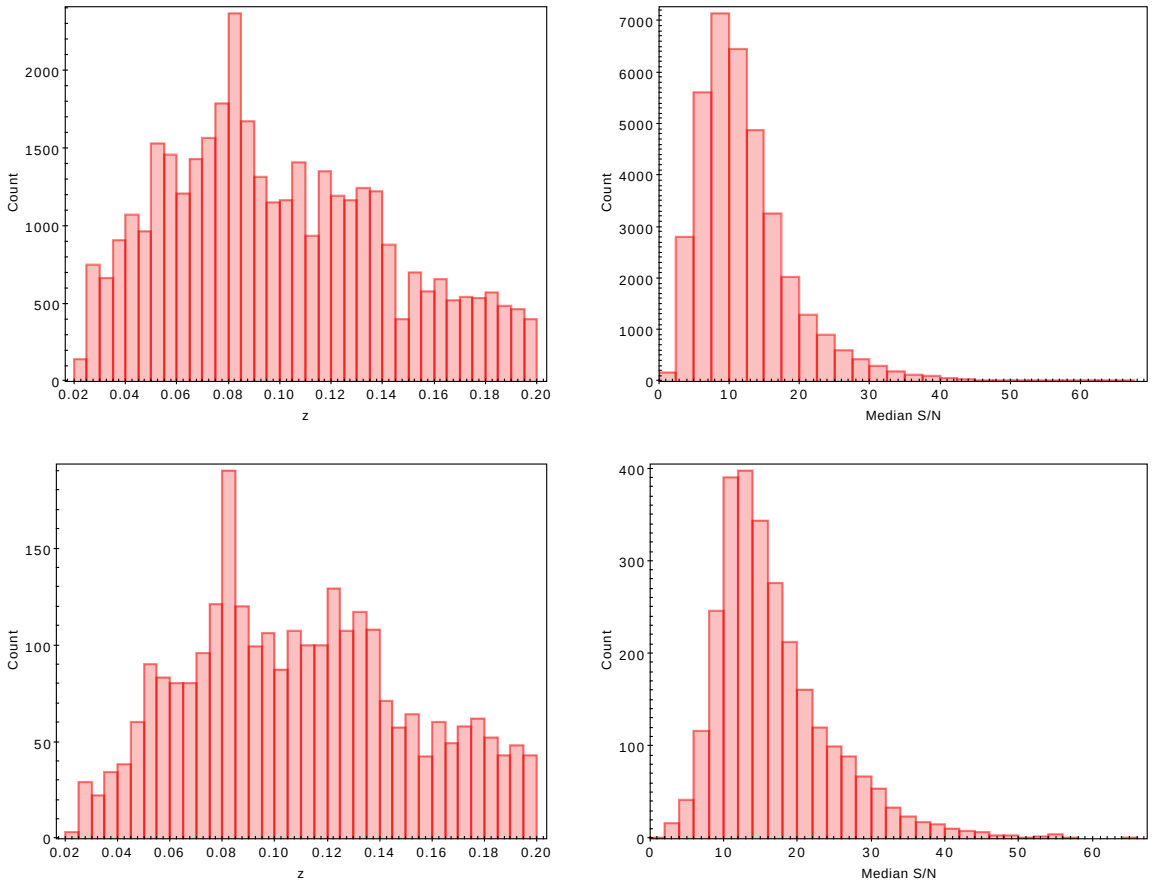


**Figure 3.6:** On the top left the $z$ distribution and on the top right the $S/N$ distribution of the preliminary selected sample from SDSS, on the bottom left the $z$ distribution and on the bottom right the $S/N$ distribution of sample after the application of the $O_{123}$ diagram.

the method used in the 6dFGS survey, the adopted redshift range corresponds to $1.24 - 11.9\,\mathrm{kpc}$, and the medium redshift $z$ correspond to $6.1\,\mathrm{kpc}$. Again, also in that case the observed light come from the inner part of the objects, and only the inner part of the ENLR is observed. The $S/N$ of the AGNs sample is characterized by an higher medium value around 16 with respect to preliminary selected one, it means that the majority of the spectra are of acceptable quality.

## 3.2 Preparation of the spectra

The following steps concern the fitting and the subtraction of the underlying stellar continuum for each spectrum. This is done using the spectral synthesis code STARLIGHT (Roberto Cid Fernandes et al. 2005). The model is described by the eqn. 3.2, it makes a linear combination of synthetic spectra which are reddened and then convolved with a broadening function to obtain the stellar dispersion velocity.

$$M_\lambda = \sum_{j=1}^{N} L_{\lambda,j} = \sum_{j=1}^{N} L^0_{\lambda,j} \otimes G(v_*, \sigma_*) 10^{-0.4 A_{\lambda,j}} \tag{3.2}$$

In the eqn. 3.2 $M_\lambda$ is the final model obtained by the sum of N spectra, $L_{\lambda,j}$ is the spectrum of population j, $L^0_{\lambda,j}$ is the j-population spectrum without extinction nor kinematics, $G(v_*, \sigma_*)$ is a Gaussian filter centered at $v_*$ and dispersion $\sigma_*$ and $10^{0.4 A_{\lambda,j}}$ is the extinction correction, where $A_{\lambda,j}$ is the j-population extinction at $\lambda$. The input spectra required some pre-processing before being ready for use within the code: the spectra have to be flux calibrated and corrected for Galaxy extinction and redshift. These processes are done using IRAF packages.

### 3.2.1 Flux calibration

The first step consisted in the flux calibration of the 6dFGS sample using the object's spectra that were observed by both the analyzed surveys. The procedure used in this work is similar to the method proposed by Chen et al. 2018 and applied for the first time to a narrow-line type-I Seyfert sample of the southern hemisphere. The objects searching process is based on a coordinates match between the two spectroscopic survey databases within a tolerance range of 3 arcsec. The images of the sources in both surveys were compared manually to make sure that the objects observed were the same. This search resulted in 35 galaxies in common. The header of the 6dFGS spectra do not present some important data about the observation that are needed for the flux calibration, so the *exposure time* and the *airmass* value were calculated for

each spectrum. The exposure time was calculated by multiplying the number of frames for the exposure time of each frame, the airmass value was obtained from the location of the observatory and the observation time. The next step consisted in the creation of a sensitive function with the SDSS spectra using the IRAF task: STANDARD and SENSFUNC. STANDARD is configured to use the spectra sampled by some bandpasses, so it was first applied the task SBAND to prepare the SDSS and the 6dFGS spectra database. Each spectrum was sampled using bandpasses characterized by a band-width of 50 Å, moreover the fluxes thorough them have to be expressed in AB magnitude. The eqn. 3.3 converts the fluxes in magnitude, where $f_\lambda$ corresponds to the flux and $m_{AB}$ the magnitude.

$$m_{AB} = -2.5 \log \frac{f_\lambda \cdot \lambda^2}{3} + 38.9 \tag{3.3}$$

The SDSS spectra of the objects selected before were used as standard catalogue and the 6dFGS spectra as the observed ones. In this procedure the 6dFGS spectra are integrated over calibration bandpasses and written into an output file along with the associated calibration fluxes. The output data are used by the task SENSFUNC to determine the sensitivity function. The following step consisted in a manual check of the sensitivity function of each object to delete the ones that do not present a coherent shape with the others and finally they were combined together to obtain a median correction for the V-part and the R-part of the spectra. It is supposed that due the fact that the primary purpose of the 6dFGS survey was a redshift and peculiar velocity analysis of the nearby galaxies, the photometric calibration was not a priority and some observations could do in not optimal condition of sky and in different nights for the V-part or the R-part of the same object spectrum. This justification may explain the fact that some V-spectra and R-spectra could not be perfectly attached together. Finally the spectra were flux-calibrated using the task CALIBRATE and the V-part and R-part attached together using SCOMBINE.

### 3.2.2 Extinction and Redshift correction

The Galactic extinction absorption due to the presence of diffuse interstellar medium was corrected using the task DEREDDEN, the $A_V$ extinction values are calculated using a tool from NED[6]. The dust mapping used by the tool are from Schlegel, Finkbeiner, and Davis 1998. The spectra were shifted to the rest frame with the task NEWREDSHIFT by using the $z$ value given from the SDSS and 6dFGS database and re-gridded to a dispersion 1 Å/px with DISPCOR. Finally all they were converted into text format using WSPECTEXT and given as input to STARLIGHT.

### 3.2.3 Continuum Fitting

The base used by STARLIGHT to fit the galaxies continuum was composed by 150 different stellar spectra combining 25 different ages from $10^6$ yr up to $18 \times 10^9$ yr and 5 metallicities $Z = 0.05,\ 0.02,\ 0.008,\ 0.004,\ 0.001\ Z_\odot$. The extinction function used corresponds to the Cardelli, Clayton, and Mathis 1989. The emission lines were masked in order to improve the quality of the fit. In order to obtain a pure emission line spectrum the best-fitting synthetic model of the continuum for each galaxy was subtracted from the observed one (fig. 3.7).

Before to proceed with the spectra analysis both the 6dFGS and SDSS spectra were visually selected in order to delete the ones that did not show any emission lines or with a bad continuum subtraction. At the end of this procedure the selected spectra for the 6dFGS were 3999, for the SDSS 929. The S/N ratio of the new selected sample was about 14 for 6dFGS and about 25 for SDSS. The low value for the 6dFGS is due to the lower quality of the spectra.

[6]NASA/IPAC Extragalactic Database https://irsa.ipac.caltech.edu/applications/DUST/

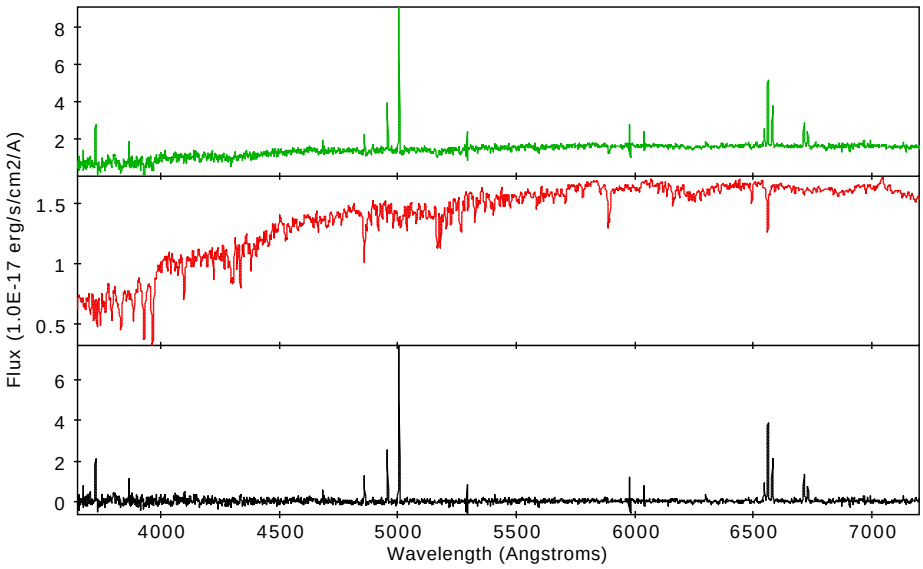


**Figure 3.7:** Example of the correction for stellar component for the source 2MASX J20414157-0526075 (in our sample it correspond to the SDSS spectrum spec-0634-52164-0586). From the top to down the original spectrum (green), the fit of the stellar component (red) and the residual pure emission-line spectrum (black) are plotted.

## 3.3 Emission Lines Fitting

The emission lines were fitted with a dedicated code written in *Python*. It was developed employing *astropy.modelling* package. In order to obtain a classification of the galaxies at lest four emission lines are needed , [O III] $\lambda$5007, H$\beta$ $\lambda$4861, [N II] $\lambda$6584 and H$\alpha$ $\lambda$6563. The model used for the fitting is composed by a sum of three Gaussian curves. It measures the Gaussian peaks and their FWHMs with a linear interpolation after the subtraction of the continuum. The fitting procedure used in the two samples was quite different. The 6dFGS fitting code is divided in two parts, one centered on the H$\alpha$ emission line and fitting also the two emission lines of [N II], the second centered on H$\beta$ emission line and measuring also the two emission lines of [O III] $\lambda\lambda$ 4959,5007. Each code fits the emission lines with two different FWHMs: one for the Balmer lines of each part and one for [O III] and for [N II]. The SDSS code is divided in two parts too, but the fitting procedure applied three Gaussian curves characterized by the same FWHM. Examples are plotted in fig 3.8. The first four plots show the fitting procedure on some SDSS spectra, on the left it is represented the blue section of the spectrum

while on the right the red section. The two plots on the top show a successful fitting procedure, while the two in the middle present an unsuccessful fitting. Moreover the fourth plot show an additional broad component of H$\alpha$ that is not fitted by the code. In order to obtain a correct fitting of this component the model was modified with a further Gaussian curve as it is possible to observe in the two plots on the bottom of fig. 3.8. This fitting procedure was applied to the AGNs selected sample which will be described in the next chapter.

The continuum was evaluated with a linear interpolation because, due to the correction for stellar component, the baseline mean value is about zero. The code returns a table for all the measured spectra, each line corresponds to an object and contains the fluxes, the FWHMs and the relatives errors of the measured emission lines. The flux $f$ of each fitted emission line is obtained using the eqn. 3.4 where $I_0$ is the peak of the Gaussian fit.

$$f = I_0 \frac{FWHM}{2.355} \sqrt{2\pi} \tag{3.4}$$

The errors related to flux and FWHM are calculated apply a Monte Carlo method during the fitting procedure: a random Gaussian noise characterized by $\sigma = rms$ of the continuum near the emission line was added to the original spectrum.
This method was repeated 100 times in order to obtain enough measures of each parameters. The mean value of them is the measure, the standard deviation is the associated error. The measures are reported in appendix A. The fitting procedure is successful for 858 SDSS spectra and for 3893 spectra of the 6dFGS. Some spectra presented weak emission lines and low $S/N$ and this is supposed to be problem for a correct fitting procedure.

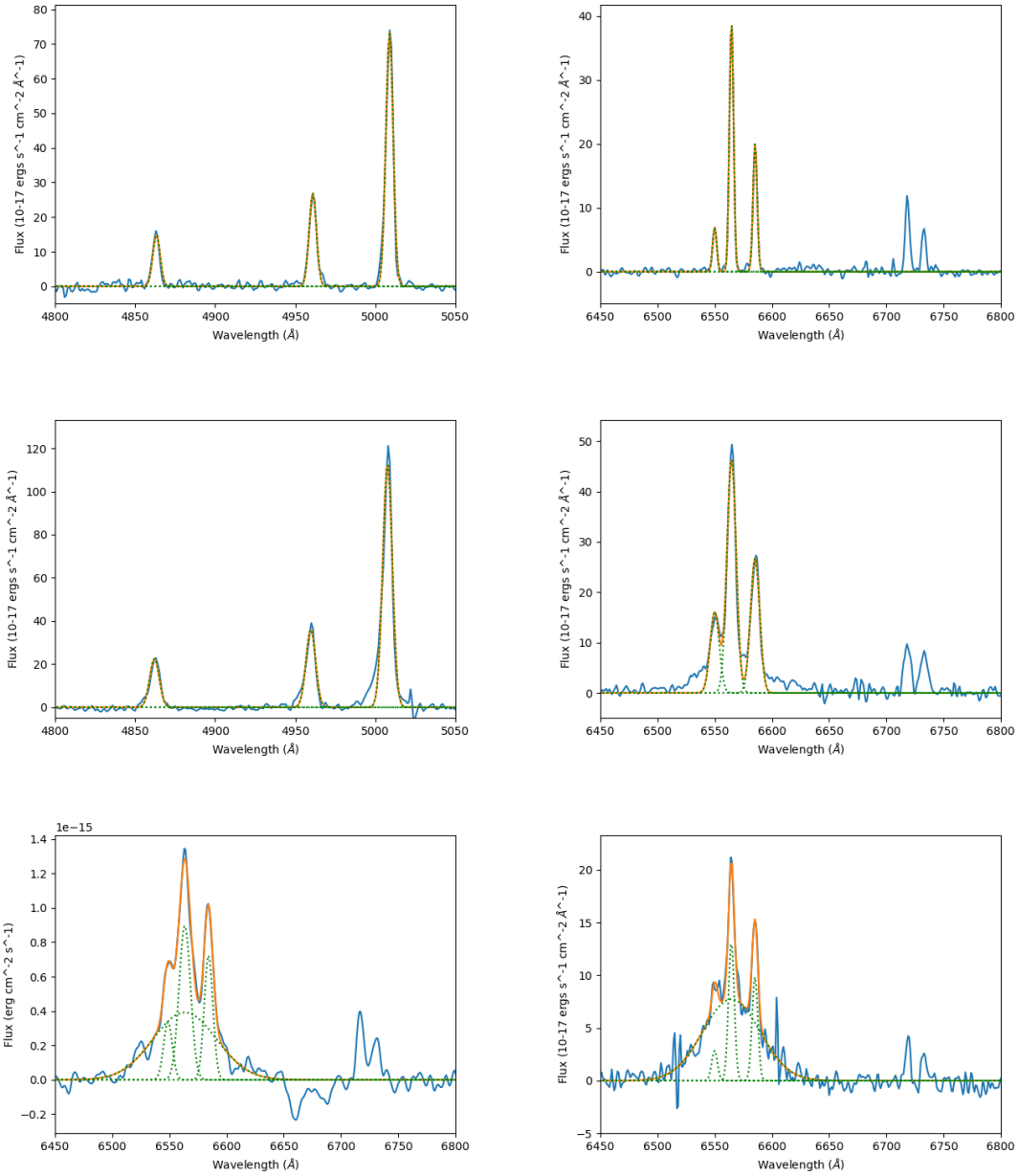


**Figure 3.8:** The images in the first two rows show the results of the fitting procedure of the SDSS sample, the blue line represents the spectrum, the orange line the output from the fitting procedure and the dashed green line shows the flux of each emission line. On the left, the fitting of the H$\beta$ and [O III] lines, on the right the fitting of H$\alpha$ and [N II]. On the top it is shown the successful procedure, on the bottom the examples of not perfect fitting of the emission lines. The two images in the last row show the fitting of the broad component for the H$\alpha$ emission line: on the left an example of a spectrum from the 6dFGS, on the right an example from the SDSS.

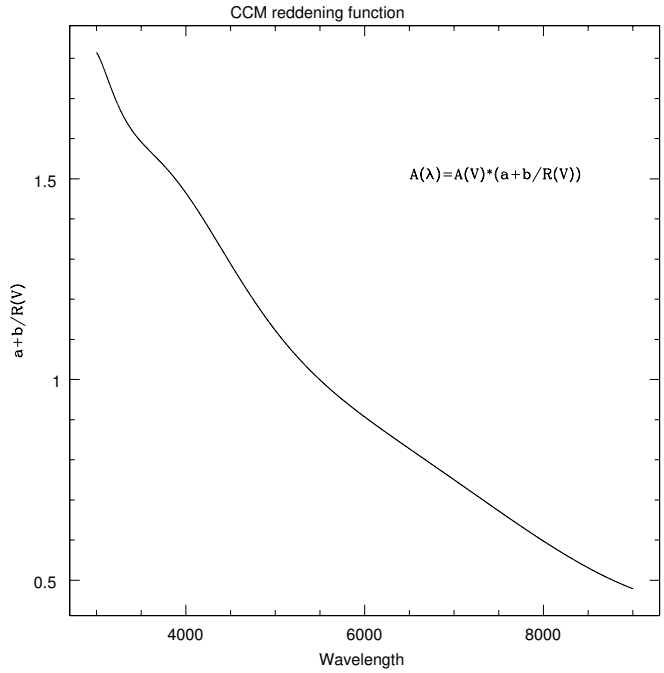


**Figure 3.9:** Extinction law dependence with respect to wavelength (Cardelli, Clayton, and Mathis 1989).

## 3.4 Fluxes Reddening correction

The last step was the reddening correction of the measured fluxes (*dereddening*). Reddening is due to diffuse interstellar medium (ISM) located between the source and the observer. The ISM is mainly composed by H, $H_2$, free electrons, various molecules and grains of dust. The interaction between ISM and photons is wavelength dependent and can be represented by the relation plotted in fig. 3.9.

The extinction is identified by the letter $A(\lambda)$ and usually it is related to the reference extinction in V-band ($A_V$). Here the intrinsic flux is expressed as $F_\lambda$, while the observed one as $f_\lambda$. The theoretic ratio of Balmer lines $H_\alpha$ e $H_\beta$ is given by the eqn. 3.5:

$$\frac{F_\alpha}{F_\beta} = 2.86 \tag{3.5}$$

The observed ratio value, due to the reddening, is higher than the intrinsic one.

The intrinsic and observed values are strictly related by eqn. 3.6.

$$\frac{F_\alpha}{F_\beta} = \frac{f_\alpha}{f_\beta} 10^{-0.1384(A_V)} \tag{3.6}$$

With the aim of calculate $A_V$ for each galaxy, from the eqn. 3.6 it is possible to obtain the eqn. 3.7.

$$A_V = \frac{1}{0.1384}\left(\log\frac{f_\alpha}{f_\beta} - \log\frac{F_\alpha}{F_\beta}\right) \tag{3.7}$$

In order to correct the observed fluxes, using the eqn. 3.8, it is possible to obtain the extinction's value of each emission line. This relation was studied for a limited wavelength range $0.125\,\mu\text{m} \leq \lambda \leq 3.5\,\mu\text{m}$ (Cardelli, Clayton, and Mathis 1989). The parameters used in eqn. 3.8 are obtained with the equations reported below and listed tab. 3.3, where $y = x - 1.82$ with $x = \frac{10000}{\lambda}$ and $\lambda$ is expressed in Å.

$$A(\lambda) = (A_V)(a_y + \frac{b_y}{R_v}) \tag{3.8}$$

$$a_y = 1. + 0.17699y - 0.50447y^2 - 0.02427y^3 + 0.72085y^4 + 0.01979y^5 - 0.77530y^6 + 0.32999y^7$$

$$b_y = 1.41338y + 2.28305y^2 + 1.07233y^3 - 5.38434y^4 - 0.62251y^5 + 5.30260y^6 - 2.09002y^7$$

| $\lambda$ | y | $a_y$ | $b_y$ |
|---|---|---|---|
| $H_\beta$ | 0.237 | 1.015 | 0.461 |
| [OIII]5007 | 0.177 | 1.016 | 0.323 |
| $H_\alpha$ | -0.296 | 0.909 | -0.282 |
| [NII]6584 | -0.301 | 0.907 | -0.286 |

**Table 3.3:** Parameters employed in the flux reddening correction.

This operation of reddening correction was applied to all the fluxes measured with the linear fit. The intrinsic flux ratios were calculated with the eqn. 3.9, where with

$\lambda_1$ and $\lambda_2$ are the wavelength of the two emission lines.

$$\frac{F_{\lambda_1}}{F_{\lambda_2}} = \frac{f_{\lambda_1}}{f_{\lambda_2}} 10^{0.4(A(\lambda_1)-A(\lambda_2))} \tag{3.9}$$

## 3.5 Errors estimation

The errors associated to the measures obtained by the fitting process were calculated directly from the code. In order to obtain an estimation of errors for the others quantity described above, the propagation error theory (eqn. 3.10) was applied: considering a function $G(x, y)$ its associated error is $\sigma_G$, $\sigma_x$ and $\sigma_y$ are the errors related to the variable x and y. This procedure permitted to calculate the errors of $\log R = \frac{F_1}{F_2}$ (eqn. 3.11) where $F_1$ and $F_2$ are the reddening corrected fluxes.

$$\sigma_G{}^2 = \left(\frac{\delta G}{\delta x}\right)^2 \sigma_x{}^2 + \left(\frac{\delta G}{\delta y}\right)^2 \sigma_y{}^2 \tag{3.10}$$

$$\sigma_{\log R}{}^2 = \left(\frac{1}{F_1}\right)^2 \sigma_{F_1}{}^2 + \left(-\frac{1}{F_2{}^2}\right)^2 \sigma_{F_2}{}^2 \tag{3.11}$$

# Chapter 4

# Results and Discussion

In the previous chapter the methods used for the object's selection from the surveys and for the emission lines fitting were explained. These processes were needed to obtain the flux ratios to plot in the diagnostics diagram and discern the AGNs from the others sources.

## 4.1 Samples selection

The fitting process permitted to obtain the fluxes of the most luminous emission lines. The selection of the galaxies was subsequently done using the diagnostic diagram [O III] $\lambda$5007/H$\beta$ vs [N II] $\lambda$6584/H$\alpha$. This diagram, using the relations introduced by L. J. Kewley et al. 2006 (Ke01, Ka03) and R. Cid Fernandes et al. 2010 (Fe10), permits to classified galaxies in four classes:

$$\textbf{Ke01} \qquad \log \frac{[\mathrm{O\,III}]}{\mathrm{H}\beta} = 0.61/(\log \frac{[\mathrm{N\,II}]}{\mathrm{H}\alpha} - 0.47) + 1.19 \tag{4.1}$$

$$\textbf{Ka03} \qquad \log \frac{[\mathrm{O\,III}]}{\mathrm{H}\beta} = 0.61/(\log \frac{[\mathrm{N\,II}]}{\mathrm{H}\alpha} - 0.05) + 1.3 \tag{4.2}$$

$$\textbf{Fe10} \qquad \log \frac{[\mathrm{O\,III}]}{\mathrm{H}\beta} = 1.01 \times \log \frac{[\mathrm{N\,II}]}{\mathrm{H}\alpha} + 0.48 \tag{4.3}$$

- **Star-forming galaxies** lie below and to the left of the Ka03 classification line
- **Composite galaxies** lie between the Ke01 and Ka03 classification lines
- **Seyfert galaxies** lie above the Ke01 classification line
- **LINERs** lie above the Ke01 and on the right of the Fe10 classification lines

The diagnostic diagram of the preliminary sample of the 6dFGS permits to discern 297 AGNs and 94 composite galaxies (fig. 4.1). The Seyfert galaxies (green points) are in the upper part of the diagram while the blue points correspond to the composite galaxies. The star-forming galaxies and the LINERs are plotted as red points. The spectra of the objects lying in the upper part of the diagram with $\log([\mathrm{O\,III}]/\mathrm{H}\beta) \geq 1.2$, show faint emission lines and in some of them the fitting of H$\beta$ emission line was not good because hidden by the continuum noise therefore producing an high value of $\log([\mathrm{O\,III}]/\mathrm{H}\beta)$.

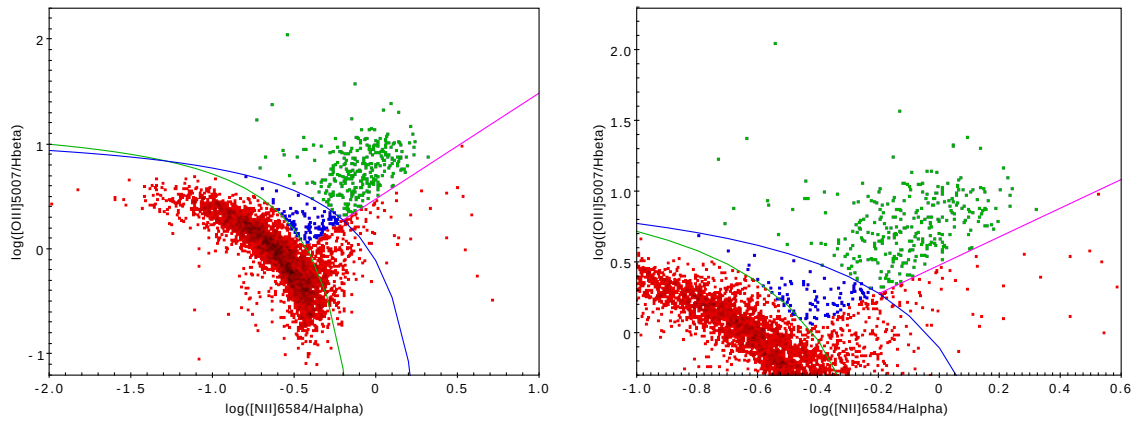


**Figure 4.1:** On left the diagnostic diagram of the 6dFGS preliminary sample, on the right a zoom of it. The green points represent the AGNs sources, the blue point the composite objects, the red point the star-forming galaxies and the LINERs. The blue line is the Ke01, the green line the Ka03, the violet line the Fe10.

In fig. 4.2 it is plotted the diagnostic diagram of the objects from the SDSS that allowed to separate, from the others galaxies, 614 AGNs and 83 composite galaxies. It is possible to observe that with respect to the plots of the other survey, it is not

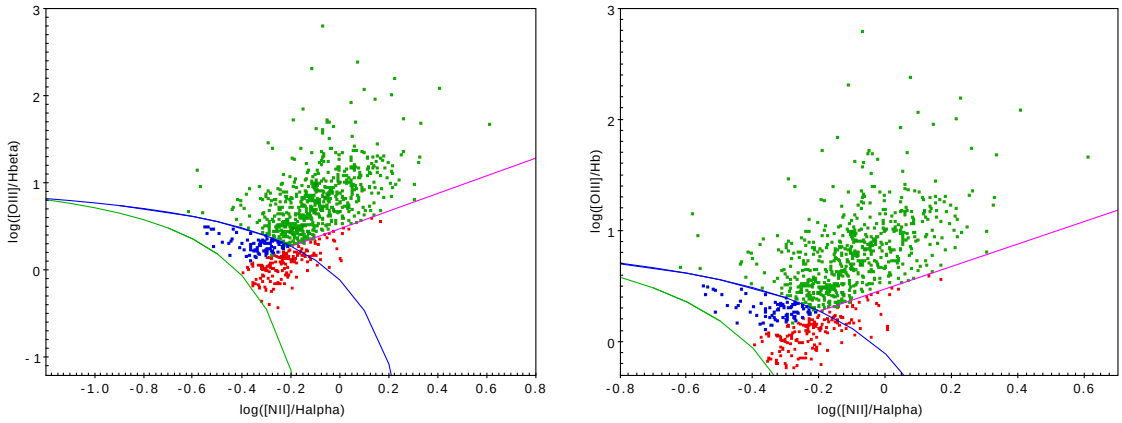


**Figure 4.2:** The same as in fig. 4.1 but for the SDSS sample.

present any star-forming galaxies, indeed the preliminary selected sample from SDSS was analysed using the $O_{123}$ *diagram* that allowed to separate them from AGNs. The legend used is the same of the others plots and it is observed that the objects in the upper part of the plot suffer of the same problem as in the 6dFGS sample.

### 4.1.1 Flux comparison

The SDSS database presents the measures of the emission lines fluxes obtained by Tremonti et al. 2004, so it is possible to compare them with the ones obtained by this work (fig. 4.3). The plots show a dashed line that corresponds to the one-to-one correlation (green dashed line) and a linear fit of the measures (red dashed line).

All the measures obtained in this work show flux values higher than those of the SDSS database as is possible to see from the linear fit (tab. 4.1). It is observed above that some spectra show faint H$\beta$ emission line hidden by the continuum noise that implicated some problems during the fitting procedure and the worst goodness of fit of the H$\beta$ plot with respect to the others reflect it. Finally to consider only the objects characterized by luminous emission lines, were selected the ones that showed a relative error on the measured fluxes of $err \leq 0.15$. This condition reduced the SDSS sample to 443 objects, 361 AGNs and 81 composite galaxies, and the 6dFGS sample to 318 sources, 235 AGNs and 83 composite galaxies.

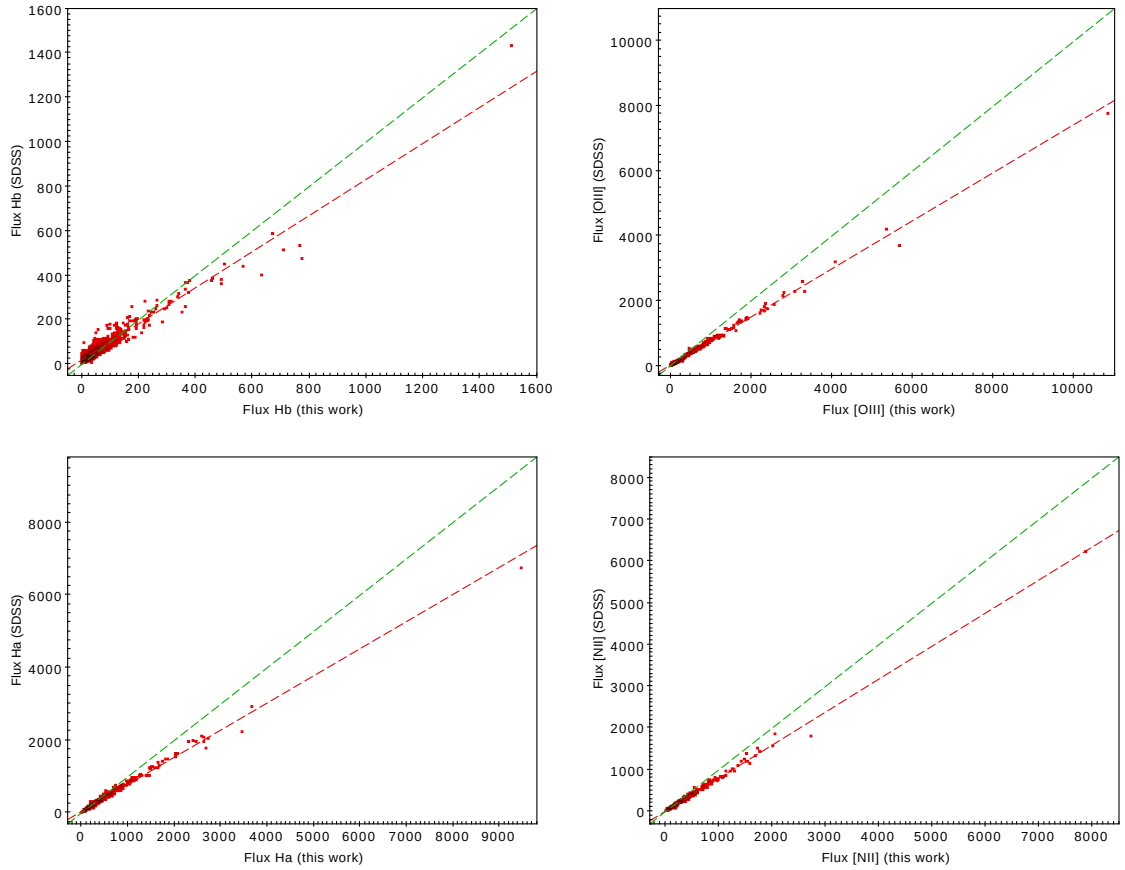


**Figure 4.3:** Comparison between the fluxes measured in this work and the fluxes from Tremonti et al. 2004. The units are $10^{-17}\,\mathrm{erg\,cm^{-2}\,s^{-1}}$. The green dashed line shows a one-to-one correlation, the red dashed line, the linear fit.

| Emission Line | linear fit | Correlation |
|---|---|---|
| H$\beta$ | $y = 0.81x + 20.25$ | 0.996 |
| [O III] | $y = 0.75x + 41.95$ | 0.995 |
| H$\alpha$ | $y = 0.74x + 22.40$ | 0.996 |
| [N II] | $y = 0.79x + 8.21$ | 0.996 |

**Table 4.1:** Linear fit of the fluxes comparison showed in fig. 4.3. The measures from SDSS database are represented by $y$ while the measures obtained in this work by $x$.

### 4.1.2 Spectra comparison

The composite galaxies and the Seyfert galaxies show different features on their spectra. The composite galaxies usually show a higher H$\alpha$ emission line with respect to the [O III], while in Seyfert galaxies the emissions from the [O III] are the most luminous. The spectra obtained by the two surveys permit to compare the two classes of objects.

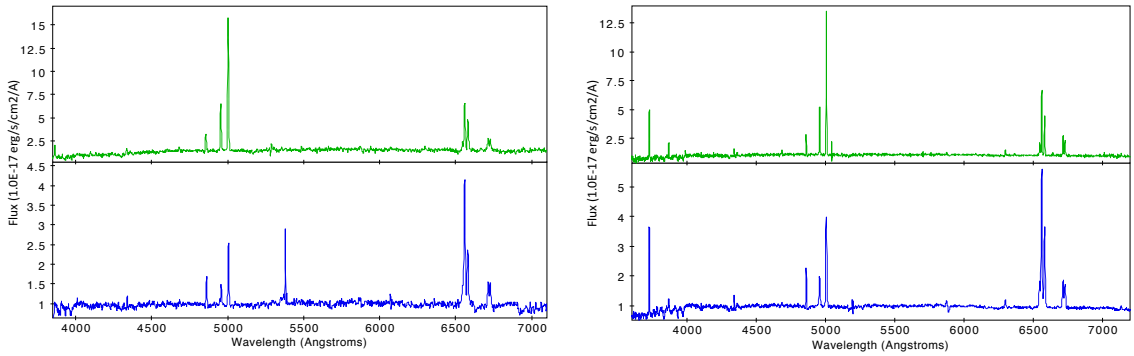


**Figure 4.4:** On the left two spectra from the 6dFGS, the upper is the Seyfert galaxy 2MASX J15155970-3825468 while the lower the composite galaxy CGCG 381-015. On the right the green line represents the Seyfert galaxy 2MASS J15415908-0143361 while the blue line shows the spectrum of the composite galaxy LCRS B121606.4-032746, both the spectra are from the SDSS.

Fig. 4.4 shows the SDSS spectra of the Seyfert galaxy 2MASS J15415908-0143361[1] that has a redshift $z = 0.105$ and of the composite galaxy LCRS B121606.4-032746[2] that has a redshift $z = 0.073$, and the 6dFGS spectra of the Seyfert galaxy 2MASX J15155970-3825468[3] at $z = 0.044$ and the composite galaxy CGCG 381-015[4] at $z = 0.036$.

The SDSS spectra are characterized by an higher resolution with respect to the 6dFGS, and this is confirmed also by the amount of emission lines that are possible to discern in their spectra. Moreover all the spectra show luminous emission lines that can be attributed to the presence of a large amount of gas ionized by the central source.

### 4.1.3 Sources comparison

The match of the sources from the two AGNs selected samples permits to find 7 objects observed by both the surveys. The most luminous of them is the source 2MASX J01464813-0837249[5] that shows a redshift of $z = 0.077$. Comparing the spectra from the two surveys (fig. 4.5), it is observed a not good overlapping of the emission lines:

[1] In our sample it corresponds to the SDSS spectrum spec-0926-52413-0153
[2] In our sample it corresponds to the SDSS spectrum spec-0333-52313-0124
[3] In our sample it corresponds to the 6dFGS spectrum g1515597-382547
[4] In our sample it corresponds to the 6dFGS spectrum g2337139-014101
[5] In our sample it corresponds to the SDSS spectrum spec-0664-52174-0559 and to the 6dFGS spectrum g0146482-083725

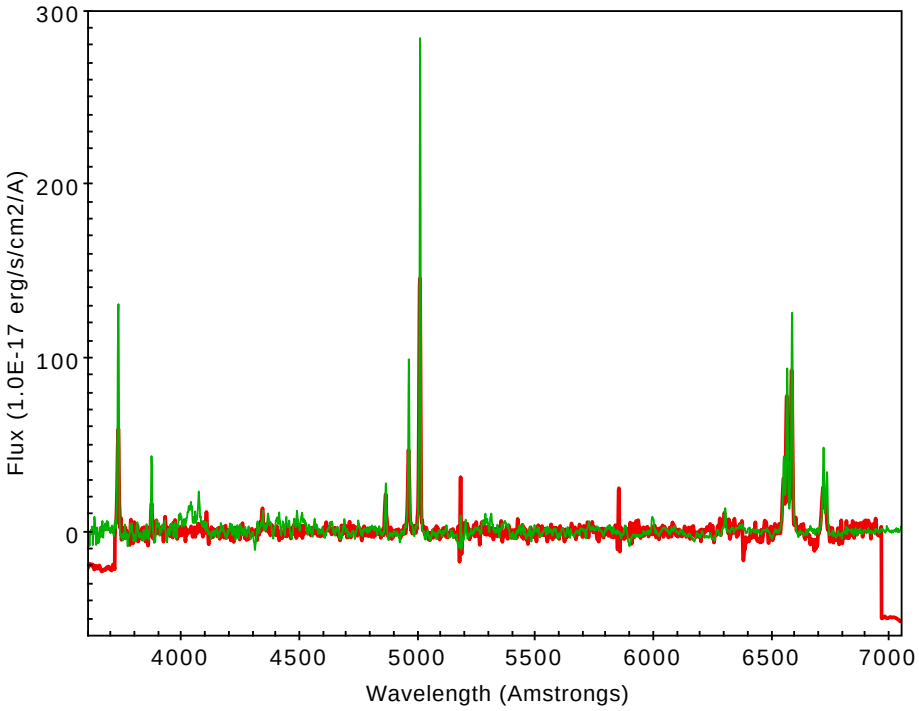


**Figure 4.5:** This plot shows the overlapping of the spectra spec-0664-52174-0559 from SDSS and g0146482-083725 from 6dFGS. The two spectra correspond to the same source 2MASX J01464813-0837249.

indeed the spectra from SDSS (green line) show flux values higher with respect to 6dFGS ones (red line) but the measured FWHMs are similar in both the spectra.

It is possible that the differences are caused by the flux calibration, indeed the spectra from 6dFGS were calibrated using a new method employing the calibrated spectra from SDSS. This procedure could add some errors on the fluxes measures. Another hypothesis, that could explain the differences on the flux ratios, is relative to the size of the optical fiber used during the observations. The size of the SDSS fiber is 3 arcsec while the 6dFGS one is 6.7 arcsec and this implicate that observing the same galaxy, the two fibers observe different regions on it (fig. 4.6). The output of fiber spectroscopy, with respect to long-slit or IFU observations, is a 1-D[6] spectrum for each object. The emitted light is averaged on the fiber size so the SDSS flux ratios show higher values because the observations are closer to the circumnuclear regions of the

[6]One-dimension spectrum, with respect to two-dimension spectrum obtained with long-slit observations or the data cube obtained with IFU, does not have any space information about the region from which the light is emitted.

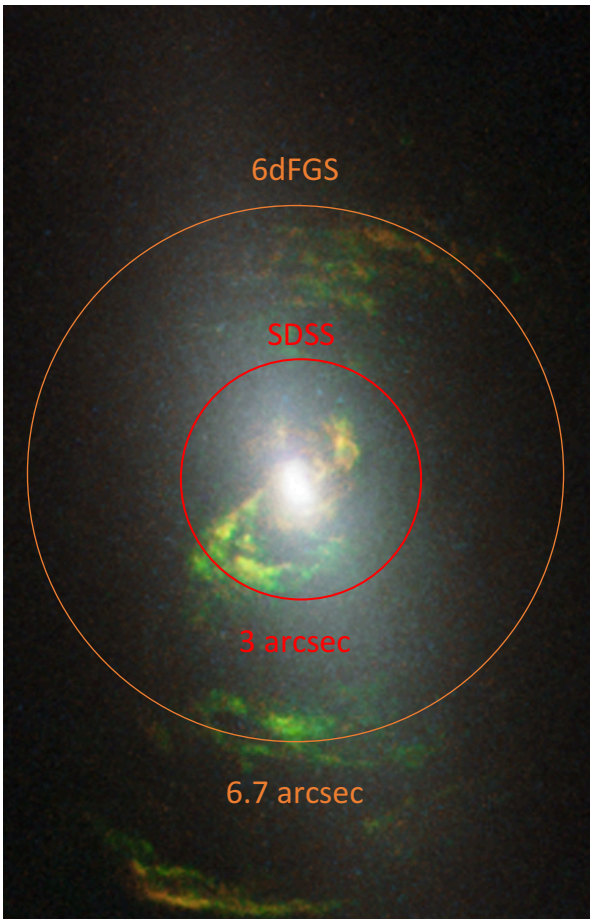


**Figure 4.6:** Comparison between the size of the fiber used by SDSS survey and by 6dFGS projected on the sky. On the background the image of the ionization cones of NGC 5252. This example image shows the size of the two fibers plotted over a galaxy, the images of the fibers are scaled each others.

AGNs while the 6dFGS observations, involving outer part of the AGNs that can be characterized by lower amount of gas, could product an average spectra characterized by lower flux ratio values.

## 4.2 FWHM spectral classification

The classification of the Seyfert galaxies is based on the visibility of the broad Balmer lines components but this criterion depends on the spectra quality and is a bit subjective (Donald E. Osterbrock and Ferland 2006). Additionally the visual classifying of a large number of spectra is extremely time-consuming so following Vaona et al. 2012, in this

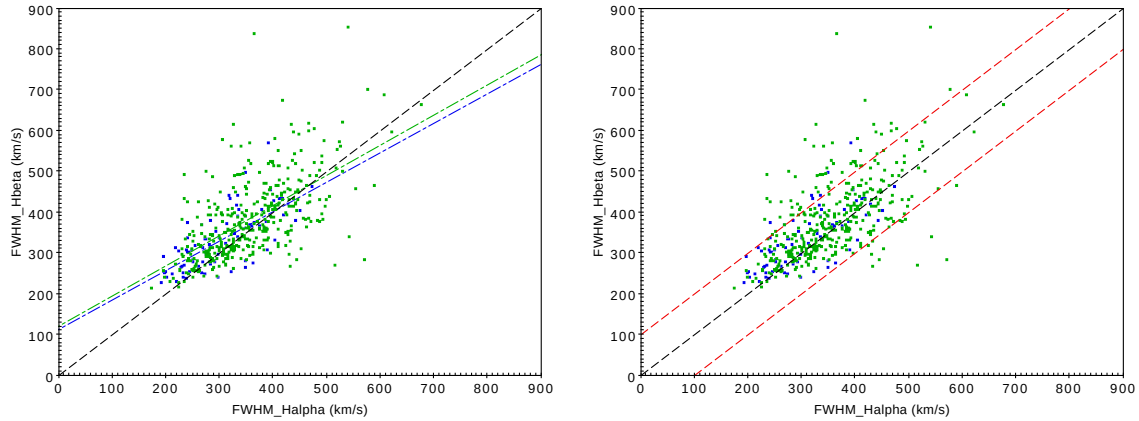


**Figure 4.7:** Comparison between FWHMs of H$\alpha$ and H$\beta$ of the SDSS sample. The green points show the AGNs while the blue points represent the composite galaxies. In the upper plot the green and blue dashed lines are the linear fit respectively of Seyfert galaxies and composite galaxies sample while the black dashed line show a one-to-one correlation, in the bottom plot the dashed red lines show a range within FWHM $\pm$ 100 km s$^{-1}$.

work it is adopted another criterion for the spectral classification of the sources based on the comparison between the FWHMs of the Balmer lines and on the presence of the H$\alpha$ and H$\beta$ broad component. The H$\alpha$ and H$\beta$ emission lines have to be emitted by the same gas components, so they are expected to have the same FWHM. In order to confirm that, the FWHM values obtained by the emission lines fitting process were compared. The SDSS sample is plotted in fig. 4.7 while the 6dFGS in fig. 4.8. According to the legend used above, the green points represent the Seyfert galaxies and the blue points the composite galaxies while the black dashed line shows a one-to-one correlation.

The plots are characterized by FWHM $\leq$ 1000 km s$^{-1}$ and the linear fits of the samples, represented in the first plot of the figures, are reported in tab. 4.2. On average the objects show a larger FWHMs on H$\alpha$ line with respect to H$\beta$ line and this could be due to the low resolution of the spectra. Indeed in some objects, it was not possible to resolve the broad component of the Balmer lines. The second plot in fig. 4.7 and fig. 4.8 shows two red dashed lines that correspond to the one-to-one correlation line shift of $\pm$100 km s$^{-1}$. The samples are divide, following this division, in

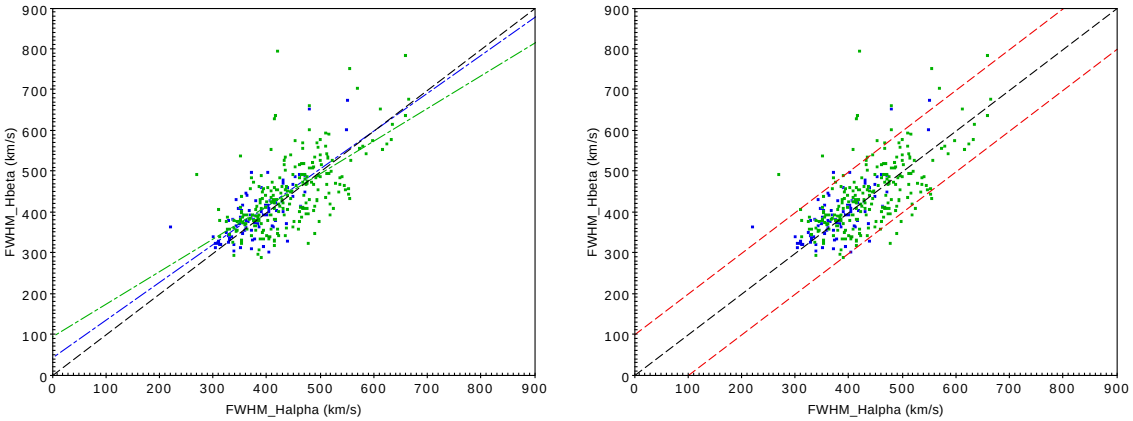


**Figure 4.8:** The same as in fig. 4.7 but for the 6dFGS sample.

three groups: the sources that lies above the FWHM $+100\,\mathrm{km\,s^{-1}}$ line, the ones that lie below FWHM $-100\,\mathrm{km\,s^{-1}}$ and the ones that lie between the two lines. The first group and the second one are characterized by sources that respectively show higher FWHM value of H$\beta$ of H$\alpha$ emission lines. These spectra were visually examined and it was observed that the large difference could be due to the relative low flux of respectively H$\alpha$ and H$\beta$ emission lines with respect to the continuum noise. This did not allow a well identification of them by the fitting code and therefore the measures of the fluxes and FWHMs could not be accurate. On the other side, the sources belonging to the third group show almost one-to-one correlation between the two FWHMs.

| Survey | Classification | linear fit | Correlation |
|---|---|---|---|
| SDSS | AGNs | $y = 0.74x + 121.17$ | 0.615 |
| | Composite | $y = 0.72x + 113.06$ | 0.696 |
| 6dFGS | AGNs | $y = 0.80x + 95.07$ | 0.616 |
| | Composite | $y = 0.93x + 43.35$ | 0.718 |

**Table 4.2:** Linear fit of the FWHM show in fig. 4.7 and in fig. 4.8. The FWHM of the H$\beta$ is represented in the relations by $y$, while the $x$ variable represents the FWHM of H$\alpha$.

### 4.2.1 Broad Balmer lines component

The Seyfert galaxies are divided in type-I and type-II in order to taking in account the effects of the inclination of the AGN with respect to the line of sight. Type-II Seyfert galaxies are characterized by narrow emission lines with typical FWHM $\leq 1000\,\mathrm{km\,s^{-1}}$, while type-I Balmer lines show a narrow emission overlap to a broader component characterized by FWHM $\geq 2000\,\mathrm{km\,s^{-1}}$. As seen in the chapter 1, the Seyfert galaxies can be divided in further classes taking into account the relative dominance of the H$\beta$ and H$\alpha$ broad component. To obtain the measures of the broad components, following a similar procedure of the first lines fitting, the spectra of the AGNs samples were re-fitted using a different code characterized by a model composed by four Gaussians: three for the narrow emission components and one for the broad Balmer one. Examples of the used model are showed in fig. 4.9, the plots on the upper part represent an example of the fitting model on two spectra from 6dFGS survey while the plots on the bottom show two examples from the SDSS sample. The analysis of spectra does not show any H$\beta$ broad component, and this is supposed due to the low resolution. On the other side, the fitting of the H$\alpha$ broad component was successful for 48 objects of the SDSS and for 32 objects of the 6dFGS survey. It is observed that if the broad component of H$\alpha$ is characterized by FWHM $\leq 2000\,\mathrm{km\,s^{-1}}$ it would be hidden by the H$\alpha$+[N II]$\lambda\lambda\,6548, 6584$ features as it is possible to see in fig. 4.9 in the plots on the left. In order to avoid that, only the spectra characterized by broad H$\alpha$ components with FWHM $\geq 2000\,\mathrm{km\,s^{-1}}$ and a relative error on the measured FWHMs broad component of $err \leq 0.25$ were considered in the broad-AGNs samples.

The mean FWHM values of the broad H$\alpha$ component obtained for sources selected from the SDSS is $\approx 4100\,\mathrm{km\,s^{-1}}$ while for the 6dFGS is $\approx 2900\,\mathrm{km\,s^{-1}}$. The plot in fig. 4.10 shows the comparison between the two samples. The visual examination of the sources characterized by FWHM $\geq$ FWHM$_{\mathrm{mean}}$ shows that these values could be due to the high noise present on the spectra that does not permit a precise fitting of the

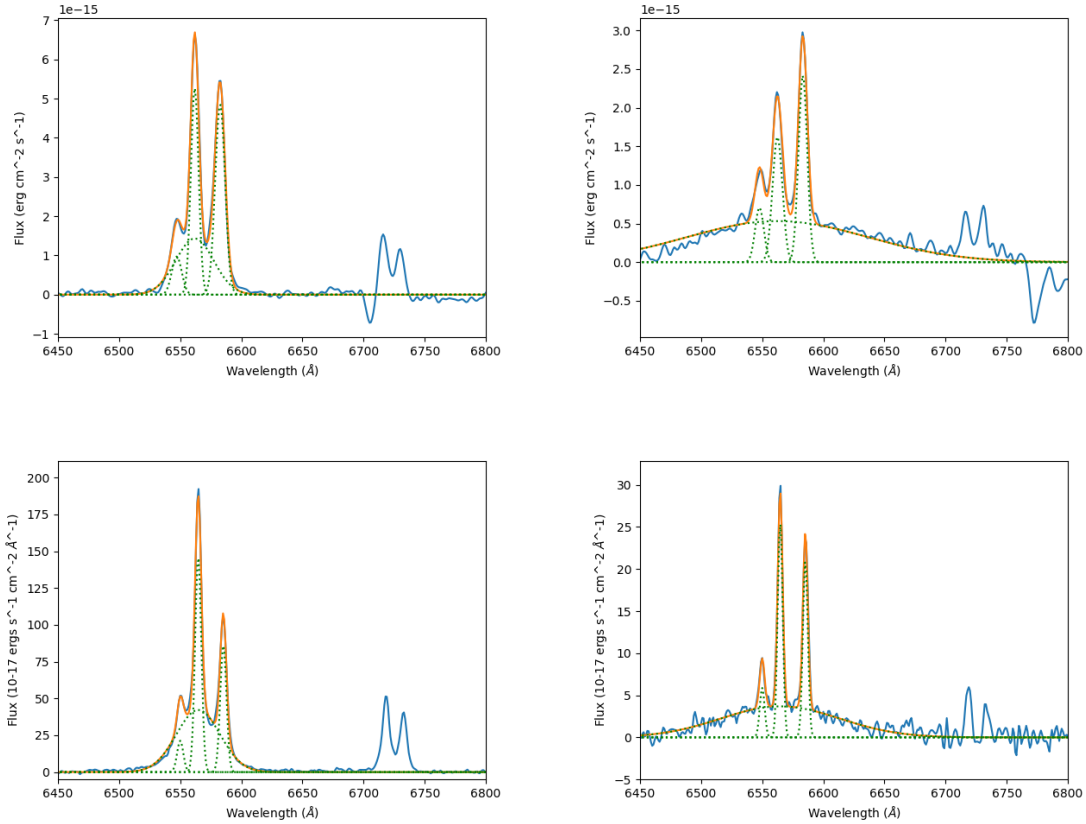


**Figure 4.9:** Examples of the H$\alpha$ broad component fitting process. The two upper plots represent two spectra from 6dFGS while the two spectra on the bottom are selected from the SDSS survey. The two plots on the left show a hidden broad component while on the right the broad component is evident.

various component. Following the classification proposed by D. E. Osterbrock 1977 these Seyfert galaxies can be classified as type-1.9.

## 4.3 The size-luminosity relation

The size-luminosity relation allows to estimate the size of the ENLR analyzing the luminosity of the [O III] emission line but it requires the distance of the sources.

The distance is calculated using a dedicated code written in python employing the *astropy.cosmology* package. Starting from the redshift $z$ of the sources, thanks to the cosmological model WMAP9 (Hinshaw et al. 2013) it is possible to obtain the luminosity distance of the objects. The next step is to calculate the luminosity of the

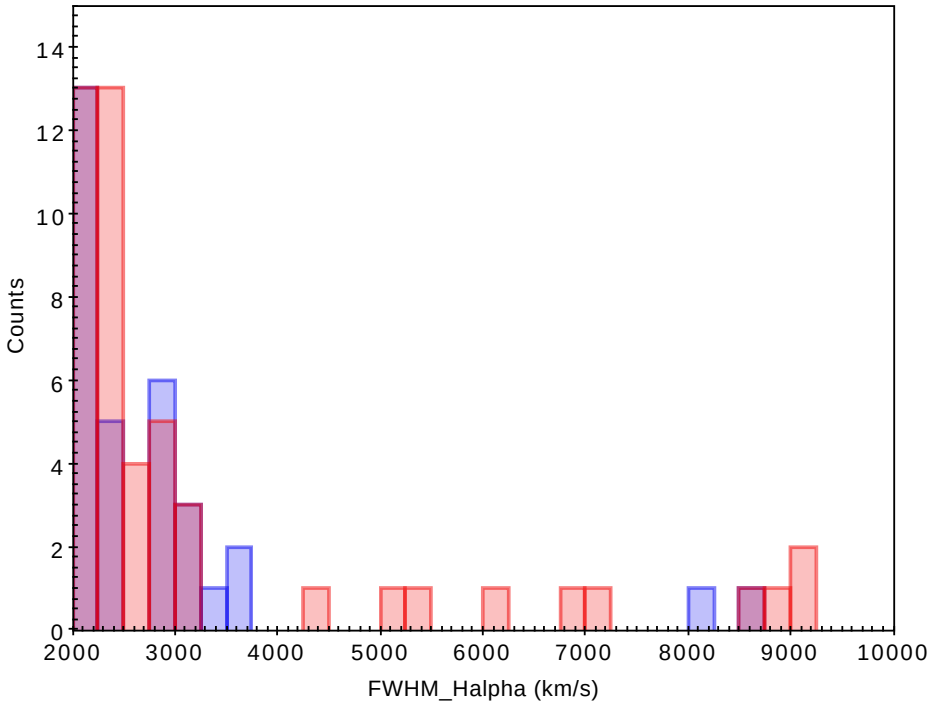


**Figure 4.10:** Comparison between the broad H$\alpha$ component FWHMs. The blue sample show the objects selected from 6dFGS and the red sample represents the objects from SDSS.

[O III] $\lambda$5007 emission line from the measured flux.

$$L_{[O\,III]} = 4\pi \times D^2 \times F_{[O\,III]} \tag{4.4}$$

In the eqn. (4.4), $L_{[O\,III]}$ is the luminosity of the emission line, $D$ the distance of the source and $F_{[O\,III]}$ the reddening corrected flux of [O III] $\lambda$5007. The spectra of this work are 1-D, so it is not possible to directly measure the size of the ENLR as it was done in others works (chapter 2). In order to obtain an estimation of the emission region's dimension it is supposed that it would correspond to the size of the fiber. The limit of this hypothesis is important, the calculated extension of the ENLR would be distance dependent, indeed the projection on the sky of the size of the fiber depends on the distance of the source (fig. 4.6). As example, objects with large ENLR but close to the observer, would show a smaller emission region with respect to distant objects with the same ENLR due to the projection of the fiber's size. However, following this

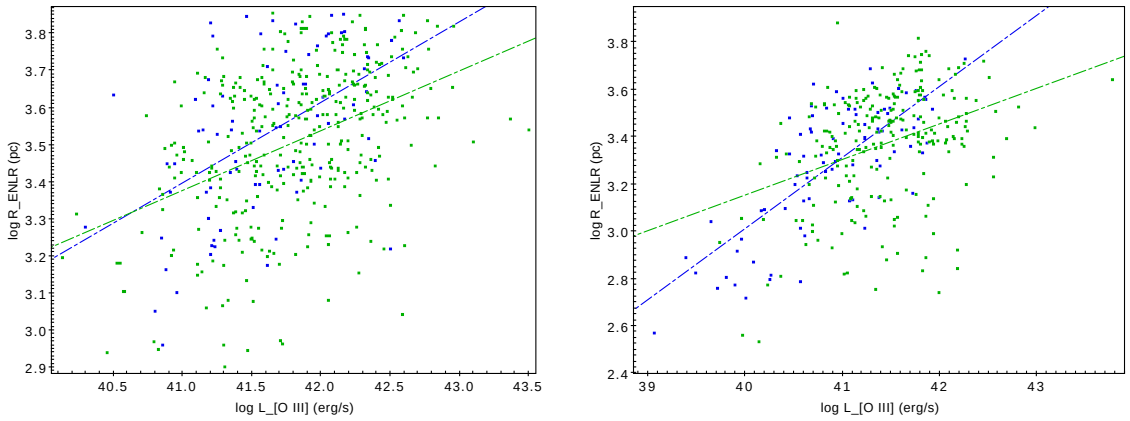


**Figure 4.11:** On the left the size-luminosity relation of the SDSS sample while on the right the same relation for the 6dFGS sample. The green dashed points represent the Seyfert galaxies, the blue points show the composite galaxies sample. The dashed lines are the linear fit of the samples and follow the same legend described above.

method, it is possible to obtain a rough estimate of the ENLRs size of a large number of sources. In order to obtain the extension of the ENLRs, it is employed the eqn. 4.5:

$$R_{ENLR} = \frac{\alpha \times D}{2} \tag{4.5}$$

$R_{ENLR}$ represent the radius of the ENLR, $\alpha$ the angular extension of the fibers[7] and $D$ the distance of the source. The measures obtained are plotted and the results are shown in fig. 4.11, following the legend used in the others plots, the green points represent the Seyfert galaxies while the blue points represent the composite galaxies.

The linear fits for each sample are reported in tab. 4.3, and taking into account the limits described above, they are almost in agreement with the ones obtained in others works (tab. 2.1). The differences on the size-luminosity relation can be attributed to the methods used to obtain the size of the ENLRs. Analysing the plots it is possible to observe that the objects characterized by higher $R_{ENLR}$ correspond to the ones with larger distance as it was supposed. Moreover the objects below the linear fit, that show lower values of $R_{ENLR}$ but large $L_{[O\,III]}$, correspond to the closest luminous

[7]The SDSS employed fibers with an angular size of 3 arcsec $= 1.45 \times 10^{-5}$ rad while 6dFGS used fibers an angular size of 6.7 arcsec $= 3.25 \times 10^{-5}$ rad

| Survey | Classification | linear fit | Correlation |
|---|---|---|---|
| SDSS | AGNs | $y = 0.16x - 3.22$ | 0.425 |
| | Composite | $y = 0.21x - 5.50$ | 0.715 |
| 6dFGS | AGNs | $y = 0.15x - 2.85$ | 0.362 |
| | Composite | $y = 0.30x - 8.99$ | 0.750 |

**Table 4.3:** Linear fit of the size-luminosity relations show in fig. 4.11. The $\log R_{ENLR}$ is represented in the relations by $y$ while the $x$ variable represents $\log L_{[OIII]}$.

objects. Analysing the size-luminosity plot, are identified 79 sources from SDSS and 11 from 6dFGS characterized by $R_{ENLR} > 5\,\mathrm{kpc}$. The $L_{[O\,III]}$ of SDSS sample shows a range of $40.13 \leq L_{[O\,III]} \leq 43.49\,\mathrm{erg\,s^{-1}}$ and a mean value of $L_{[O\,III]} \approx 41.78\,\mathrm{erg\,s^{-1}}$ and it is characterized by a mean distance $D \approx 498.3\,\mathrm{Mpc}$. The 6dFGS sample range of values the luminosity is quite different $39.06 \leq L_{[O\,III]} \leq 43.77\,\mathrm{erg\,s^{-1}}$ and a mean value of $L_{[O\,III]} \approx 41.30\,\mathrm{erg\,s^{-1}}$ and it shows a mean value of distance $D \approx 168.2\,\mathrm{Mpc}$. The $R_{ENLR}$ range of values obtained for the two samples reflect the distance bias, indeed for SDSS is $0.799 \leq R_{ENLR} \leq 7.144\,\mathrm{kpc}$ with a mean value of $R_{ENLR} \approx 3.610\,\mathrm{kpc}$ while for 6dFGS is $0.344 \leq R_{ENLR} \leq 7.570\,\mathrm{kpc}$ with a mean value of $R_{ENLR} \approx 2.570\,\mathrm{kpc}$. Comparing the samples, the 6dFGS one shows a lower mean distance of the objects with respect to SDSS. Indeed it is characterized by a lower number of objects that show $R_{ENLR} > 5\,\mathrm{kpc}$ and this could be due to the bias caused by the method used to estimate the size of the ENLR. As supposed above, these plots are biased by the distance of the sources, however they permit to discern a catalogue of objects characterized by high value of $R_{ENLR}$ and $L_{[O\,III]}$ that probably could show a large ENLR. To confirm this hypothesis, narrow-band or broad-band images surveys are now mandatory.

# Conclusion

The aim of the thesis is the selection of a new sample of type-II AGNs of the southern hemisphere. The sources were selected from SDSS and 6dFGS archives using two different methods: the [O I] $\lambda$6300/[O III] $\lambda$5007 vs [O II] $\lambda$3727/[O III] $\lambda$5007 diagram ($O_{123}$) by Vaona et al. 2012 for the spectra observed by SDSS and the classic diagnostic diagram [N II] $\lambda$6584/H$\alpha$ vs [O III] $\lambda$5007/H$\beta$ for the spectra of 6dFGS, that have a shorter spectral range and are not flux calibrated. Indeed one of the most challenging point of this work was the development of a strategy to obtain an average flux calibration function to apply to 6dFGS spectra. The stellar component was then modeled and subtracted to the spectra before fitting the emission lines. The higher spectral resolution and higher mean value of S/N of the SDSS spectra permitted an easier identification and a more successful fitting of the emission lines with respect to 6dFGS. Starting from samples of 36315 emission line spectra extracted from SDSS and 12737 from 6dFGS, applying the just exposed criteria, and making a continuous use of the visual inspection, which is very time consuming, a final catalog of 761 objects was obtained, that are divided in 597 Seyfert galaxies and 164 composite galaxies. To discern type-II from Intermediate-type Seyfert galaxies, the broad components of the Seyfert galaxies sample was fitted and this permitted to discern 80 possible type-1.9 Seyfert galaxies, that however were not excluded for the sample. Finally for each object of the catalog the size of the ENLR was estimated with the aim of discover new Seyfert galaxies characterized by large ionization cones. In particular, the sample contains 200 promising candidates with $L_{[O\,III]} \geq 10^{42}\,erg\,s^{-1}$. These AGN will be the first targets

of an already planned observational campaign through [O III] filters at Las Campanas Observatory (Chile). Once new ENLRs will be detected, their spectral properties will be investigated with following integral-field spectroscopic observations. These Seyfert galaxies will become also good targets for radio observations with the aim to check the ENLR-radio emission connection.

# Appendix A

# The sources's sample

Here are resumed the samples of the objects obtained after the selection procedure described in the chapter 4. The 6dFGS sample is composed by 38 objects characterized by $L_{[OIII]} > 10^{42}\,\mathrm{erg\,s^{-1}}$ while the SDSS sample contains 36 sources with $L_{[OIII]} > 10^{42.5}\,\mathrm{erg\,s^{-1}}$.

**Table A.1:** Sources details obtained from the 6dFGS database. *targetname* is the name of the objects, *ra* and *dec* are expressed in *deg* and show the coordinates on the sky, $A_V$ is the extinction in V-band while the others are parameters used on the query search process.

| targetname | ra | dec | $A_V$ | z | ngood | nmbest | quality |
|---|---|---|---|---|---|---|---|
| g0018046-544908 | 4.5192 | -54.8188 | 0.05 | 0.069 | 3 | 2 | |
| g0138054-125211 | 24.5225 | -12.8696 | 0.07 | 0.040 | 4 | 4 | |
| g0143405-511551 | 25.9187 | -51.2642 | 0.07 | 0.050 | 3 | 2 | |
| g0206040-160411 | 31.5168 | -16.0697 | 0.10 | 0.034 | 4 | 3 | |
| g0305294-361130 | 46.3723 | -36.1916 | 0.07 | 0.072 | 3 | 2 | |
| g0326538-570624 | 51.7240 | -57.1067 | 0.11 | 0.040 | 4 | 3 | |
| g0338336-163219 | 54.6398 | -16.5385 | 0.41 | 0.037 | 4 | 3 | |
| g0425031-252120 | 66.2630 | -25.3556 | 0.18 | 0.042 | 5 | 4 | |
| g0458521-120218 | 74.7173 | -12.0383 | 0.48 | 0.043 | 3 | 3 | |
| g0530281-333914 | 82.6170 | -33.6539 | 0.06 | 0.062 | 3 | 3 | |
| g0536580-004241 | 84.2418 | -0.7115 | 1.09 | 0.040 | 4 | 3 | |
| g0552332-112229 | 88.1384 | -11.3748 | 2.23 | 0.022 | 6 | 4 | |
| g0613286-375949 | 93.3690 | -37.9971 | 0.27 | 0.038 | 5 | 4 | |
| g0626025-370020 | 96.5105 | -37.0056 | 0.30 | 0.034 | 4 | 3 | |
| g0631384-140029 | 97.9100 | -14.0082 | 0.81 | 0.034 | 5 | 3 | |
| g1013199-355858 | 153.3329 | -35.9827 | 0.39 | 0.029 | 3 | 3 | |
| g1127234-291527 | 171.8476 | -29.2576 | 0.21 | 0.024 | 4 | 4 | |
| g1226024-233622 | 186.5102 | -23.6061 | 0.31 | 0.049 | 6 | 4 | |
| g1249411-811422 | 192.4211 | -81.2394 | 0.94 | 0.066 | 3 | 3 | |
| g1307059-234037 | 196.7747 | -23.6768 | 0.43 | 0.010 | 5 | 4 | |
| g1334252-302402 | 203.6049 | -30.4004 | 0.17 | 0.050 | 3 | 3 | |
| g1334396-232648 | 203.6652 | -23.4465 | 0.37 | 0.034 | 3 | 3 | |
| g1337500-235941 | 204.4581 | -23.9948 | 0.35 | 0.030 | 4 | 3 | |
| g1348152-421020 | 207.0634 | -42.1722 | 0.31 | 0.038 | 5 | 4 | |
| g1356080-340522 | 209.0332 | -34.0894 | 0.28 | 0.052 | 3 | 2 | |
| g1448440-435538 | 222.1832 | -43.9273 | 0.64 | 0.038 | 4 | 4 | |
| g1519173-445012 | 229.8221 | -44.8367 | 0.79 | 0.033 | 4 | 3 | |
| g1840276-532159 | 280.1151 | -53.3663 | 0.30 | 0.035 | 3 | 2 | |
| g2030369-253823 | 307.6537 | -25.6396 | 0.17 | 0.046 | 3 | 3 | |
| g2040157-512547 | 310.0656 | -51.4297 | 0.09 | 0.054 | 4 | 2 | |
| g2052023-570408 | 313.0097 | -57.0688 | 0.20 | 0.012 | 3 | 3 | |
| g2127028-225932 | 321.7618 | -22.9921 | 0.15 | 0.032 | 4 | 4 | |
| g2132279-300503 | 323.1162 | -30.0840 | 0.14 | 0.066 | 3 | 3 | |
| g2203235-073731 | 330.8481 | -7.6252 | 0.12 | 0.044 | 5 | 3 | |
| g2233571-254544 | 338.4880 | -25.7621 | 0.07 | 0.060 | 3 | 3 | |
| g2259193-303721 | 344.8303 | -30.6225 | 0.07 | 0.071 | 3 | 2 | |
| g2331578-184621 | 352.9906 | -18.7724 | 0.10 | 0.032 | 5 | 4 | |
| g2332071-232104 | 353.0297 | -23.3512 | 0.08 | 0.059 | 3 | 3 | |

**Table A.2:** Fluxes of the sources from 6dFGS sample. The unit of *fluxes* is $10^{-17}\,\mathrm{erg\,s^{-1}\,cm^{-2}}$, the FWHM unit is Å. The fitted emission lines are H$\beta$ $\lambda$4861 and H$\alpha$ $\lambda$6563 Balmer lines, [O III] $\lambda$5007 and [N II] $\lambda$6584.

| targetname | H$\beta$ | FWHM$_{\mathrm{H}\beta}$ | [O III] | FWHM$_{[\mathrm{O\,III}]}$ | H$\alpha$ | FWHM$_{\mathrm{H}\alpha}$ | [N II] | FWHM$_{[\mathrm{N\,II}]}$ |
|---|---|---|---|---|---|---|---|---|
| g0018046-544908 | 556.00 ± 21.22 | 11.40 ± 0.62 | 2363.00 ± 23.70 | 11.87 ± 0.16 | 2810.00 ± 118.20 | 12.41 ± 0.54 | 3546.00 ± 109.30 | 15.44 ± 0.64 |
| g0138054-125211 | 459.70 ± 27.57 | 8.66 ± 0.45 | 4415.00 ± 35.37 | 12.64 ± 0.16 | 2366.00 ± 17.82 | 9.47 ± 0.08 | 2283.00 ± 18.06 | 13.42 ± 0.15 |
| g0143405-511551 | 658.20 ± 12.17 | 7.89 ± 0.18 | 7536.00 ± 13.51 | 8.76 ± 0.02 | 2664.00 ± 29.03 | 11.80 ± 0.17 | 3066.00 ± 25.42 | 10.88 ± 0.12 |
| g0206040-160411 | 114.20 ± 6.68 | 5.44 ± 0.38 | 1266.00 ± 7.01 | 7.18 ± 0.05 | 1495.00 ± 8.67 | 8.80 ± 0.07 | 1072.00 ± 9.04 | 8.58 ± 0.08 |
| g0305294-361130 | 523.50 ± 19.30 | 6.73 ± 0.34 | 933.10 ± 19.16 | 6.90 ± 0.16 | 3433.00 ± 24.40 | 10.12 ± 0.09 | 1476.00 ± 24.27 | 10.51 ± 0.23 |
| g0326538-570624 | 397.20 ± 10.51 | 8.02 ± 0.24 | 4797.00 ± 13.34 | 9.92 ± 0.03 | 2158.00 ± 28.78 | 11.25 ± 0.18 | 2479.00 ± 31.52 | 12.45 ± 0.17 |
| g0338336-163219 | 292.50 ± 9.93 | 8.24 ± 0.39 | 2144.00 ± 10.67 | 8.79 ± 0.06 | 2326.00 ± 17.77 | 10.45 ± 0.10 | 1748.00 ± 18.22 | 10.35 ± 0.13 |
| g0425031-252120 | 328.30 ± 21.04 | 7.59 ± 0.65 | 2711.00 ± 32.56 | 9.80 ± 0.13 | 2099.00 ± 15.83 | 11.72 ± 0.12 | 2298.00 ± 14.51 | 11.12 ± 0.09 |
| g0458521-120218 | 141.30 ± 13.15 | 5.53 ± 0.46 | 828.80 ± 15.83 | 7.77 ± 0.17 | 1356.00 ± 39.21 | 8.84 ± 0.39 | 403.40 ± 28.19 | 8.06 ± 0.57 |
| g0530281-333914 | 828.60 ± 11.41 | 8.57 ± 0.16 | 7904.00 ± 13.17 | 9.27 ± 0.02 | 2882.00 ± 21.99 | 10.91 ± 0.11 | 2297.00 ± 23.09 | 12.93 ± 0.20 |
| g0536580-004241 | 603.50 ± 18.25 | 9.38 ± 0.30 | 5356.00 ± 17.73 | 10.62 ± 0.04 | 3396.00 ± 16.16 | 10.92 ± 0.07 | 2215.00 ± 13.42 | 10.82 ± 0.10 |
| g0552332-112229 | 1900.00 ± 48.88 | 6.66 ± 0.21 | 22520.00 ± 49.11 | 7.36 ± 0.02 | 10050.00 ± 64.46 | 9.04 ± 0.09 | 8071.00 ± 56.21 | 9.31 ± 0.10 |
| g0613286-375949 | 394.50 ± 12.03 | 5.54 ± 0.15 | 2425.00 ± 12.29 | 7.34 ± 0.04 | 2547.00 ± 16.74 | 8.12 ± 0.07 | 1776.00 ± 17.14 | 8.16 ± 0.10 |
| g0626025-370020 | 1412.00 ± 18.52 | 7.69 ± 0.12 | 15650.00 ± 21.59 | 8.19 ± 0.01 | 5492.00 ± 21.83 | 10.56 ± 0.05 | 5601.00 ± 16.86 | 10.30 ± 0.04 |
| g0631384-140029 | 144.90 ± 9.53 | 6.81 ± 0.49 | 965.00 ± 13.03 | 8.54 ± 0.11 | 1404.00 ± 12.35 | 11.33 ± 0.12 | 1337.00 ± 11.32 | 11.16 ± 0.12 |
| g1013199-355858 | 1893.00 ± 43.81 | 10.34 ± 0.27 | 21520.00 ± 38.81 | 10.82 ± 0.02 | 10500.00 ± 61.33 | 14.38 ± 0.09 | 8444.00 ± 54.60 | 15.17 ± 0.11 |
| g1127234-291527 | 801.80 ± 27.43 | 9.18 ± 0.38 | 7800.00 ± 31.22 | 8.91 ± 0.05 | 6820.00 ± 46.70 | 13.64 ± 0.10 | 7124.00 ± 41.82 | 14.48 ± 0.10 |
| g1226024-233622 | 232.20 ± 15.77 | 7.58 ± 0.57 | 2989.00 ± 25.02 | 12.76 ± 0.13 | 1482.00 ± 26.47 | 11.18 ± 0.24 | 1127.00 ± 25.73 | 14.46 ± 0.47 |
| g1249411-811422 | 247.10 ± 8.82 | 7.30 ± 0.27 | 3022.00 ± 10.50 | 9.53 ± 0.04 | 1068.00 ± 33.89 | 11.69 ± 0.47 | 815.70 ± 28.92 | 11.94 ± 0.47 |
| g1307059-234037 | 1440.00 ± 78.59 | 6.63 ± 0.44 | 14470.00 ± 84.37 | 8.76 ± 0.07 | 13510.00 ± 207.50 | 11.43 ± 0.20 | 14630.00 ± 188.00 | 11.76 ± 0.18 |
| g1334252-302402 | 431.50 ± 9.54 | 7.42 ± 0.16 | 3052.00 ± 11.94 | 9.84 ± 0.05 | 2525.00 ± 25.31 | 12.08 ± 0.14 | 1423.00 ± 18.15 | 12.29 ± 0.20 |
| g1334396-232648 | 1807.00 ± 28.31 | 9.39 ± 0.22 | 18300.00 ± 34.46 | 11.65 ± 0.03 | 7450.00 ± 60.93 | 13.80 ± 0.10 | 7607.00 ± 46.77 | 15.55 ± 0.12 |
| g1337500-235941 | 1328.00 ± 28.28 | 8.79 ± 0.21 | 12720.00 ± 33.98 | 9.80 ± 0.03 | 6045.00 ± 52.35 | 12.77 ± 0.12 | 5485.00 ± 46.19 | 13.19 ± 0.13 |
| g1348152-421020 | 2426.00 ± 25.22 | 9.74 ± 0.13 | 16250.00 ± 35.88 | 10.51 ± 0.03 | 9974.00 ± 27.81 | 10.49 ± 0.04 | 6350.00 ± 23.58 | 11.50 ± 0.06 |
| g1356080-340522 | 453.10 ± 16.67 | 9.58 ± 0.41 | 3218.00 ± 24.58 | 13.75 ± 0.14 | 2157.00 ± 18.21 | 11.26 ± 0.12 | 1554.00 ± 18.62 | 12.64 ± 0.20 |
| g1448440-435538 | 4939.00 ± 198.50 | 8.36 ± 0.46 | 44610.00 ± 199.70 | 9.43 ± 0.05 | 24780.00 ± 169.00 | 10.96 ± 0.10 | 24660.00 ± 149.90 | 11.97 ± 0.09 |
| g1519173-445012 | 134.60 ± 11.36 | 7.41 ± 0.75 | 812.50 ± 10.01 | 6.46 ± 0.10 | 1329.00 ± 16.52 | 8.06 ± 0.12 | 911.60 ± 15.88 | 8.15 ± 0.15 |
| g1840276-532159 | 314.70 ± 12.49 | 7.04 ± 0.35 | 3005.00 ± 14.71 | 8.37 ± 0.05 | 2110.00 ± 38.00 | 12.10 ± 0.24 | 2362.00 ± 32.45 | 13.33 ± 0.26 |
| g2030369-253823 | 276.60 ± 21.45 | 5.54 ± 0.44 | 1420.00 ± 28.04 | 9.06 ± 0.21 | 3153.00 ± 22.72 | 9.20 ± 0.09 | 2300.00 ± 28.14 | 9.58 ± 0.13 |
| g2040157-512547 | 1242.00 ± 16.08 | 7.49 ± 0.13 | 12640.00 ± 15.96 | 7.61 ± 0.01 | 4042.00 ± 17.75 | 9.53 ± 0.05 | 1682.00 ± 17.72 | 10.63 ± 0.14 |
| g2052023-570408 | 3552.00 ± 53.43 | 8.82 ± 0.15 | 32400.00 ± 47.67 | 9.16 ± 0.01 | 23250.00 ± 109.50 | 11.20 ± 0.06 | 15810.00 ± 100.30 | 12.01 ± 0.10 |
| g2127028-225932 | 502.10 ± 20.56 | 6.30 ± 0.27 | 2768.00 ± 23.44 | 7.61 ± 0.07 | 3858.00 ± 14.05 | 10.17 ± 0.04 | 2533.00 ± 14.83 | 10.31 ± 0.07 |
| g2132279-300503 | 608.10 ± 9.86 | 6.15 ± 0.12 | 5631.00 ± 10.10 | 7.45 ± 0.02 | 2322.00 ± 9.21 | 8.32 ± 0.04 | 858.50 ± 9.47 | 8.51 ± 0.12 |
| g2203235-073731 | 3356.00 ± 40.67 | 7.88 ± 0.11 | 34670.00 ± 41.37 | 8.34 ± 0.01 | 12400.00 ± 86.18 | 10.39 ± 0.09 | 7856.00 ± 98.86 | 11.88 ± 0.18 |
| g2233571-254544 | 256.40 ± 16.24 | 6.72 ± 0.42 | 2279.00 ± 17.62 | 8.28 ± 0.07 | 1716.00 ± 32.59 | 10.69 ± 0.24 | 2075.00 ± 28.01 | 11.88 ± 0.22 |
| g2259193-303721 | 197.80 ± 10.91 | 12.68 ± 1.12 | 2046.00 ± 11.12 | 15.96 ± 0.09 | 1187.00 ± 39.85 | 14.37 ± 0.39 | 2033.00 ± 41.09 | 21.81 ± 0.49 |
| g2331578-184621 | 905.80 ± 17.32 | 6.73 ± 0.14 | 5084.00 ± 20.06 | 8.70 ± 0.04 | 5902.00 ± 23.90 | 9.28 ± 0.06 | 4990.00 ± 23.18 | 9.59 ± 0.07 |
| g2332071-232104 | 233.90 ± 18.22 | 7.21 ± 0.54 | 3255.00 ± 17.25 | 8.67 ± 0.06 | 3498.00 ± 62.77 | 12.08 ± 0.24 | 3007.00 ± 52.61 | 13.55 ± 0.34 |

**Table A.3:** Data used for the selection procedure of the sample. The unit of $FWHM_{\mathrm{H}\alpha}$ and $FWHM_{\mathrm{H}\beta}$ is $\mathrm{km\,s^{-1}}$, the distance $D$ is expressed in Mpc, the unit of $\mathrm{L_{[O\,III]}}$ is $10^{41}\,\mathrm{erg\,s^{-1}}$ and $\mathrm{R_{NLR}}$ is expressed pc.

| targetname | $\mathrm{FWHM_{H\alpha}}$ km/s | $\mathrm{FWHM_{H\beta}}$ km/s | $log$[O III]/H$\beta$ | log [N II]/H$\alpha$ | $z$ | D | log $L_{[\mathrm{O\,III}]}$ | log $R_{NLR}$ |
|---|---|---|---|---|---|---|---|---|
| g0018046-544908 | 567.09 ± 24.50 | 703.56 ± 38.14 | 0.597 ± 0.039 | 0.099 ± 0.052 | 0.069 | 314.4 | 42.251 | 3.708 |
| g0138054-125211 | 432.93 ± 3.52 | 534.52 ± 28.02 | 0.950 ± 0.061 | -0.018 ± 0.011 | 0.040 | 179.3 | 42.060 | 3.464 |
| g0143405-511551 | 539.34 ± 7.54 | 487.12 ± 11.23 | 1.040 ± 0.019 | 0.060 ± 0.014 | 0.050 | 224.2 | 42.149 | 3.562 |
| g0206040-160411 | 402.35 ± 3.15 | 335.80 ± 23.33 | 0.961 ± 0.059 | -0.151 ± 0.010 | 0.034 | 150.8 | 42.680 | 3.389 |
| g0305294-361130 | 462.73 ± 4.02 | 415.10 ± 20.67 | 0.205 ± 0.042 | -0.370 ± 0.018 | 0.072 | 329.1 | 42.253 | 3.728 |
| g0326538-570624 | 514.06 ± 8.41 | 494.65 ± 14.75 | 1.047 ± 0.027 | 0.058 ± 0.018 | 0.040 | 177.6 | 42.164 | 3.460 |
| g0338336-163219 | 477.63 ± 4.57 | 508.41 ± 24.25 | 0.809 ± 0.034 | -0.128 ± 0.013 | 0.037 | 164.0 | 42.281 | 3.426 |
| g0425031-252120 | 535.64 ± 5.53 | 468.42 ± 39.99 | 0.873 ± 0.065 | 0.036 ± 0.010 | 0.042 | 187.0 | 42.190 | 3.483 |
| g0458521-120218 | 404.08 ± 17.69 | 341.35 ± 28.57 | 0.702 ± 0.095 | -0.531 ± 0.076 | 0.043 | 193.0 | 42.274 | 3.496 |
| g0530281-333914 | 498.57 ± 4.94 | 528.72 ± 9.75 | 0.969 ± 0.014 | -0.099 ± 0.013 | 0.062 | 282.7 | 42.158 | 3.662 |
| g0536580-004241 | 499.25 ± 3.06 | 578.71 ± 18.70 | 0.911 ± 0.030 | -0.188 ± 0.008 | 0.040 | 180.3 | 42.275 | 3.467 |
| g0552332-112229 | 413.18 ± 3.93 | 410.96 ± 13.02 | 1.040 ± 0.026 | -0.098 ± 0.009 | 0.022 | 96.6 | 42.269 | 3.196 |
| g0613286-375949 | 371.31 ± 3.06 | 341.84 ± 9.20 | 0.744 ± 0.031 | -0.160 ± 0.012 | 0.038 | 170.9 | 42.077 | 3.444 |
| g0626025-370020 | 482.84 ± 2.38 | 474.72 ± 7.71 | 1.028 ± 0.013 | 0.007 ± 0.005 | 0.034 | 150.4 | 42.063 | 3.388 |
| g0631384-140029 | 517.81 ± 5.62 | 420.53 ± 30.55 | 0.756 ± 0.067 | -0.026 ± 0.012 | 0.034 | 151.4 | 42.143 | 3.391 |
| g1013199-355858 | 657.50 ± 4.16 | 637.89 ± 16.60 | 1.019 ± 0.023 | -0.097 ± 0.009 | 0.029 | 127.0 | 42.554 | 3.315 |
| g1127234-291527 | 623.59 ± 4.34 | 566.55 ± 23.70 | 0.928 ± 0.034 | 0.015 ± 0.009 | 0.024 | 104.7 | 42.547 | 3.231 |
| g1226024-233622 | 511.05 ± 11.02 | 467.93 ± 35.05 | 1.065 ± 0.068 | -0.122 ± 0.029 | 0.049 | 218.8 | 42.366 | 3.551 |
| g1249411-811422 | 534.13 ± 21.62 | 450.52 ± 16.72 | 1.065 ± 0.036 | -0.119 ± 0.048 | 0.066 | 298.7 | 42.093 | 3.686 |
| g1307059-234037 | 522.61 ± 9.33 | 409.18 ± 26.91 | 0.937 ± 0.055 | 0.030 ± 0.020 | 0.010 | 43.0 | 42.180 | 2.844 |
| g1334252-302402 | 552.00 ± 6.26 | 457.75 ± 10.06 | 0.810 ± 0.022 | -0.252 ± 0.016 | 0.050 | 224.3 | 42.275 | 3.562 |
| g1334396-232648 | 630.90 ± 4.53 | 579.26 ± 13.45 | 0.985 ± 0.016 | 0.008 ± 0.010 | 0.034 | 152.3 | 42.224 | 3.393 |
| g1337500-235941 | 583.64 ± 5.71 | 542.36 ± 12.84 | 0.956 ± 0.021 | -0.044 ± 0.012 | 0.030 | 133.5 | 42.091 | 3.336 |
| g1348152-421020 | 479.37 ± 1.69 | 601.11 ± 8.27 | 0.806 ± 0.011 | -0.198 ± 0.005 | 0.038 | 169.6 | 42.262 | 3.440 |
| g1356080-340522 | 514.89 ± 5.35 | 591.24 ± 25.49 | 0.823 ± 0.038 | -0.144 ± 0.015 | 0.052 | 231.9 | 42.037 | 3.576 |
| g1448440-435538 | 500.94 ± 4.57 | 516.00 ± 28.33 | 0.925 ± 0.040 | -0.004 ± 0.009 | 0.038 | 167.6 | 42.970 | 3.435 |
| g1519173-445012 | 368.52 ± 5.39 | 457.31 ± 46.35 | 0.713 ± 0.085 | -0.169 ± 0.021 | 0.033 | 144.7 | 42.055 | 3.371 |
| g1840276-532159 | 553.28 ± 11.06 | 434.79 ± 21.91 | 0.933 ± 0.040 | 0.046 ± 0.023 | 0.035 | 153.9 | 42.132 | 3.398 |
| g2030369-253823 | 420.59 ± 3.98 | 342.03 ± 27.40 | 0.634 ± 0.080 | -0.143 ± 0.014 | 0.046 | 206.3 | 42.808 | 3.525 |
| g2040157-512547 | 435.40 ± 2.29 | 462.25 ± 8.15 | 1.001 ± 0.013 | -0.381 ± 0.011 | 0.054 | 240.9 | 42.129 | 3.593 |
| g2052023-570408 | 511.92 ± 2.61 | 544.09 ± 9.26 | 0.914 ± 0.015 | -0.171 ± 0.008 | 0.012 | 51.6 | 42.183 | 2.924 |
| g2127028-225932 | 465.06 ± 2.01 | 388.56 ± 16.79 | 0.687 ± 0.042 | -0.187 ± 0.007 | 0.032 | 143.3 | 42.226 | 3.367 |
| g2132279-300503 | 380.41 ± 1.83 | 379.49 ± 7.65 | 0.951 ± 0.016 | -0.433 ± 0.012 | 0.066 | 301.0 | 42.196 | 3.689 |
| g2203235-073731 | 474.75 ± 4.02 | 486.38 ± 7.04 | 1.000 ± 0.012 | -0.199 ± 0.014 | 0.044 | 197.9 | 42.575 | 3.507 |
| g2233571-254544 | 488.65 ± 10.79 | 414.48 ± 26.11 | 0.902 ± 0.064 | 0.079 ± 0.023 | 0.060 | 273.0 | 42.508 | 3.647 |
| g2259193-303721 | 656.77 ± 17.74 | 782.49 ± 69.18 | 0.974 ± 0.055 | 0.231 ± 0.039 | 0.071 | 322.9 | 42.453 | 3.720 |
| g2331578-184621 | 424.20 ± 2.56 | 415.10 ± 8.76 | 0.704 ± 0.020 | -0.076 ± 0.006 | 0.032 | 140.8 | 42.243 | 3.359 |
| g2332071-232104 | 552.19 ± 10.97 | 444.97 ± 33.45 | 1.052 ± 0.078 | -0.072 ± 0.025 | 0.059 | 267.3 | 43.775 | 3.638 |

**Table A.4:** Sources details obtained from the SDSS database. *spectra* is the name of the objects, *ra* and *dec* are expressed in *deg* and show the coordinates on the sky, $A_V$ is the extinction in V-band, [O II] is the flux of the emission line [O II] $\lambda$3727, [O III] is the flux of the emission line [O III] $\lambda$5007 and [O I] is the flux of the emission line [O III] $\lambda$6300. $0_{23}$ is the flux ratio between [O II] and [O III] while $0_{13}$ is the flux ratio between [O I] and [O III]. The unit of *fluxes* is $10^{-17}\,\mathrm{erg\,s^{-1}\,cm^{-2}}$.

| Spectra | ra | dec | $z$ | $A_V$ | [O II] | [O III] | [O I] | $\log 0_{23}$ | $\log O_{13}$ |
|---|---|---|---|---|---|---|---|---|---|
| spec-0267-51608-0047 | 148.4325 | -1.0264 | 0.110 | 0.13 | 181.16 | 712.00 | 94.52 | -0.298 | -0.877 |
| spec-0343-51692-0218 | 239.0220 | -0.6923 | 0.156 | 0.33 | 41.65 | 211.51 | 14.13 | -0.276 | -1.175 |
| spec-0344-51693-0102 | 241.3983 | -0.5664 | 0.124 | 0.45 | 47.18 | 196.03 | 32.46 | -0.314 | -0.781 |
| spec-0375-52140-0063 | 336.7797 | -0.3101 | 0.130 | 0.28 | 114.44 | 932.48 | 35.87 | -0.629 | -1.415 |
| spec-0377-52145-0474 | 338.6959 | -0.1126 | 0.143 | 0.17 | 94.57 | 592.90 | 33.91 | -0.519 | -1.243 |
| spec-0404-51812-0241 | 30.9399 | -1.0193 | 0.162 | 0.09 | 51.69 | 108.49 | 29.21 | 0.060 | -0.570 |
| spec-0412-52258-0272 | 46.8907 | -0.4425 | 0.185 | 0.20 | 79.10 | 342.52 | 21.94 | -0.565 | -1.193 |
| spec-0454-51908-0090 | 37.1620 | -9.4326 | 0.108 | 0.10 | 96.71 | 574.69 | 24.94 | -0.614 | -1.363 |
| spec-0454-51908-0545 | 37.2199 | -7.8932 | 0.185 | 0.08 | 23.00 | 306.83 | 11.43 | -0.556 | -1.429 |
| spec-0460-51924-0616 | 51.3557 | -6.1439 | 0.034 | 0.17 | 1111.96 | 7779.58 | 703.13 | -0.475 | -1.044 |
| spec-0462-51909-0129 | 55.3955 | -7.3237 | 0.066 | 0.18 | 143.18 | 367.31 | 33.38 | -0.189 | -1.042 |
| spec-0464-51908-0331 | 58.6264 | -5.4481 | 0.109 | 0.36 | 77.31 | 763.58 | 40.82 | -0.639 | -1.272 |
| spec-0467-51901-0058 | 131.9488 | -0.3810 | 0.051 | 0.09 | 179.07 | 467.50 | 160.24 | 0.063 | -0.465 |
| spec-0474-52000-0011 | 142.6019 | -0.7077 | 0.155 | 0.10 | 47.02 | 133.46 | 30.01 | -0.051 | -0.648 |
| spec-0476-52314-0215 | 143.7352 | -0.8444 | 0.083 | 0.09 | 63.17 | 354.61 | 30.02 | -0.329 | -1.072 |
| spec-0635-52145-0374 | 310.8513 | -5.6989 | 0.131 | 0.16 | 53.54 | 322.00 | 32.57 | -0.457 | -0.995 |
| spec-0636-52176-0505 | 314.3546 | -5.8200 | 0.178 | 0.14 | 160.14 | 267.37 | 31.92 | -0.030 | -0.923 |
| spec-0637-52174-0178 | 315.3326 | -7.0363 | 0.096 | 0.26 | 100.43 | 198.25 | 36.07 | -0.062 | -0.740 |
| spec-0640-52200-0398 | 321.0459 | -6.9949 | 0.118 | 0.51 | 45.94 | 75.26 | 16.94 | 0.134 | -0.648 |
| spec-0644-52173-0255 | 327.3491 | -8.6752 | 0.103 | 0.16 | 100.40 | 208.78 | 43.35 | -0.099 | -0.683 |
| spec-0652-52138-0073 | 4.7218 | -9.9907 | 0.145 | 0.12 | 39.88 | 102.70 | 14.92 | -0.130 | -0.838 |
| spec-0655-52162-0431 | 9.7191 | -9.4121 | 0.094 | 0.10 | 304.68 | 929.62 | 53.51 | -0.379 | -1.240 |
| spec-0659-52199-0607 | 18.3571 | -8.8927 | 0.191 | 0.16 | 21.15 | 106.42 | 13.56 | -0.214 | -0.895 |
| spec-0661-52163-0257 | 20.6427 | -10.7682 | 0.197 | 0.13 | 53.78 | 537.63 | 14.82 | -0.632 | -1.559 |
| spec-0664-52174-0006 | 27.8500 | -10.0686 | 0.171 | 0.09 | 61.14 | 131.00 | 14.92 | 0.002 | -0.943 |
| spec-0664-52174-0214 | 26.1188 | -10.1674 | 0.174 | 0.09 | 75.81 | 574.92 | 27.62 | -0.723 | -1.318 |
| spec-0664-52174-0374 | 26.0723 | -8.5114 | 0.052 | 0.08 | 254.50 | 937.52 | 76.97 | -0.202 | -1.086 |
| spec-0665-52168-0507 | 28.4347 | -8.9542 | 0.163 | 0.07 | 295.48 | 928.78 | 83.69 | -0.227 | -1.045 |
| spec-0668-52162-0094 | 34.9547 | -9.5611 | 0.156 | 0.09 | 27.34 | 294.58 | 23.43 | -0.460 | -1.099 |
| spec-0725-52258-0216 | 345.8430 | -10.5201 | 0.110 | 0.12 | 53.66 | 189.14 | 24.04 | -0.287 | -0.896 |
| spec-0921-52380-0340 | 222.9318 | -1.2844 | 0.181 | 0.14 | 31.45 | 275.98 | 18.22 | -0.481 | -1.180 |
| spec-0923-52404-0473 | 228.1965 | -1.7398 | 0.146 | 0.46 | 161.32 | 2148.46 | 49.38 | -0.771 | -1.639 |
| spec-0924-52409-0606 | 231.7318 | -0.9303 | 0.122 | 0.44 | 18.40 | 203.93 | 9.69 | -0.579 | -1.323 |
| spec-1023-52818-0230 | 312.9292 | -0.5912 | 0.191 | 0.33 | 194.83 | 340.45 | 45.23 | 0.037 | -0.877 |
| spec-1242-52901-0126 | 57.4187 | -1.0682 | 0.124 | 0.60 | 127.15 | 508.23 | 74.96 | -0.177 | -0.831 |
| spec-2878-54465-0423 | 21.5291 | -9.0993 | 0.110 | 0.11 | 86.98 | 228.93 | 35.86 | -0.058 | -0.805 |

**Table A.5:** Fluxes of the sources from SDSS sample. The unit of *fluxes* is $10^{-17}\,\mathrm{erg\,s^{-1}\,cm^{-2}}$, the FWHM unit is Å. The fitted emission lines are H$\beta$ $\lambda$4861 and H$\alpha$ $\lambda$6563 Balmer lines, [O III] $\lambda$5007 and [N II] $\lambda$6584.

| Spectra | H$\beta$ | FWHM$_{\mathrm{H}\beta}$ | O III | H$\alpha$ | FWHM$_{\mathrm{H}\alpha}$ | [N II] |
|---|---|---|---|---|---|---|
| spec-0267-51608-0047 | 167.33 ± 3.31 | 6.99 ± 0.05 | 839.77 ± 4.46 | 1101.29 ± 3.34 | 10.66 ± 0.04 | 835.66 ± 4.51 |
| spec-0343-51692-0218 | 42.03 ± 2.97 | 5.15 ± 0.07 | 240.94 ± 3.16 | 300.63 ± 4.12 | 8.95 ± 0.15 | 222.79 ± 4.60 |
| spec-0344-51693-0102 | 77.17 ± 8.77 | 8.00 ± 0.37 | 268.34 ± 10.52 | 626.87 ± 3.51 | 5.12 ± 0.03 | 416.22 ± 2.74 |
| spec-0375-52140-0063 | 73.74 ± 4.75 | 7.38 ± 0.05 | 1116.48 ± 6.08 | 454.32 ± 3.41 | 8.62 ± 0.07 | 477.44 ± 3.64 |
| spec-0377-52145-0474 | 38.51 ± 4.36 | 7.45 ± 0.08 | 700.91 ± 5.51 | 235.35 ± 3.48 | 8.66 ± 0.14 | 174.28 ± 4.10 |
| spec-0404-51812-0241 | 41.52 ± 3.40 | 8.50 ± 0.39 | 140.90 ± 4.44 | 362.04 ± 4.98 | 8.66 ± 0.12 | 283.49 ± 5.04 |
| spec-0412-52258-0272 | 59.99 ± 6.16 | 8.34 ± 0.18 | 414.57 ± 7.68 | 407.66 ± 2.86 | 8.79 ± 0.06 | 286.67 ± 2.89 |
| spec-0454-51908-0090 | 92.02 ± 4.33 | 5.70 ± 0.06 | 710.89 ± 5.36 | 619.87 ± 2.94 | 9.25 ± 0.05 | 546.53 ± 2.99 |
| spec-0454-51908-0545 | 41.88 ± 2.89 | 6.58 ± 0.08 | 356.41 ± 3.50 | 325.59 ± 3.41 | 6.93 ± 0.07 | 189.03 ± 2.67 |
| spec-0460-51924-0616 | 1509.63 ± 59.80 | 9.37 ± 0.09 | 10815.88 ± 69.40 | 9468.32 ± 17.96 | 6.67 ± 0.02 | 7872.53 ± 20.97 |
| spec-0462-51909-0129 | 64.65 ± 9.53 | 9.72 ± 0.27 | 478.72 ± 11.97 | 659.37 ± 4.27 | 10.19 ± 0.07 | 491.84 ± 3.85 |
| spec-0464-51908-0331 | 56.57 ± 3.76 | 5.77 ± 0.04 | 961.07 ± 5.29 | 617.88 ± 4.00 | 9.48 ± 0.07 | 602.16 ± 4.43 |
| spec-0467-51901-0058 | 233.97 ± 7.32 | 7.03 ± 0.11 | 585.39 ± 8.17 | 2646.98 ± 5.40 | 9.12 ± 0.02 | 1549.61 ± 4.48 |
| spec-0474-52000-0011 | 64.89 ± 3.42 | 7.01 ± 0.24 | 145.24 ± 4.58 | 580.96 ± 2.69 | 6.98 ± 0.03 | 363.91 ± 2.93 |
| spec-0476-52314-0215 | 57.14 ± 7.25 | 5.83 ± 0.14 | 461.04 ± 8.61 | 636.56 ± 3.07 | 6.91 ± 0.03 | 559.09 ± 2.93 |
| spec-0635-52145-0374 | 33.16 ± 4.72 | 6.36 ± 0.13 | 406.57 ± 5.96 | 311.57 ± 2.58 | 6.12 ± 0.04 | 309.73 ± 2.63 |
| spec-0636-52176-0505 | 99.78 ± 6.43 | 8.14 ± 0.22 | 278.56 ± 7.38 | 705.39 ± 2.50 | 10.63 ± 0.03 | 429.99 ± 2.28 |
| spec-0637-52174-0178 | 32.66 ± 3.22 | 6.87 ± 0.16 | 231.84 ± 4.03 | 498.95 ± 2.17 | 9.65 ± 0.04 | 356.75 ± 2.07 |
| spec-0640-52200-0398 | 25.19 ± 2.96 | 6.02 ± 0.27 | 90.47 ± 3.38 | 311.39 ± 3.04 | 7.96 ± 0.09 | 215.42 ± 3.77 |
| spec-0644-52173-0255 | 49.30 ± 4.81 | 9.97 ± 0.26 | 332.11 ± 6.34 | 855.42 ± 3.35 | 7.15 ± 0.03 | 805.09 ± 3.72 |
| spec-0652-52138-0073 | 33.70 ± 4.80 | 6.48 ± 0.41 | 113.20 ± 5.19 | 365.99 ± 2.60 | 9.28 ± 0.09 | 246.83 ± 3.18 |
| spec-0655-52162-0431 | 148.65 ± 4.08 | 6.12 ± 0.04 | 1308.29 ± 5.93 | 980.79 ± 2.19 | 10.28 ± 0.02 | 600.53 ± 1.79 |
| spec-0659-52199-0607 | 38.87 ± 2.38 | 6.72 ± 0.14 | 118.12 ± 2.41 | 362.94 ± 2.75 | 10.88 ± 0.06 | 189.20 ± 2.32 |
| spec-0661-52163-0257 | 51.76 ± 4.10 | 4.97 ± 0.05 | 580.97 ± 5.04 | 255.82 ± 2.08 | 6.02 ± 0.05 | 197.63 ± 1.94 |
| spec-0664-52174-0006 | 64.11 ± 4.98 | 5.74 ± 0.25 | 147.41 ± 6.89 | 501.73 ± 4.37 | 7.16 ± 0.06 | 241.33 ± 3.32 |
| spec-0664-52174-0214 | 74.05 ± 5.71 | 6.40 ± 0.13 | 665.61 ± 8.97 | 365.30 ± 2.90 | 7.56 ± 0.07 | 299.06 ± 3.10 |
| spec-0664-52174-0374 | 177.22 ± 15.01 | 9.25 ± 0.16 | 1324.35 ± 19.42 | 1649.00 ± 6.54 | 7.80 ± 0.04 | 908.20 ± 5.56 |
| spec-0665-52168-0507 | 244.94 ± 3.76 | 7.57 ± 0.03 | 1123.17 ± 4.43 | 1279.77 ± 3.38 | 12.87 ± 0.03 | 554.69 ± 2.81 |
| spec-0668-52162-0094 | 81.24 ± 4.66 | 8.34 ± 0.15 | 363.25 ± 4.87 | 556.57 ± 2.79 | 8.99 ± 0.04 | 404.87 ± 2.69 |
| spec-0725-52258-0216 | 34.89 ± 3.50 | 6.76 ± 0.15 | 221.77 ± 4.00 | 388.81 ± 2.58 | 8.70 ± 0.05 | 429.54 ± 2.68 |
| spec-0921-52380-0340 | 67.93 ± 5.77 | 7.22 ± 0.12 | 338.43 ± 5.37 | 416.30 ± 3.31 | 8.73 ± 0.06 | 276.01 ± 2.92 |
| spec-0923-52404-0473 | 314.61 ± 4.04 | 5.18 ± 0.01 | 2790.69 ± 4.98 | 1191.03 ± 3.74 | 7.71 ± 0.03 | 510.73 ± 3.49 |
| spec-0924-52409-0606 | 27.42 ± 3.55 | 5.15 ± 0.10 | 229.96 ±3.94 | 236.48 ± 3.12 | 8.33 ± 0.10 | 188.39 ± 2.95 |
| spec-1023-52818-0230 | 194.58 ± 1.78 | 7.38 ± 0.04 | 400.86 ±2.02 | 1078.74 ± 1.90 | 8.65 ± 0.02 | 332.69 ± 1.64 |
| spec-1242-52901-0126 | 129.91 ± 5.79 | 8.06 ± 0.14 | 676.62 ±7.41 | 876.07 ± 4.02 | 8.18 ± 0.04 | 697.27 ± 4.02 |
| spec-2878-54465-0423 | 44.81 ± 4.06 | 6.71 ± 0.25 | 214.12 ±5.03 | 533.89 ± 3.13 | 9.58 ± 0.05 | 552.46 ± 2.98 |

**Table A.6:** Data used for the selection procedure of the SDSS sample. The unit of $FWHM_{\mathrm{H}\alpha}$ and $FWHM_{\mathrm{H}\beta}$ is $\mathrm{km\,s^{-1}}$, the distance $D$ is expressed in Mpc, the unit of $\mathrm{L_{[O\,III]}}$ is $10^{41}\,\mathrm{erg\,s^{-1}}$ and $\mathrm{R_{NLR}}$ is expressed pc.

| Spectra | $\mathrm{FWHM_{H\alpha}}$ (km/s) | $\mathrm{FWHM_{H\beta}}$ km/s) | log [O III]/H$\beta$ | log [N II]/H$\alpha$ | $z$ | D | log $L_{[\mathrm{O\,III}]}$ | log $R_{NLR}$ |
|---|---|---|---|---|---|---|---|---|
| spec-0267-51608-0047 | 487.28 ± 1.65 | 431.39 ± 2.84 | 0.655 ± 0.020 | -0.123 ± 0.006 | 0.110 | 516.69 | 42.605 | 3.574 |
| spec-0343-51692-0218 | 409.11 ± 6.72 | 317.59 ± 4.13 | 0.708 ± 0.072 | -0.134 ± 0.025 | 0.156 | 753.21 | 42.507 | 3.737 |
| spec-0344-51693-0102 | 234.27 ± 1.37 | 493.85 ± 22.96 | 0.484 ± 0.120 | -0.182 ± 0.009 | 0.124 | 586.36 | 42.515 | 3.629 |
| spec-0375-52140-0063 | 393.80 ± 3.25 | 455.28 ± 3.15 | 1.138 ± 0.065 | 0.018 ± 0.011 | 0.130 | 618.07 | 42.791 | 3.651 |
| spec-0377-52145-0474 | 395.99 ± 6.31 | 459.60 ± 4.69 | 1.218 ± 0.113 | -0.133 ± 0.028 | 0.143 | 683.65 | 42.665 | 3.695 |
| spec-0404-51812-0241 | 395.67 ± 5.39 | 524.40 ± 24.19 | 0.469 ± 0.088 | -0.111 ± 0.022 | 0.162 | 786.54 | 42.590 | 3.756 |
| spec-0412-52258-0272 | 401.75 ± 2.83 | 514.71 ± 11.11 | 0.792 ± 0.104 | -0.156 ± 0.012 | 0.185 | 911.23 | 42.836 | 3.820 |
| spec-0454-51908-0090 | 423.01 ± 2.10 | 351.53 ± 3.76 | 0.841 ± 0.048 | -0.058 ± 0.007 | 0.108 | 506.92 | 42.548 | 3.565 |
| spec-0454-51908-0545 | 316.64 ± 3.25 | 406.27 ± 5.18 | 0.875 ± 0.070 | -0.240 ± 0.018 | 0.185 | 911.58 | 42.960 | 3.820 |
| spec-0460-51924-0616 | 304.85 ± 0.87 | 577.97 ± 5.25 | 0.812 ± 0.040 | -0.083 ± 0.003 | 0.034 | 152.81 | 42.589 | 3.044 |
| spec-0462-51909-0129 | 465.66 ± 3.25 | 600.00 ± 16.72 | 0.800 ± 0.149 | -0.132 ± 0.010 | 0.066 | 299.63 | 42.503 | 3.337 |
| spec-0464-51908-0331 | 433.48 ± 2.97 | 356.35 ± 2.72 | 1.156 ± 0.067 | -0.017 ± 0.010 | 0.109 | 511.25 | 43.366 | 3.569 |
| spec-0467-51901-0058 | 416.75 ± 0.78 | 434.05 ± 7.04 | 0.323 ± 0.034 | -0.238 ± 0.004 | 0.051 | 228.51 | 42.501 | 3.219 |
| spec-0474-52000-0011 | 319.24 ± 1.55 | 432.87 ± 14.63 | 0.287 ± 0.061 | -0.208 ± 0.009 | 0.155 | 745.39 | 42.593 | 3.733 |
| spec-0476-52314-0215 | 315.86 ± 1.51 | 360.11 ± 8.39 | 0.832 ± 0.128 | -0.062 ± 0.007 | 0.083 | 382.26 | 42.822 | 3.443 |
| spec-0635-52145-0374 | 279.66 ± 2.06 | 392.64 ± 8.27 | 1.023 ± 0.143 | -0.007 ± 0.012 | 0.131 | 621.22 | 42.950 | 3.654 |
| spec-0636-52176-0505 | 486.04 ± 1.42 | 502.49 ± 13.39 | 0.396 ± 0.070 | -0.219 ± 0.006 | 0.178 | 872.43 | 42.681 | 3.801 |
| spec-0637-52174-0178 | 441.34 ± 1.83 | 423.99 ± 9.81 | 0.759 ± 0.100 | -0.152 ± 0.007 | 0.096 | 444.60 | 43.099 | 3.508 |
| spec-0640-52200-0398 | 364.04 ± 4.30 | 371.41 ± 16.66 | 0.475 ± 0.123 | -0.166 ± 0.020 | 0.118 | 554.93 | 42.585 | 3.605 |
| spec-0644-52173-0255 | 326.88 ± 1.55 | 615.55 ± 16.23 | 0.729 ± 0.099 | -0.034 ± 0.006 | 0.103 | 477.99 | 43.497 | 3.540 |
| spec-0652-52138-0073 | 424.38 ± 4.07 | 399.79 ± 25.06 | 0.453 ± 0.150 | -0.176 ± 0.015 | 0.145 | 696.97 | 42.699 | 3.704 |
| spec-0655-52162-0431 | 469.95 ± 0.82 | 377.95 ± 2.41 | 0.899 ± 0.028 | -0.216 ± 0.004 | 0.094 | 435.02 | 42.651 | 3.499 |
| spec-0659-52199-0607 | 497.52 ± 2.74 | 414.48 ± 8.76 | 0.418 ± 0.065 | -0.288 ± 0.014 | 0.191 | 942.65 | 42.767 | 3.835 |
| spec-0661-52163-0257 | 275.09 ± 2.15 | 306.48 ± 3.33 | 1.020 ± 0.080 | -0.114 ± 0.013 | 0.197 | 974.64 | 42.593 | 3.849 |
| spec-0664-52174-0006 | 327.34 ± 2.74 | 354.06 ± 15.61 | 0.306 ± 0.091 | -0.322 ± 0.016 | 0.171 | 834.38 | 42.509 | 3.782 |
| spec-0664-52174-0214 | 345.71 ± 3.06 | 394.86 ± 7.90 | 0.924 ± 0.078 | -0.089 ± 0.013 | 0.174 | 848.29 | 42.529 | 3.789 |
| spec-0664-52174-0374 | 356.50 ± 1.60 | 570.93 ± 9.94 | 0.809 ± 0.086 | -0.264 ± 0.007 | 0.052 | 234.35 | 42.603 | 3.230 |
| spec-0665-52168-0507 | 588.39 ± 1.23 | 467.13 ± 2.04 | 0.628 ± 0.016 | -0.365 ± 0.006 | 0.163 | 788.90 | 42.774 | 3.757 |
| spec-0668-52162-0094 | 410.80 ± 1.87 | 514.71 ± 9.57 | 0.602 ± 0.059 | -0.142 ± 0.008 | 0.156 | 754.10 | 42.625 | 3.738 |
| spec-0725-52258-0216 | 397.46 ± 2.42 | 417.44 ± 9.01 | 0.728 ± 0.102 | 0.038 ± 0.009 | 0.110 | 515.24 | 42.764 | 3.572 |
| spec-0921-52380-0340 | 399.01 ± 2.74 | 445.53 ± 7.47 | 0.655 ± 0.086 | -0.182 ± 0.013 | 0.181 | 886.29 | 42.578 | 3.808 |
| spec-0923-52404-0473 | 352.34 ± 1.55 | 319.87 ± 0.86 | 0.933 ± 0.013 | -0.369 ± 0.008 | 0.146 | 700.50 | 42.613 | 3.706 |
| spec-0924-52409-0606 | 380.63 ± 4.39 | 318.02 ± 6.48 | 0.863 ± 0.131 | -0.103 ± 0.020 | 0.122 | 576.38 | 42.517 | 3.621 |
| spec-1023-52818-0230 | 395.26 ± 0.73 | 455.65 ± 2.47 | 0.277 ± 0.010 | -0.514 ± 0.005 | 0.191 | 942.94 | 42.565 | 3.835 |
| spec-1242-52901-0126 | 373.82 ± 1.78 | 497.61 ± 8.83 | 0.669 ± 0.046 | -0.103 ± 0.007 | 0.124 | 586.09 | 42.654 | 3.628 |
| spec-2878-54465-0423 | 437.73 ± 2.38 | 414.24 ± 15.68 | 0.601 ± 0.094 | 0.009 ± 0.008 | 0.110 | 516.01 | 42.845 | 3.573 |

# Bibliography


Antonucci, Robert (1993). "Unified models for active galactic nuclei and quasars." In: 31, pp. 473–521. DOI: 10.1146/annurev.aa.31.090193.002353.

Baldi, Ranieri D., Alessandro Capetti, and Gabriele Giovannini (2015). "Pilot study of the radio-emitting AGN population: the emerging new class of FR 0 radio-galaxies". In: 576, A38, A38. DOI: 10.1051/0004-6361/201425426. arXiv: 1502.00427 [astro-ph.GA].

Baldwin, Phillips, and R. Terlevich (1981). "Classification parameters for the emission-line spectra of extragalactic objects." In: 93, pp. 5–19. DOI: 10.1086/130766.

Beckmann, Shrader(auth.) (2012). *Active Galactic Nuclei*. Wiley-VCH.

Bennert, Nicola et al. (2002). "Size and Structure of the Narrow-Line Region of Quasars". In: 574.2, pp. L105–L109. DOI: 10.1086/342420. arXiv: astro-ph/0206334 [astro-ph].

Bennett, C. L. et al. (2014). "The 1% Concordance Hubble Constant". In: 794, 135, p. 135. DOI: 10.1088/0004-637X/794/2/135. arXiv: 1406.1718.

Böttcher, M. et al. (2013). "Leptonic and Hadronic Modeling of Fermi-detected Blazars". In: 768.1, 54, p. 54. DOI: 10.1088/0004-637X/768/1/54. arXiv: 1304.0605 [astro-ph.HE].

Cardelli, J. A., G. C. Clayton, and J. S. Mathis (1989). "The relationship between infrared, optical, and ultraviolet extinction". In: 345, pp. 245–256. DOI: 10.1086/167900.

Carilli, C. L. et al. (2019). "Imaging the AGN Torus in Cygnus". In: *arXiv e-prints*, arXiv:1904.01365, arXiv:1904.01365. arXiv: 1904.01365 [astro-ph.HE].

Chen, S. et al. (2018). "Probing narrow-line Seyfert 1 galaxies in the southern hemisphere". In: 615, A167, A167. DOI: 10.1051/0004-6361/201832678. arXiv: 1801.07234 [astro-ph.GA].

Cid Fernandes, Roberto et al. (2005). "Semi-empirical analysis of Sloan Digital Sky Survey galaxies - I. Spectral synthesis method". In: 358.2, pp. 363–378. DOI: 10.1111/j.1365-2966.2005.08752.x. arXiv: astro-ph/0412481 [astro-ph].

Cid Fernandes, R. et al. (2010). "Alternative diagnostic diagrams and the 'forgotten' population of weak line galaxies in the SDSS". In: 403.2, pp. 1036–1053. DOI: 10.1111/j.1365-2966.2009.16185.x. arXiv: 0912.1643 [astro-ph.CO].

Cracco, V. et al. (2011). "The origin of gas in extended narrow-line regions of nearby Seyfert galaxies - I. NGC 7212". In: 418.4, pp. 2630–2641. DOI: 10.1111/j.1365-2966.2011.19654.x. arXiv: 1109.1195 [astro-ph.CO].

Davies, Rebecca L. et al. (2016). "The Role of Radiation Pressure in the Narrow Line Regions of Seyfert Host Galaxies". In: 824.1, 50, p. 50. DOI: 10.3847/0004-637X/824/1/50. arXiv: 1604.06104 [astro-ph.GA].

Dopita, Michael A. et al. (2002). "Are the Narrow-Line Regions in Active Galaxies Dusty and Radiation Pressure Dominated?" In: 572.2, pp. 753–761. DOI: 10.1086/340429. arXiv: astro-ph/0203360 [astro-ph].

Fanaroff, B. L. and J. M. Riley (1974). "The morphology of extragalactic radio sources of high and low luminosity". In: 167, 31P–36P. DOI: 10.1093/mnras/167.1.31P.

Fischer, Travis C. et al. (2018). "Hubble Space Telescope Observations of Extended [O III]$\lambda$ 5007 Emission in Nearby QSO2s: New Constraints on AGN Host Galaxy Interaction". In: 856.2, 102, p. 102. DOI: 10.3847/1538-4357/aab03e. arXiv: 1802.06184 [astro-ph.GA].

Hainline, Kevin N. et al. (2013). "SALT Long-slit Spectroscopy of Luminous Obscured Quasars: An Upper Limit on the Size of the Narrow-line Region?" In: 774.2, 145, p. 145. DOI: 10.1088/0004-637X/774/2/145. arXiv: 1307.5852 [astro-ph.CO].

Heckman, Timothy M. and Philip N. Best (2014). "The Coevolution of Galaxies and Supermassive Black Holes: Insights from Surveys of the Contemporary Universe". In: 52, pp. 589–660. DOI: 10.1146/annurev-astro-081913-035722. arXiv: 1403.4620 [astro-ph.GA].

Hine, R. G. and M. S. Longair (1979). "Optical spectra of 3CR radio galaxies." In: 188, pp. 111–130. DOI: 10.1093/mnras/188.1.111.

Hinshaw, G. et al. (2013). "Nine-year Wilkinson Microwave Anisotropy Probe (WMAP) Observations: Cosmological Parameter Results". In: 208.2, 19, p. 19. DOI: 10.1088/0067-0049/208/2/19. arXiv: 1212.5226 [astro-ph.CO].

Jones, D. Heath, Mike A. Read, et al. (2009). "The 6dF Galaxy Survey: final redshift release (DR3) and southern large-scale structures". In: 399.2, pp. 683–698. DOI: 10.1111/j.1365-2966.2009.15338.x. arXiv: 0903.5451 [astro-ph.CO].

Jones, D. Heath, Will Saunders, et al. (2004). "The 6dF Galaxy Survey: samples, observational techniques and the first data release". In: 355.3, pp. 747–763. DOI: 10.1111/j.1365-2966.2004.08353.x. arXiv: astro-ph/0403501 [astro-ph].

Kang, Daeun and Jong-Hak Woo (2018). "Unraveling the Complex Structure of AGN-driven Outflows. III. The Outflow Size-Luminosity Relation". In: *The Astrophysical Journal* 864.2, 124, p. 124. DOI: 10.3847/1538-4357/aad561. arXiv: 1807.08356 [astro-ph.GA].

Kauffmann, Guinevere et al. (2003). "The host galaxies of active galactic nuclei". In: 346.4, pp. 1055–1077. DOI: 10.1111/j.1365-2966.2003.07154.x. arXiv: astro-ph/0304239 [astro-ph].

Kewley, Lisa J. et al. (2006). "The host galaxies and classification of active galactic nuclei". In: 372.3, pp. 961–976. DOI: 10.1111/j.1365-2966.2006.10859.x. arXiv: astro-ph/0605681 [astro-ph].

Kewley et al. (2001). "Theoretical Modeling of Starburst Galaxies". In: 556.1, pp. 121–140. DOI: 10.1086/321545. arXiv: astro-ph/0106324 [astro-ph].

Khachikian, E. Y. and D. W. Weedman (1974). "An atlas of Seyfert galaxies." In: 192, pp. 581–589. DOI: 10.1086/153093.

Liu, Guilin et al. (2013). "Observations of feedback from radio-quiet quasars - I. Extents and morphologies of ionized gas nebulae". In: 430.3, pp. 2327–2345. DOI: 10.1093/mnras/stt051. arXiv: 1301.1677 [astro-ph.CO].

Maraschi, L., G. Ghisellini, and A. Celotti (1992). "A Jet Model for the Gamma-Ray–emitting Blazar 3C 279". In: 397, p. L5. DOI: 10.1086/186531.

Matsuta, K. et al. (2012). "Infrared and Hard X-Ray Diagnostics of Active Galactic Nucleus Identification from the Swift/BAT and AKARI All-sky Surveys". In: 753.2, 104, p. 104. DOI: 10.1088/0004-637X/753/2/104. arXiv: 1205.0140 [astro-ph.HE].

Mortlock, Daniel J. et al. (2011). "A luminous quasar at a redshift of z = 7.085". In: 474.7353, pp. 616–619. DOI: 10.1038/nature10159. arXiv: 1106.6088 [astro-ph.CO].

Netzer, Hagai (2013). *The Physics and Evolution Active Galactic Nuclei*. Cambridge University Press.

— (2015). "Revisiting the Unified Model of Active Galactic Nuclei". In: 53, pp. 365–408. DOI: 10.1146/annurev-astro-082214-122302. arXiv: 1505.00811 [astro-ph.GA].

Osterbrock, D. E. (1977). "Spectrophotometry of Seyfert 1 galaxies." In: 215, pp. 733–745. DOI: 10.1086/155407.

Osterbrock, Donald E. and Gary J. Ferland (2006). *Astrophysics of gaseous nebulae and active galactic nuclei*.

Padovani, P. et al. (2017). "Active galactic nuclei: what's in a name?" In: 25.1, 2, p. 2. DOI: 10.1007/s00159-017-0102-9. arXiv: 1707.07134 [astro-ph.GA].

Schlegel, D. J., D. P. Finkbeiner, and M. Davis (1998). "Maps of Dust Infrared Emission for Use in Estimation of Reddening and Cosmic Microwave Background Radiation

Foregrounds". In: 500, pp. 525–553. DOI: 10.1086/305772. eprint: astro-ph/9710327.

Schmitt, H. R. et al. (2003). "A Hubble Space Telescope Survey of Extended [O III] $\lambda$5007 Å Emission in a Far-Infrared-Selected Sample of Seyfert Galaxies: Results". In: 597.2, pp. 768–779. DOI: 10.1086/381224. arXiv: astro-ph/0307255 [astro-ph].

Storchi-Bergmann, T. et al. (2018). "Bipolar Ionization Cones in the Extended Narrow-line Region of Nearby QSO2s". In: 868.1, 14, p. 14. DOI: 10.3847/1538-4357/aae7cd. arXiv: 1810.06246 [astro-ph.GA].

Sun, Ai-Lei et al. (2018). "Imaging extended emission-line regions of obscured AGN with the Subaru Hyper Suprime-Cam Survey". In: 480.2, pp. 2302–2323. DOI: 10.1093/mnras/sty1394. arXiv: 1803.07241 [astro-ph.GA].

Thomas, Adam D. et al. (2018). "Interrogating Seyferts with NebulaBayes: Spatially Probing the Narrow-line Region Radiation Fields and Chemical Abundances". In: *The Astrophysical Journal* 856.2, 89, p. 89. DOI: 10.3847/1538-4357/aab3db. arXiv: 1803.00740 [astro-ph.GA].

Tran, Hien D., Joseph S. Miller, and Laura E. Kay (1992). "Detection of Obscured Broad-Line Regions in Four Seyfert 2 Galaxies". In: 397, p. 452. DOI: 10.1086/171801.

Tremonti, Christy A. et al. (2004). "The Origin of the Mass-Metallicity Relation: Insights from 53,000 Star-forming Galaxies in the Sloan Digital Sky Survey". In: 613.2, pp. 898–913. DOI: 10.1086/423264. arXiv: astro-ph/0405537 [astro-ph].

Trump, Jonathan R. et al. (2011). "Accretion Rate and the Physical Nature of Unobscured Active Galaxies". In: 733.1, 60, p. 60. DOI: 10.1088/0004-637X/733/1/60. arXiv: 1103.0276 [astro-ph.CO].

Vaona, L. et al. (2012). "Spectral properties of the narrow-line region in Seyfert galaxies selected from the SDSS-DR7". In: 427.2, pp. 1266–1283. DOI: 10.1111/j.1365-2966.2012.22060.x. arXiv: 1210.5201 [astro-ph.CO].

Veilleux, Sylvain and Donald E. Osterbrock (1987). "Spectral Classification of Emission-Line Galaxies". In: 63, p. 295. DOI: 10.1086/191166.

Wright, E. L. (2006). "A Cosmology Calculator for the World Wide Web". In: 118, pp. 1711–1715. DOI: 10.1086/510102. eprint: astro-ph/0609593.

Wu, Yu-Zhong et al. (2011). "The Different Nature of Seyfert 2 Galaxies With and Without Hidden Broad-line Regions". In: 730.2, 121, p. 121. DOI: 10.1088/0004-637X/730/2/121. arXiv: 1101.4132 [astro-ph.HE].